THE GEOLOGICAL SOCIETY OF AMERICA®

Constraining the early stage of the post-orogenic extensional tectonics in central Italy: New evidence from a long sediment core from the tectonically active L'Aquila Basin

G. Mondati[1], B. Giaccio[2], A.L. Deino[3], P. Arcangeli[1], A. Bertini[4], H. Huang[4], M. Nocentini[5], M. Iorio[6], A. Angelino[6], F. Cifelli[1], M. Mattei[1], L. Sagnotti[7], E. Gliozzi[1], M. Marchegiano[8], M. Petrelli[9], M. Peral[10,*], P. Claeys[10], E. Regattieri[11], G. Zanchetta[12], M. Spadi[13,*], M. Tallini[13], A.M. Conte[2], S. Conticelli[1,2,4], M. Casalini[2,4], S. Racano[1], and D. Cosentino[1,†]

[1]*Dipartimento di Scienze, Università degli Studi Roma Tre, 00146 Roma, Italy*
[2]*Istituto di Geologia Ambientale e Geoingegneria, Consiglio Nazionale delle Ricerche (IGAG-CNR), 00010 Montelibretti, Italy*
[3]*Berkeley Geochronology Center, Berkeley, California 94709, USA*
[4]*Dipartimento di Scienze della Terra, Università degli Studi di Firenze, 50121 Firenze, Italy*
[5]*Dipartimento per il Servizio Geologico d'Italia, Istituto Superiore per la Protezione e la Ricerca Ambientale (ISPRA), 00144 Roma, Italy*
[6]*Istituto di Scienze Marine, Consiglio Nazionale delle Ricerche (ISMAR-CNR), 80133 Napoli, Italy*
[7]*Istituto Nazionale di Geofisica e Vulcanologia (INGV), 00143 Roma, Italy*
[8]*Department of Stratigraphy and Paleontology, University of Granada, 18071 Granada, Spain*
[9]*Dipartimento di Fisica e Geologia, Università degli Studi di Perugia, I-06123 Perugia, Italy*
[10]*Archaeology, Environmental Changes and Geo-Chemistry, Vrije Universiteit Brussel, 1050 Brussels, Belgium*
[11]*Istituto di Geoscienze e Georisorse, Consiglio Nazionale delle Ricerche (IGG-CNR), 56127 Pisa, Italy*
[12]*Dipartimento di Scienze della Terra, Università degli Studi di Pisa, 56126 Pisa, Italy*
[13]*Dipartimento di Ingegneria Civile, Edile-Architettura e Ambientale, Università degli Studi dell'Aquila, 67100 L'Aquila, Italy*

ABSTRACT

The central Apennines are among the most seismically active sectors of the central Mediterranean region, as testified by the recent sequence of Mw >6 earthquakes (L'Aquila Mw 6.3, 6 April 2009; Amatrice Mw 6.2, 24 August 2016), that struck the region. Although many recent studies have focused on the recent history of the active and seismogenic faults, due to the poor understanding on the age of the fault-bounded intermontane basins and on the early stage of their continental deposition, less is known about the faults' long-term behavior.

To try to fill this knowledge gap, we analyzed a long sediment core (230 m depth, Castelnuovo 1 borehole; CN-1) recovered from the infill of the Plio-Pleistocene tectonically active L'Aquila Basin (Paganica–San Demetrio–Castelnuovo [PSC] Sub-basin) by employing $^{40}Ar/^{39}Ar$ dating, magnetostratigraphy, multiproxy paleoclimatic data (palynological analyses, pollen temperature index and clumped isotopes), and astrocyclostratigraphy.

Combining the results from the CN-1 pollen record, $^{40}Ar/^{39}Ar$ dating of a tephra (1.77 ± 0.15 Ma), and magnetostratigraphy of the CN-1 sediment core, we can refer the longest normal polarity interval (N3) to the Olduvai subchron, which we use to constrain the CN-1 age model. Moreover, spectral analysis of the CN-1 calcimetry data series shows the presence of 13 obliquity-modulated cycles, resulting in an age of ca. 1490 ka for the top of the core and an age of ca. 2027 ka for its base. This time span encompasses Marine Isotopic Stages (MIS) 50–75. The occurrence of lacustrine ostracod fauna since the lowermost portion of the CN-1 core points to the presence in the PSC Sub-basin, already at 2 Ma, of a well-developed intermontane lake. Both pollen assemblages and clumped isotopes show warm-to-cold climate changes along the CN-1 sediment core, with clumped-isotope–derived temperatures of the lake waters of 15.4 ± 1.6 °C (MIS 53) and 11.5 ± 1.3 °C (MIS 52), whereas temperatures of 21 ± 1.7 °C and 15.6 ± 1.7 °C correspond respectively to MIS 67 and MIS 64.

The PSC Sub-basin shows a complex subsurface architecture, with highs and depocenters showing maximum thickness of the lacustrine deposits up to 510–450 m. Considering that the CN-1 age model points to a sedimentation rate of 0.3 mm/yr for the deep lacustrine deposits, the onset of the continental sedimentation in the L'Aquila intermontane basin started at ca. 3.2–3.0 Ma.

This post-orogenic extensional domain responsible for the onset and subsequent development of the L'Aquila intermontane basin is still active, representing an archive of ~3 m.y. of continued crustal extension from one of the most seismically active sectors of the central Mediterranean region.

1. INTRODUCTION

Reconstructing the spatio-temporal evolution of fault systems in tectonically and seismically active areas is crucial for understanding their long-term behavior and assessing related hazards (e.g., Nicol et al., 2005; Liu and Stein,

D. Cosentino https://orcid.org/0000-0002-7470-476X
[†]domenico.cosentino@uniroma3.it
[*]Present address: M. Peral—University of Bordeaux, Bordeaux, France; M. Spadi—Italferr, 00155 Roma, Italy

GSA Bulletin;
Published online 23 September 2025

https://doi.org/10.1130/B37760.1.

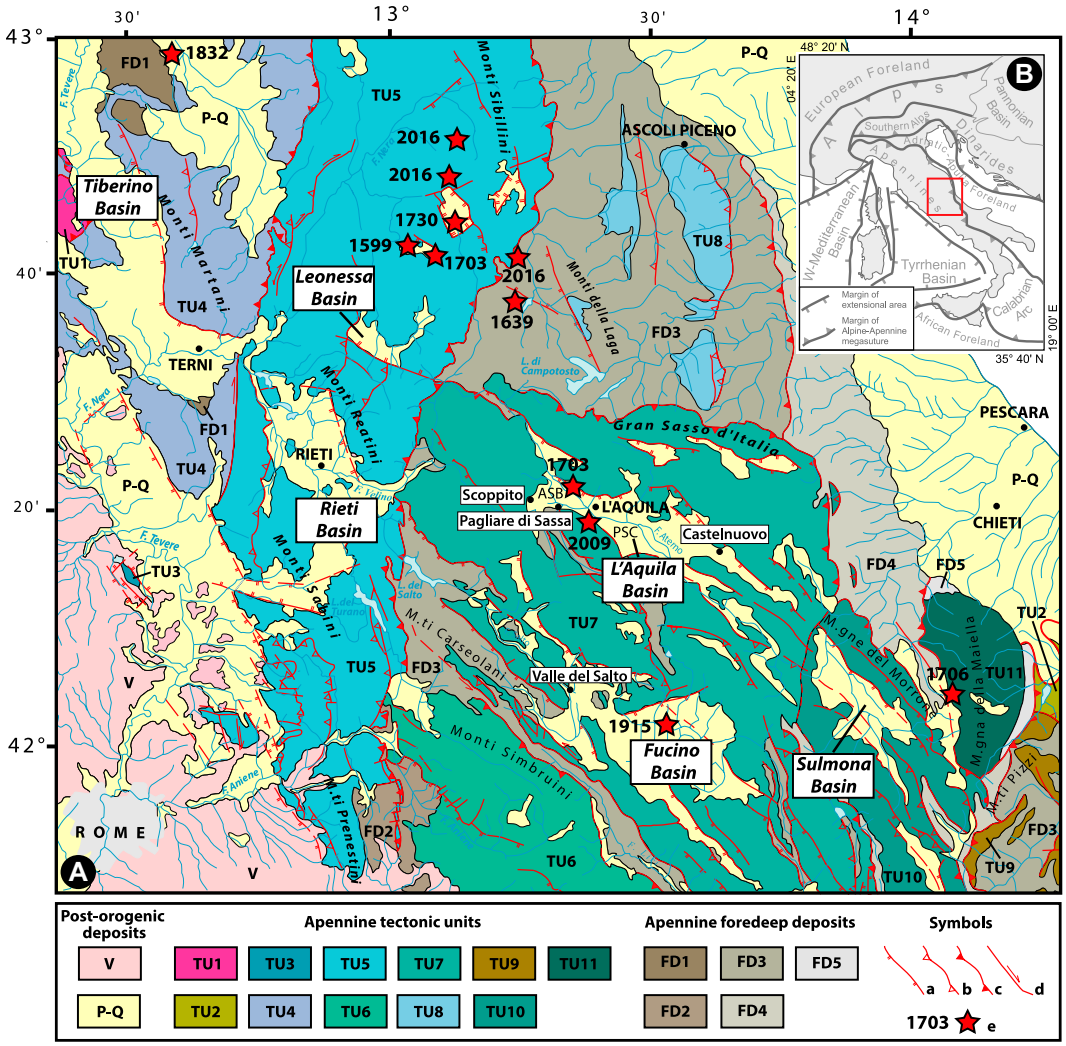

Figure 1. (A) Structural sketch of the central Apennines. V—Quaternary volcanics; P-Q—Plio-Quaternary marine and continental deposits; TU1—External Ligurian Unit; TU2—Sannio Unit; TU3—Mt. Soratte Tectonic Unit; TU4—Inner Umbria Tectonic Unit; TU5—Umbria-Marchean-Sabine Tectonic Unit; TU6—Simbruini-Ernici-Matese Tectonic Unit; TU7—Gran Sasso-Western Marsica Tectonic Unit; TU8—Molise Tectonic Unit; TU9—Acquasanta-Montagnone Tectonic Unit; TU10—Morrone-Eastern Marsica Tectonic Unit; TU11—Maiella Tectonic Unit; FD1—Burdigalian foredeep deposits; FD2—Tortonian foredeep deposits; FD3—Messinian foredeep deposits; FD4—upper Messinian–early lower Pliocene foredeep deposits; FD5—late lower Pliocene foredeep deposits; (a) normal fault; (b) minor thrust; (c) major thrust; (d) strike-slip fault; (e) location and year of earthquakes with Mw >6. (B) Map showing the position of the area figured in (A) in the tectonic framework of the Alpine-Apennine suture zone. Modified from Cosentino et al. (2017).

2016; Manighetti et al., 2021; Iezzi et al., 2023; Arriga et al., 2024). The central Apennines are among the most seismically active regions of the Italian Peninsula. They have been intensely investigated in terms of their seismic hazard, as testified by the multitude of studies following the recent L'Aquila (6 April 2009, Mw = 6.3), Amatrice (24 August 2016, Mw = 6.2), and Norcia (30 October 2016, Mw = 6.5) earthquakes (e.g., Falcucci et al., 2009; Galli et al., 2010; EMERGEO Working Group, 2010; Giaccio et al., 2012; Falcucci et al., 2016; Lavecchia et al., 2016; Scognamiglio et al., 2018; Brozzetti et al., 2019; Cinti et al., 2019; Galli et al., 2019; Improta et al., 2019; Puliti et al., 2020; Maraio et al., 2023).

While many of these studies focus on the very recent history of the active and seismogenic fault systems, the earliest stages and overall spatio-temporal evolution of the extensional tectonic regime, which is responsible for the current central Apennine seismicity, are still poorly known. The post-orogenic crustal extension in the central Apennines is responsible for the development of a series of extensional intermontane basins along the axis of the chain (e.g., Tiberino, Norcia, Leonessa, Rieti, L'Aquila, Fucino, and Sulmona basins; Fig. 1).

The long sedimentary successions hosted in these tectonic basins offer a unique opportunity to evaluate the timing of the activity and slip rates of the fault systems that bound the basins and controlled their evolution. The basin sediments are also valuable archives of the geological processes that occurred during the transition from a compressional domain, with the development of the central Apennine fold-and-thrust belt, to an extensional crustal domain responsible for the creation of today's basin-and-range topography (e.g., Cavinato and De Celles, 1999; Cosentino et al., 2017; Fellin et al., 2022; Racano et al., 2024).

The age of the transition from compressional to extensional deformation, which defines the early-stage development of the central Apennine extensional intermontane basins, is not well constrained due to a lack of exposure of the oldest basin deposits. The oldest well-dated extensional intermontane basin in the central Apennines is the Tiberino Basin (e.g., Barchi et al., 1991; Basilici, 1997), where magnetostratigraphy, pollen grains, and large mammal remains point to a late Piacenzian age for its basal infill (e.g., Abbazzi et al., 1997; Pontini et al., 2002; Martinetto et al., 2014).

Climate cyclicity, as recorded in pollen and other records, has been valuable to help constrain stratigraphic relationships in sedimentary basins (e.g., Fischer, 1986; Hilgen, 1987, 1991; Schwarzacher, 2000; Suc and Popescu, 2005; Dubois et al., 2012; Soria et al., 2012; Zhou et al., 2023). The late Neogene and Quaternary environments of the Mediterranean area were substantially influenced by global climate changes, resulting in regional responses within a dynamic interplay with tectonics. Consequently, the Piacenzian–Calabrian continen-

tal pollen sites of the central Apennines (e.g., Valle del Salto, Madonna della Strada [near Scoppito], Pagliare di Sassa; Fig. 1) lack a continuous and well-calibrated record despite significant evidence on both flora and vegetation (e.g., Magri et al., 2010; Palombo et al., 2010; Sadori et al., 2010). However, this interval is well-documented in other well-calibrated continental (e.g., Upper Valdarno; Bertini, 2013) and marine (e.g., Semaforo and Vrica, Crotone Basin; Suc et al., 2010) pollen sites in Italy. The clearly observable 41,000-year obliquity-forced glacial/interglacial cycles since 2.6 Ma display a prevalent (but not exclusive) alternation between forest vegetation and open vegetation (including steppes; Bertini, 2010; Magri et al., 2017; Bertini and Combourieu-Nebout, 2023; and references therein). Moreover, pollen records enable us to track the gradual reduction and/or disappearance of taxa (e.g., Taxodiaceae, *Cathaya*, *Tsuga*, *Cedrus*, *Carya*, and *Pterocarya*), becoming more pronounced from the Gelasian, influenced by glacial/interglacial cycles. The timing of plant disappearance events varies among sites, depending on climate gradients associated with latitude, altitude, and physiography. The subtropical humid forest expanded extensively until the Piacenzian, but progressively disappeared ca. 1.2 Ma. All previous events, indicating substantial changes in flora composition and vegetation structure, provide valuable insights for stratigraphic correlations.

Recently, detailed studies on the ostracod assemblages from the Tiberino and L'Aquila basins (e.g., Spadi et al., 2016, 2018, 2019) point to a synchronous (late Piacenzian, ca. 3 Ma) onset of sedimentation in almost all the intermontane basins of the central Apennines (e.g., Cosentino et al., 2017). The presence of a *Caspiocypris*-bearing ostracod assemblage in the lacustrine deposits of L'Aquila Basin (San Nicandro Formation; Spadi et al., 2016), which points to a correlation with the *Caspiocypris* species-flock identified in the late Piacenzian–Gelasian of the Tiberino Basin (Spadi et al., 2018), is until now the only temporal constraint for the oldest synthem of L'Aquila Basin. Unfortunately, the basal infill of the L'Aquila Basin, which is usually covered by younger deposits, lacks any other independent chronological constraints (e.g., radiometric dating, magnetostratigraphy, large mammal remains, paleoclimatic proxies) to corroborate this correlation.

A different chronological argument to constrain the onset of deposition in L'Aquila Basin was suggested by Giaccio et al. (2012). Based on the presence of some calc-alkaline tephra layers that potentially originated from the Cimini Volcano, they proposed an age between 1.35 Ma and 0.78 Ma for the top of the lacustrine succession (San Nicandro Formation). In addition, assuming a sedimentation rate of 0.2 mm/yr for the deep-lake sediments of the L'Aquila Basin, Giaccio et al. (2012) estimated a maximum age of ca. 1.8 Ma for the base of the San Nicandro Formation, which should represent the age for the onset of extensional tectonics in the central Apennines.

An additional element of discussion concerning the evolution of the L'Aquila Basin are the different views on the extent of the early Pleistocene intermontane lake (e.g., Agostini et al., 2012; Cosentino et al., 2017; Geurts et al., 2020) and the different age of formation of the L'Aquila-Scoppito Sub-basin (ASB) and Paganica–San Demetrio–Castelnuovo (PSC) Sub-basin (e.g., Cosentino et al., 2017; Tallini et al., 2019; Bruno et al., 2022; Fig. 2). Although in the past 10 years several subsurface investigations (e.g., seismic reflection profiles and boreholes) provided an unprecedented reconstruction of the complex geometry of the L'Aquila sedimentary basin, which is a result of varying heights and depocenters (e.g., Macrì et al., 2016; Civico et al., 2017; Cosentino et al., 2017; Tallini et al., 2019; Bruno et al., 2022), the lack of precise chronological constraints on the basal basin infill prevented reaching a general consensus on their age formation and, consequently, on the tectono-sedimentary basin evolution.

With the aim of resolving these contrasting results and reducing the existing uncertainties about the age of the basin, and thus, by extension, of the onset of the current extensional tectonic and seismic regime, we applied an integrated multiple-dating approach, including

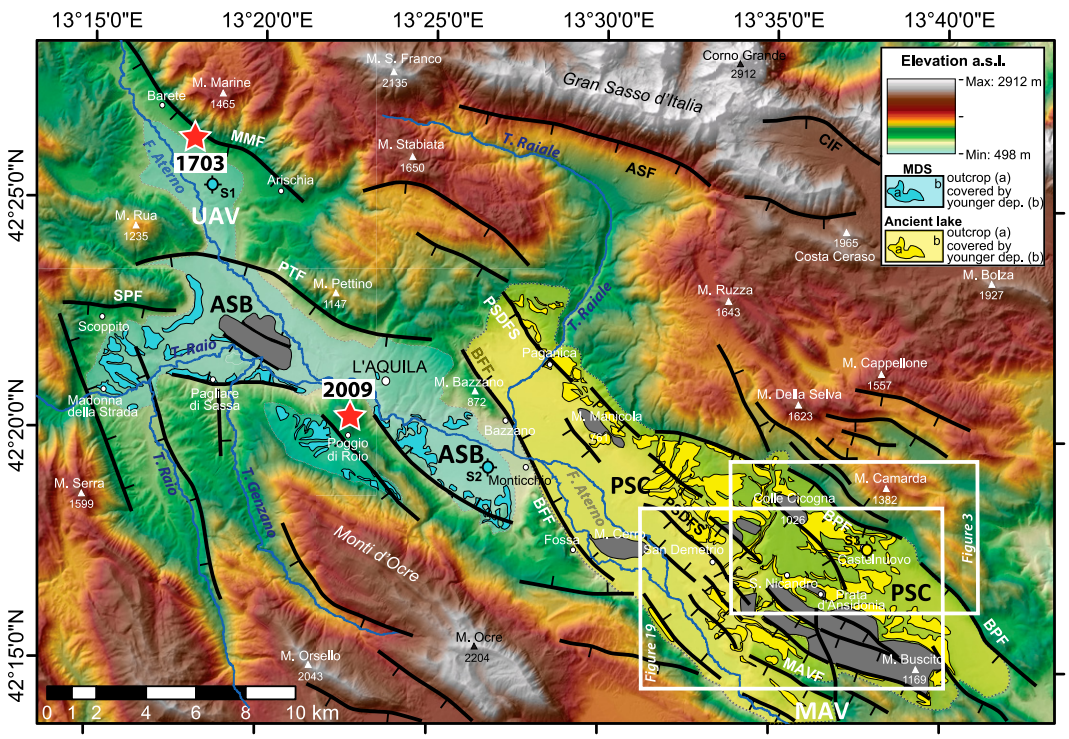

Figure 2. Map of the main active normal faults of the L'Aquila Basin. ASB—Aquila-Scoppito Sub-basin; ASF—Assergi fault; BFF—Bazzano-Fossa fault; BPF—Barisciano–San Pio fault; CIF—Campo Imperatore fault; MAV—Middle Aterno Valley; MAVF—Middle Aterno Valley fault system; MMF—Monte Marine fault; PSC—Paganica–San Demetrio–Castelnuovo Sub-basin; PSDFS—Paganica–San Demetrio fault system; PTF—Monte Pettino fault; SPF—Scoppito-Preturo fault; UAV—Upper Aterno Valley. Red stars indicate the epicenter of the 2 February 1703 Pizzoli earthquake (Mw 6.67) and of the 6 April 2009 L'Aquila earthquake (Mw 6.29). White boxes indicate the position of Figures 3 and 19. MDS—Madonna della Strada Formation. Modified from Cosentino et al. (2017).

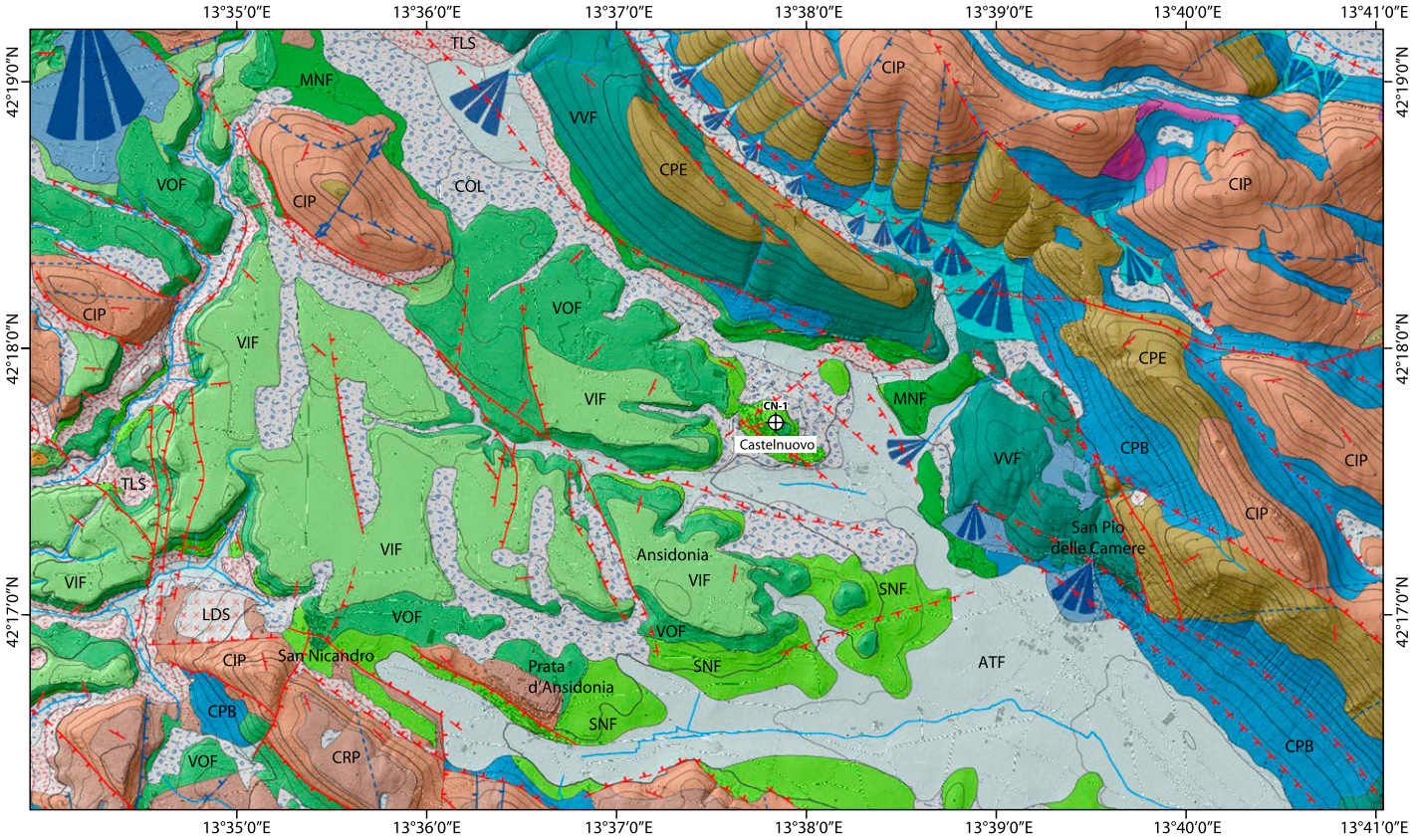

Figure 3. Geological map of the Castelnuovo area, with location of the CN-1 borehole. ATF—fluvial and alluvial deposits (Holocene); CIP—Mesozoic inner carbonate-platform succession; COL—colluvial deposits (Holocene); CPB—talus deposits (upper Pleistocene); CPE—Mesozoic carbonate-platform succession; CRP—Cenozoic carbonate-ramp/open-platform succession; LDS—landslide deposits (Holocene); MNF—Madonna della Neve Formation; SNF—San Nicandro Formation; TLS—talus deposits (Holocene); VIF—Valle dell'Inferno Formation; VOF—Valle Orsa Formation; VVF—Valle Valiano Formation. Modified from Nocentini et al. (2018).

$^{40}Ar/^{39}Ar$ dating, magnetostratigraphy, multiproxy paleoclimatic data, and astrocyclostratigraphy, to a long sediment core (Castelnuovo 1 borehole; CN-1) recovered from the L'Aquila Basin lacustrine succession.

Through defining the major depocentral depths of the PSC Sub-basin, the results of this multiple-dating approach on the CN-1 sediment core allowed us to better constrain (1) the starting age of the post-orogenic extensional tectonics in the axial zone of the central Apennines of Italy; (2) the formation of the tectonically controlled intermontane basins, which hosted thick continental successions; and (3) the end of the ancient (late Pliocene–early Pleistocene) San Nicandro Lake.

2. PREVIOUS STUDIES ON THE TECTONICALLY ACTIVE L'AQUILA BASIN

The L'Aquila Basin is a NW-SE–trending extensional intermontane basin, one of the widest in the central Apennines (Fig. 1). It is bordered to NE by an active normal fault system, on which the 6 April 2009 earthquake occurred (EMERGEO Working Group, 2010; Scognamiglio et al., 2010). This area is one of the most seismically active sectors of the central Mediterranean area (e.g., Amato et al., 1997; Bagh et al., 2007; Falcucci et al., 2011; Vannoli et al., 2012).

Like many other intermontane basins of the central Apennines, the tectonic evolution of the L'Aquila Basin is correlated with post-orogenic tectonic phases, mainly characterized by the onset of extension related to the opening of the Tyrrhenian back-arc basin in response to eastward slab roll-back, and the orogenic collapse of the Apennines (Dewey, 1988; Faccenna et al., 1996, 2001; Cipollari et al., 1999; Funiciello et al., 1999; Carminati and Doglioni, 2012; Cosentino et al., 2010, 2017; Fellin et al., 2022).

Due to the different paleodepositional environments of the continental Plio-Quaternary filling and the fault systems affecting the basin, L'Aquila Basin has been divided into two subbasins, which are characterized by different stratigraphic settings. The NW sector is represented by the L'Aquila-Scoppito Sub-basin (ASB), whereas the SE area is defined by the Paganica–San Demetrio–Castelnuovo (PSC) Sub-basin (Fig. 2).

The ASB is a W-E–trending half graben bordered to the north by the active Scoppito-Preturo and the Pettino normal faults (Fig. 2; Vezzani et al., 2009; Tallini et al., 2012; Storti et al., 2013; Arriga et al., 2024). The stratigraphy of the ASB has been studied principally by Bosi (1989), Centamore and Dramis (2010), Mancini et al. (2012), and Cosentino et al. (2017). According to Cosentino et al. (2017), the basal basin fill at the northern margin of ASB, which corresponds to the oldest continental deposits of the L'Aquila Basin (i.e., the Colle Cantaro–Cave synthem, upper Pliocene; Centamore and Dramis, 2010), shows wedge-shaped seismic facies, which indicates a syn-rift stage.

In the post-rift stage, many unconformity bounded stratigraphic units deposited within the ASB, mainly in an alluvial plain depositional environment, including the Madonna della Strada synthem (upper lower Pleistocene), the

Fosso di Genzano synthem (lower middle Pleistocene), the Colle Macchione-L'Aquila synthem (upper middle Pleistocene), the Fosso Vetoio synthem (lower upper Pleistocene), the Campo di Pile synthem (middle upper Pleistocene), and the Ponte Peschio synthem (upper upper Pleistocene; Cosentino et al., 2017; Nocentini et al., 2017).

The area examined in this study, where the CN-1 sediment core was recovered, is within the PSC Sub-basin (Fig. 3). It represents the southeastern portion of the L'Aquila Basin, confined between the southern foothills of the Gran Sasso Range to the north and the Ocre Mounts ridge to the south. To the NE, it is bounded by several normal faults (Figs. 2 and 3): the Paganica–San Demetrio fault system and the Barisciano–San Pio fault system. Conversely, the SW flank shows a more regular and rectilinear trend, defined by the presence of the antithetic Bazzano-Fossa fault (Falcucci et al., 2011, 2015; Galli et al., 2011; Giaccio et al., 2012; Blumetti et al., 2013; Storti et al., 2013; Santo et al., 2014).

Infilling continental deposits of the PSC Sub-basin have been studied since early 1970s, by Bosi and Bertini (1970), who identified the "Valle Valiano" breccia deposits and "Fluvio-lacustrine lower complex," made up of different formations showing heteropic relationships among each other. They are characterized by gravels, fluvial conglomerates, and lacustrine silty deposits, among which is the "Limi calcarei di San Nicandro." The older continental sediments date back to lower Pleistocene–?upper Pliocene. Following the ratification of the new Quaternary chronostratigraphy (Gibbard et al., 2009), this age interval corresponds to Calabrian–?Gelasian (early Pleistocene). Subsequently, during the middle Pleistocene, the deposition of the "Fluvio-lacustrine upper complex" occurred, followed by a stage mainly dominated by fluvial and alluvial fan deposits, likely during the late Pleistocene (Bosi and Bertini, 1970).

Bertini and Bosi (1993) suggested a new stratigraphic framework of the Quaternary continental deposits of the PSC Sub-basin, recognizing five distinct sedimentary cycles: (1) "Ciclo di Poggio Picenze," defined by five stratigraphically related formations deposited in lacustrine-to-marginal lacustrine environments, from slope breccia deposits to silty lacustrine sediments, and to fluvial gravels; (2) "Ciclo di Vall'Orsa," characterized by fluvial conglomerates showing clinostratifications, related to a fan delta facies; (3) "Ciclo di Valle dell'Inferno," made up by gravels and fluvial conglomerates with parallel stratification; (4) "Ciclo di S. Giovanni," which is defined by alluvial fan sediments, made up of sands and gravels; and (5) "Ciclo di S. Mauro," made up of stratified gravels and sandy silts to silty sands deposits. Based on regional correlation, the PSC Sub-basin continental succession can be related to the temporal interval spanning from the early Pleistocene to the middle Pleistocene (Bertini and Bosi, 1993; Bosi et al., 2003).

Following these pioneering studies, many other authors have tried to refine the stratigraphic setting of the PSC Sub-basin fill deposits (Centamore et al., 2006; Galli et al., 2010; Giaccio et al., 2012; Pucci et al., 2015; Spadi et al., 2016; Nocentini et al., 2018; Cosentino et al., 2019). The oldest deposits cropping out in the PSC Sub-basin are related to a lacustrine environment and pertain to the San Demetrio synthem (Spadi et al., 2016).

A complete facies-tract, from deep lacustrine sediments (e.g., San Nicandro Formation [SNF]) consisting of whitish calcareous silty deposits, to subaerial slope deposits (e.g., Valle Valiano Formation [VVF]) made up of alluvial fan and slope debris, defines the upper Pliocene–lower Pleistocene sedimentary succession of the PSC Sub-basin (Spadi et al., 2016; Nocentini et al., 2018; Cosentino et al., 2019). This facies-tract includes lacustrine marginal breccia deposits (e.g., Madonna della Neve Formation [MNF]) consisting of calcareous breccia with lacustrine whitish calcareous silty matrix, and well-developed lacustrine delta and coastal facies (e.g., Valle Orsa Formation [VOF]) containing deltaic lacustrine conglomerates and carbonate sandstones.

During the sedimentation of these post-rift successions, the extensional tectonics that created the L'Aquila intermontane basin continued to be episodically active, as evidenced by some soft sediment deformation (possibly seismites) affecting the stratigraphic successions of the L'Aquila Basin (e.g., Storti et al., 2013; Tallini et al., 2019).

Although the continental deposits of the PSC Sub-basin have been studied for a long time, starting from the 1970s (e.g., Bosi and Bertini, 1970), some elements of knowledge are still lacking. The thickness of the basin filling sequence has only been estimated from indirect data, while the age of the basal deposits filling the deepest depocenters is completely unknown. Furthermore, nothing is known about how the orbital forcings that determined the Quaternary glacial/interglacial cyclicity impacted the deposition of the San Nicandro lacustrine sediments.

3. MATERIAL AND METHODS

3.1. The PSC Sub-Basin and the Castelnuovo 1 Sediment Core (CN-1)

The PSC Sub-basin, like the rest of the L'Aquila Basin, is characterized by a complex tectonic setting, consisting of structural highs and lows (Fig. 2), which defines three main depocenters: Bagno, San Demetrio, and Castelnuovo (Civico et al., 2017; Florio et al., 2021). The CN-1 borehole was drilled at the northeastern margin of the Castelnuovo depocenter, at the top of the Castelnuovo Hill (864 meters above sea level [masl]; 42°17′41.26″N, 13°37′45.20″E). From the CN-1 borehole, a 230-m-long sediment core was recovered in October/November 2018. The core was stored at the core repository of Consiglio Nazionale delle Ricerche–Istituto di Geologia Ambientale e Geoingegneria (CNR-IGAG, Montelibretti, Rome, Italy), where it was subsequently cut in half lengthwise. On one of the halves, sampling operations were carried out for all the planned laboratory analyses (calcimetry, ostracods, diatoms, pollen, magnetostratigraphy, tephra, stable isotopes, and clumped isotopes). The other half of the core was taken to the Consiglio Nazionale delle Ricerche–Istituto di Scienze Marine (CNR-ISMAR) laboratories in Naples, Italy, where measurements of the physical properties were carried out. Half of the sediment core was sampled with various resolutions for different analyses. A total of 4221 samples, 1 cm thick, were collected every 5 cm for geochemical analyses. For magnetostratigraphy, 219 oriented samples were collected every meter and labeled CNM; each sample was split into two specimens to be processed with thermal and alternating field (AF) demagnetization. For palynological and ostracod analyses, samples (respectively labeled CNP and CNO) were taken, at the same level, every 50 cm, for a total of 426 samples each. Moreover, each tephra level was collected for mineralogical and geochemical analyses.

3.2. Physical Property Measurements

Volume magnetic susceptibility and X-ray fluorescence (XRF) measurements for all recovered 223 m of fine-grained deposits were performed. The parameters were measured continuously at 2 cm intervals using a fully automated GEOTEK Multi-Sensor Core Logger at the CNR-ISMAR Petrophysical laboratory. All 223 m were measured in sequential core sections and logged in a continuous process, graphically displayed in real time on a computer. The volume magnetic susceptibility measurements were performed throughout the Bartington Instrument MS2 System furnished with a MS2EI point sensor, which performs measurements with high spatial resolution along split cores. The ex situ XRF measurements were carried out using an Olympus DP-6000 Delta XRF spectrometer (4 W X-ray tube with Rh anode, silicon drift detector, high count rate up to 300,000 cps). The core

was covered with thin plastic wrap to measure light elements (i.e., Mg, Si) too. The XRF scanning for elemental quantification (from Mg to U detectable in ppm concentrations) was operated at 40 keV and 10 keV in a two-beam proprietary configuration known as mining plus mode. Standardization of the instrument was accomplished using the Innov-X "316" stainless steel alloy clip. The calibration was made at the Olympus factory using certified reference materials (i.e., Analytical Reference Materials International and U.S. National Institute of Standards and Technology). Scanning was conducted for 40 s and 20 s per beams, for a total of 60 s per scan. Reporting of each detected element includes the individual elemental concentration, along with individual elemental standard deviation, defined as three times the standard error.

3.3. $CaCO_3$ Content (Calcimetry)

$CaCO_3$ values (wt%) of 2008 samples, from carbonate silts to silty clays and over-consolidated grayish clays, were analyzed at a 10 cm resolution along the whole stratigraphic record of the Castelnuovo 1 borehole, starting from −2.04 m to −220.24 m depth. Calcimetric analyses were carried out at the laboratory of Paleoclimatology and Geoarchaeology of the Dipartimento di Scienze della Terra, Pisa University, Italy, with a DeAstis calcimeter and at Dipartimento di Scienze, Roma Tre University, Italy, using a Dietrich-Fruhling calcimeter. In both cases, wt% of $CaCO_3$ is calculated from the volume of CO_2 released during digestion with HCl 6N. Measurements are calibrated against samples of pure $CaCO_3$. The associated uncertainty is ±5% of the total weight.

3.4. Ostracod Analyses

Samples for ostracod analyses were disaggregated in a 5% H_2O_2 solution, washed under tap water on 0.066-mm and 0.125-mm mesh sieve size, and dried in an oven. Ostracod specimens were handpicked under a Leica S9D stereomicroscope and identified following Spadi et al. (2016).

3.5. Pollen Analysis

A total of 224 pollen samples were processed following the standard chemical-physical procedure at the Department of Earth Sciences, University of Florence, Florence, Italy. Dry samples were first weighed (4.5–23 g), and one *Lycopodium* tablet was then added to each sample to provide pollen concentration. The procedure also included treatments with 20% hydrochloric acid (HCl), 48% hydrofluoric acid (HF), sodium hexametaphosphate [$(NaPO_3)_6$] and 10% potassium hydroxide (KOH). Residues were sieved at 10 μm and then mounted in glycerine. Transmitted light microscopy, with ×1000 (oil immersion) magnification, was used for pollen identification and counting.

Pollen analyses were summarized by the curves of arboreal plants (AP) pollen percentages, and the pollen temperature index, which corresponds to the mesothermic arboreal taxa (e.g., *Quercus* spp., *Carpinus* and *Carya*) versus steppic taxa (*Artemisia* and *Ephedra*) ratio to discriminate warm-temperate from cold phases (e.g., Suc et al., 2010; Bertini et al., 2015).

3.6. Clumped Isotope Thermometry

The carbonate clumped isotope technique (Eiler, 2007) is based on the thermodynamic preference of two heavy, rare isotopes (^{13}C-^{18}O) to bind with each other within the mineral lattice. The number of ^{13}C-^{18}O bonds in carbonate, quantified as Δ_{47}, increases as temperature decreases. The Δ_{47} value is thus a direct proxy for the temperature at which the carbonate precipitated. Clumped paleothermometry has primarily been applied to reconstruct paleoclimate using marine carbonate (e.g., Peral et al., 2020; Marchegiano and John, 2022; Agterhuis et al., 2022; Meckler et al., 2022) and to a lesser extent in continental archives such as speleothems (e.g., Affek et al., 2008; Nehme et al., 2023; Peral et al., 2024) and lake sediments (e.g., Huntington et al., 2010; Grauel et al., 2016; Hudson et al., 2017; Yue et al., 2022; Marchegiano et al., 2024a).

A total of five samples of authigenic lacustrine carbonate were selected to perform Δ_{47} analyses. The selection was based on the variation of carbonate content throughout the record, as determined by calcimetry analyses, most probably linked to paleoclimate/paleoenvironmental changes. Scanning electron microscope analyses were performed on the selected samples to exclude the presence of allogenic carbonates. To ensure homogeneity, samples were crushed into a fine powder using an agate mortar. The Δ_{47} analyses were carried out at the Archaeology, Environmental Changes and Geo-Chemistry clumped isotope lab of the Vrije Universiteit Brussel (VUB), Brussels, Belgium, using a Nu Instruments Perspective-IS stable isotope ratio mass spectrometer in conjunction with a Nu-Carb carbonate sample preparation system, as described in De Vleeschouwer et al. (2022). The analyses were performed between October and December 2021 during five sessions of measurements. The carbonate powder reacted for 10 min with 105% H_3PO_4 at 70 °C. To ensure the consistency of the analyses, each sample measurement was replicated between 6 and 10 times. The Swiss Federal Institute of Technology, Zurich, Switzerland (ETH) standards (Meckler et al., 2014) were measured following the recommendations of Kocken et al. (2019) with a sample-to-standard ratio of 1:1. The carbonate standard ETH-4 was systematically measured and compared to InterCarb values (Bernasconi et al., 2018, 2021) to ensure the measurements quality control. Analyses and results were monitored using the Easotope software (John and Bowen, 2016). The raw measured Δ_{47} values were processed using the International Union of Pure and Applied Chemistry (IUPAC) Brand's isotopic parameters (Brand et al., 2010; Daëron et al., 2016; Petersen et al., 2019) and converted to the ICDES 90 °C scale, using the most recent values for the ETH-1, ETH-2, and ETH-3 carbonate reference materials (Bernasconi et al., 2021) within the ClumpyCrunch software (Daëron et al., 2016; Daëron, 2021). Both analytical and calibration uncertainties were propagated to calculate the final uncertainties on temperatures.

3.7. Magnetostratigraphy

In the Castelnuovo borehole, we collected 216 handpicked blocks from different stratigraphic levels of the core for paleomagnetic analyses. From each block, two cubic twin specimens were cut. The azimuth of the specimens is not defined, as the borehole cores were not oriented in the horizontal plane with respect to the geographic north. Therefore, we used only paleomagnetic inclination to define the magnetic polarity of the sampled blocks.

Paleomagnetic analyses were carried out at the paleomagnetic laboratory of the Istituto Nazionale di Geofisica e Vulcanologia (INGV, Rome, Italy). The natural remanent magnetization (NRM) of standard cubic specimens (10 cc) was measured using a 2-G Enterprises superconducting rock magnetometer equipped with DC-SQUID coils within a magnetically shielded room. Specimens were subjected to progressive stepwise demagnetization using both alternating field (AF) and thermal procedures.

We applied a stepwise AF demagnetization to one specimen from all sampled blocks, spanning the whole borehole stratigraphic interval (218 specimens), using a set of three orthogonal AF coils mounted in-line with the superconducting rock magnetometer system, with 5–10 mT increments of the peak field up to 20 mT, followed by 20 mT steps up to 100 mT. We applied stepwise thermal demagnetization to 179 specimens taken (from the top of the hole) between −3 m and −30 m and between −61 m and −218 m, as a further check for the magnetic signal defined with the AF demagnetization procedure. Ther-

mal demagnetization was carried out using 30–50 °C temperature increments until the NRM decreased below the limit of instrument sensitivity or random changes appeared in the paleomagnetic directions.

The analysis of the demagnetization data was carried out by using the DAIE software (Sagnotti, 2013), applying principal component analysis on at least four consecutive demagnetization steps, to determine the ChRM (characteristic remanent magnetization) direction for each specimen, and the maximum angular deviation (MAD) was computed for each determined ChRM direction.

For specimens demagnetized by AF, we computed the ΔGRM/ΔNRM ratio, which provides a quantitative measure of the tendency to acquire a spurious gyromagnetic remanent magnetization (GRM) at high AF steps (Fu et al., 2008). ΔGRM is computed as the difference between the final intensity measured at the last applied AF step and the intensity minimum value (MV) measured during the whole AF treatment; ΔNRM is the difference between the initial NRM intensity and MV.

3.8. Tephra Analysis

Eight tephra layers were identified and collected from the Castelnuovo lacustrine succession, six from the core CN-1 (CN-29.38, CN-30.95, CN-60.40, CN-73.02, CN-104.37, and CN-104.66; numbers following CN- identify the depth in m) and the other two (SNC-1 and SNC-2) from outcropping levels exposed in the "il Faccione" section (Spadi et al., 2016) and on the walls of a cellar in Castelnuovo village (Figs. 4A–4C and 5), respectively. Major and minor element compositions acquired on glass shards from the layers CN-29.38, from core CN-1, and SNC-2 from outcrop, are herewith reported, with the aim to support relationships between sediments and tephra layers at subsurface and in outcrop, and thus to use mutual information deriving from both contexts (Fig. 4).

The analyses were carried out at the CNR-IGAG using a Cameca SX50 electron microprobe equipped with five wavelength dispersive spectrometers. Operating conditions were set to 15 kV accelerating voltage; 15 nA beam current; 10–15 μm beam diameter; 20 s per element counting time; Wollastonite (Si and Ca), corundum (Al), diopside (Mg), andradite (Fe), rutile (Ti), orthoclase (K), jadeite (Na), phlogopite (F), potassium chloride (Cl), barite (S), and metals (Mn) were used as standards. The Ti content was corrected for the overlap of Ti-Kα peaks. To evaluate accuracy and precision three international secondary standards (Kakanui augite and rhyolite RLS132 glasses from the U.S. Geological Survey) were measured prior of each analytic run.

3.9. $^{40}Ar/^{39}Ar$ Geochronology

The new $^{40}Ar/^{39}Ar$ ages reported herein were obtained via small-population multi-grain analyses of phenocrystic plagioclase from a fine-grained, vitric (almost aphyric) tephra sample (SNC-2). The plagioclase phenocryst separates were obtained by standard mineral separation techniques: hand-crushing, concentration of feldspars using a Frantz Isodynamic separator, washing in distilled water and dilute HCl, followed by hand-picking under a polarizing binocular microscope. The maximum grain size available in the sample was obtained and used in the analyses (200–300 μm). The separate was irradiated in the Cadmium-Lined On-Periphery Irradiation Tube (CLOPIT) of the Oregon State University TRIGA reactor for 0.83 h. Sanidine phenocrysts from the Alder Creek Rhyolite of California (orbitally referenced age = 1.1848 ± 0.0006 Ma; Niespolo et al., 2017) were used as the flux monitor. Reactor-induced isotopic production ratios for these irradiations were $(^{36}Ar/^{37}Ar)$ $Ca = 2.65 \pm 0.02 \times 10^{-4}$; $(^{38}Ar/^{37}Ar)$ $Ca = 1.96 \pm 0.08 \times 10^{-5}$; $(^{39}Ar/^{37}Ar)$ $Ca = 6.9 5 \pm 0.09 \times 10^{-4}$; $(^{37}Ar/^{39}Ar)$ $K = 2.24 \pm 0.16 \times 10^{-4}$; $(^{38}Ar/^{39}Ar)$ $K = 1.220 \pm 0.003 \times 10^{-2}$; and $(^{40}Ar/^{39}Ar)$ $K = 2.5 \pm 0.9 \times 10^{-4}$. Atmospheric $^{40}Ar/^{36}Ar = 298.56 \pm 0.31$ (Lee et al., 2006) and decay constants were according to Min et al. (2000). All analyses were performed at the Berkeley Geochronology Center, Berkeley, California, USA, on a Nu Instruments Noblesse noble-gas mass spectrometer employing a high-efficiency ionization source, simultaneous multi-isotope measurement, and all ion-counting detectors.

Following several weeks of radiological "cooling" after irradiation, the feldspars were analyzed in small aliquots (~5–6 crystals) by the $^{40}Ar/^{39}Ar$ technique using two laser-heating methods, multi-crystal total fusion (MCTF) and multi-crystal incremental heating (MCIH). In the MCTF technique, the feldspar population was exposed under ultra-high vacuum to a diffuse laser beam at low power to drive off surficial gasses, then fused and analyzed with a focused beam in a single step. Four MCTF analyses were performed (Table S1 in the Supplemental Material[1]).

In the MCIH technique, the phenocryst population was incrementally heated in 4–8 steps at progressively increasing power to fusion, to better examine the argon systematics of the material (consistency of release patterns in terms of age, radiogenic content, and chemical composition), more effectively drive off surficial and trapped atmospheric contamination, and maintain fairly consistent gas yields. A total of 23 MCIH analyses on four small-population batches of phenocrysts were performed (Table S2).

3.10. Cyclostratigraphy and Age Modeling

Spectral analysis has been shown to be a useful statistical tool in analyzing climatic records to determine periodic or quasi-periodic characteristics. Spectral analysis of $CaCO_3$ percentages have been performed to identify and quantify the influence of orbital periodicities in the sedimentation history of the PSC Sub-basin succession.

The Castelnuovo deep borehole spectral analysis was carried out on calcimetry data along all the sediment core. For the data processing, the Acycle software, an open-source software designed for time series analysis in paleoclimate research, was used (Li et al., 2019). The identification of potential astronomical signals in the calcimetric record involved a sequence of steps. The first was checking the presence of possible empty values or averaging multiple values assigned to the same depth. Second, the series was interpolated with a constant 10 cm sampling interval. Then, to remove long-term trends, detrending was applied to ensure that data variability oscillates around a mean of zero.

We applied the LOWESS (locally weighted scatterplot smoothing) detrending method, with a smoothing window that is 35% of the total length of the data series (standard value). The result is detrended data, situated along the zero mean, with a 76.37 m LOWESS trend removed. Subsequently, the detrended time series underwent power spectral analysis to detect and recognize periodic or quasi-periodic components in the dataset (Weedon, 2003), which are represented through a periodogram in the form of spectral density peaks related to specific dominant frequencies.

The power spectrum can be evaluated with various nonparametric or parametric approaches; hence, according to our time series, the multitaper method estimator has been used, because it represents an optimal trade-off between frequency resolution and statistical confidence for uniformly spaced time series (Thomson, 1982). Furthermore, we settled on a conventional AR(1) (autoregressive) modeling option, which allowed us to display the red-noise fit to the spectrum with 90%, 95%, 99%, and 99.9% confidence

[1]Supplemental Material. Multi-crystal total fusion and incremental heating data tables, clumped carbonate isotope analyses data, major element composition of SNC-2 tephra, sediment core figures, demagnetization plots, and calcimetry data series periodograms and frequencies. Please visit https://doi.org/10.1130/GSAB.S.29944145 to access the supplemental material; contact editing@geosociety.org with any questions.

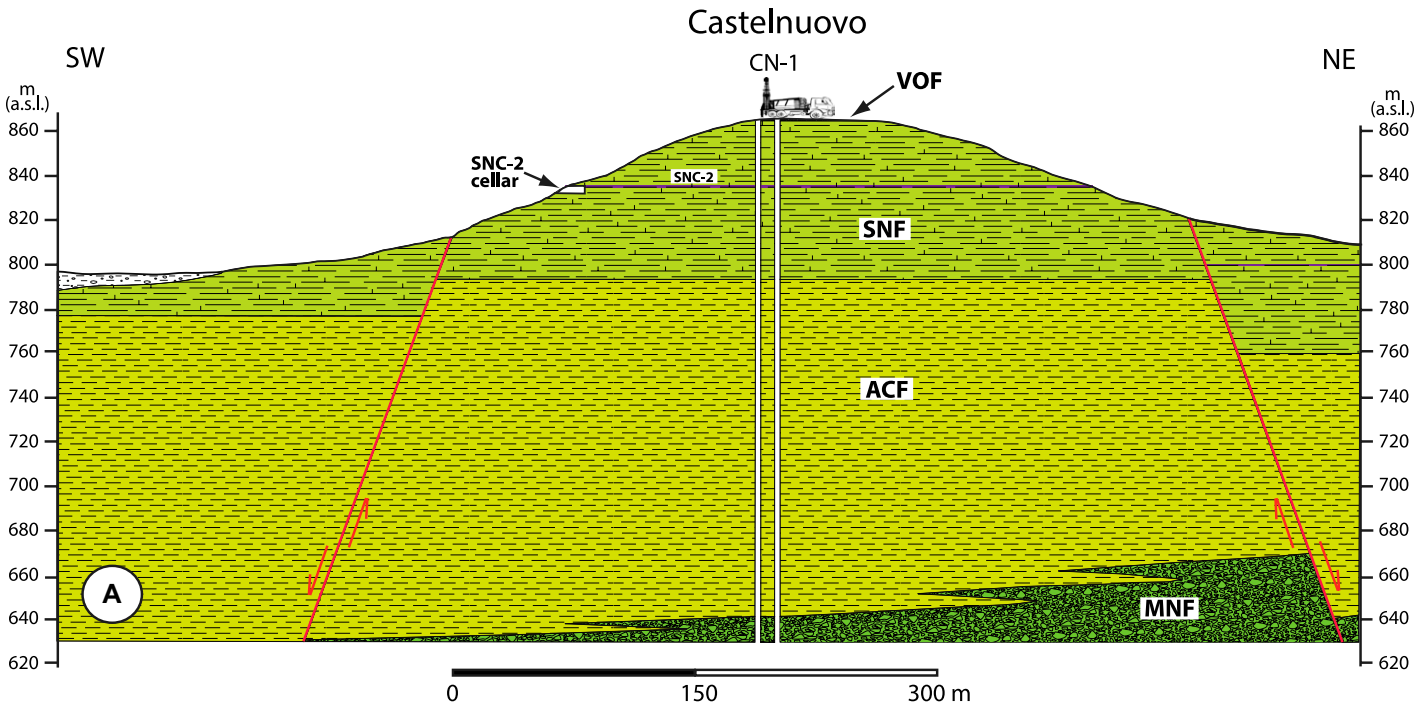

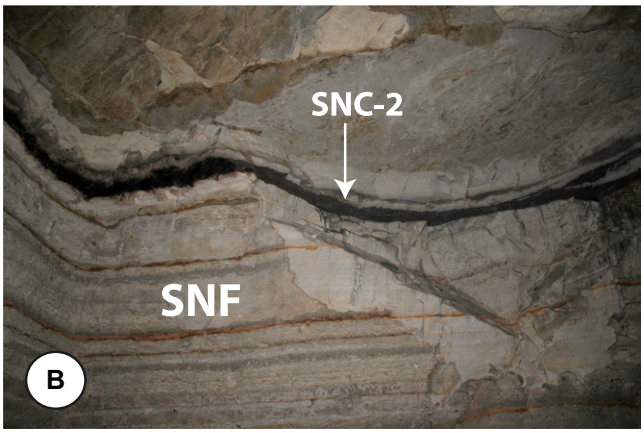

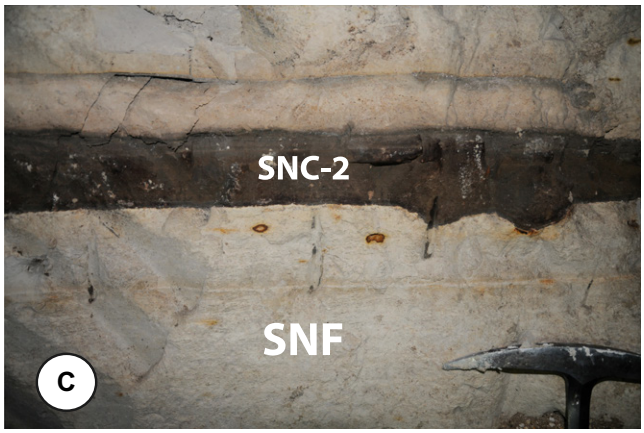

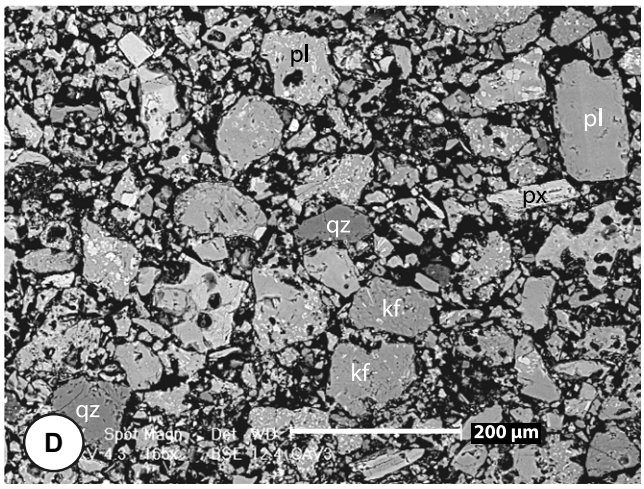

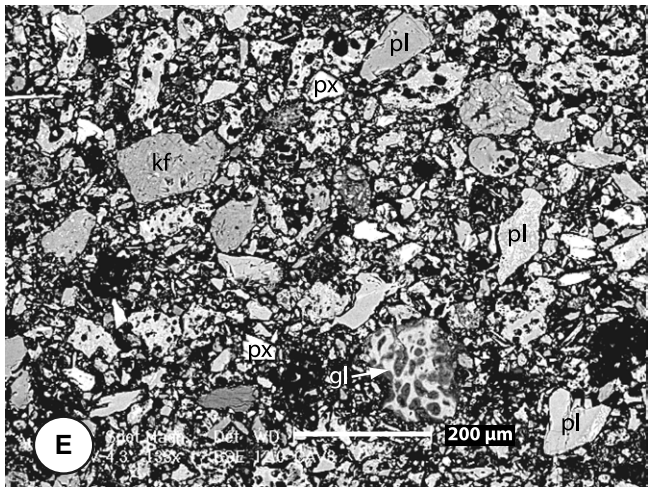

Figure 4. (A) Geological profile crossing the Castelnuovo Hill where the CN-1 borehole was drilled. The figure also shows the cellar from which the SNC-2 tephra, dated by the $^{39}Ar/^{40}Ar$ method, was sampled. ACF—Argille di Castelnuovo Formation; MNF—Madonna della Neve Formation; SNF—San Nicandro Formation; VOF—Valle Orsa Formation. (B) Cellar walls and ceiling showing the location of the SNC-2 tephra layer within the white calcareous silts of the San Nicandro Formation (SNF). (C) Close-up of the SNC-2 tephra layer. (D, E) Scanning electron microscope images showing texture and mineralogy of the SNC-2 tephra layer. pl—plagioclase; qz—quartz; kf—K-feldspar; px—pyroxene; gl—glass shard.

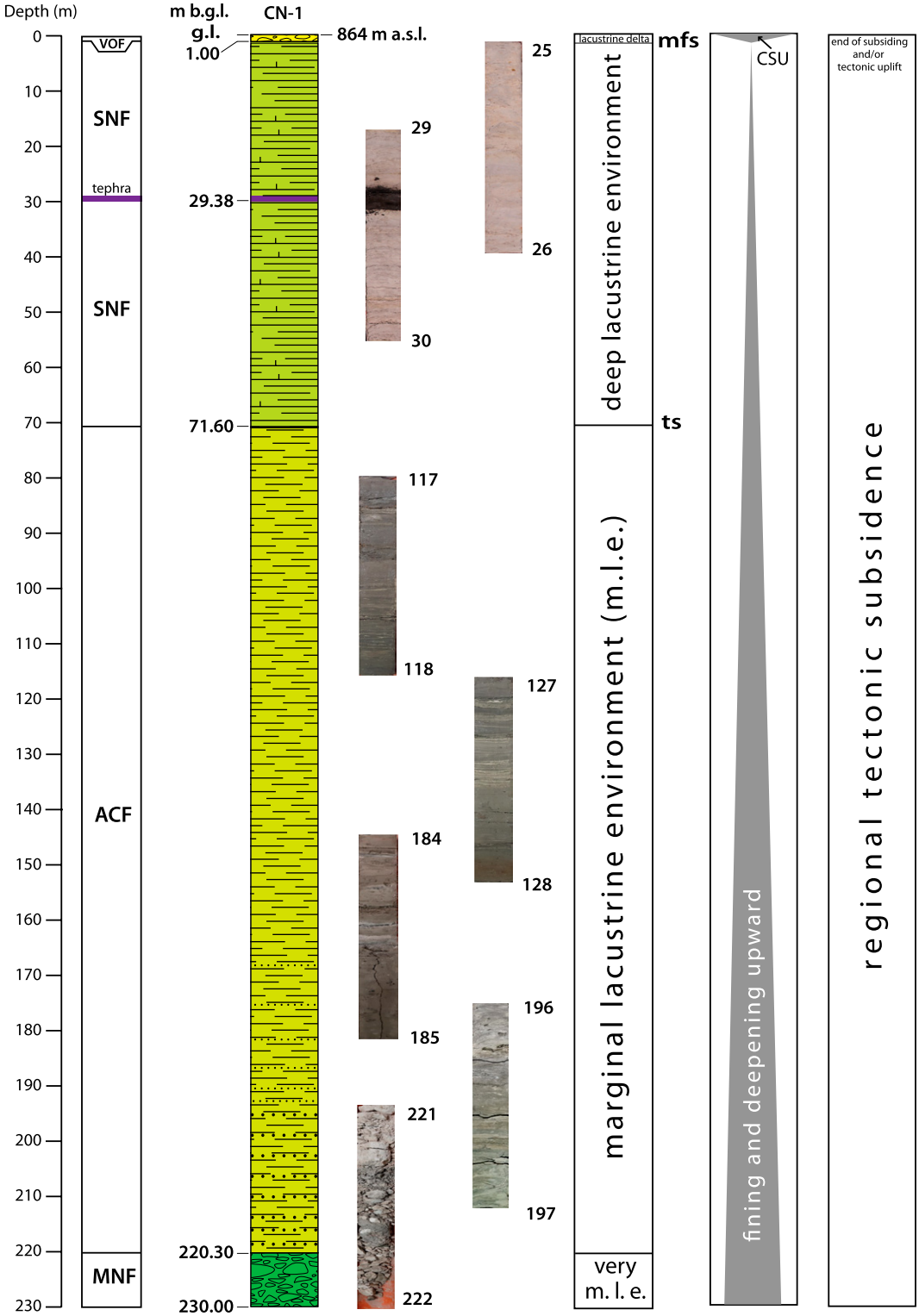

Figure 5. Stratigraphy of the CN-1 borehole with indications of paleoenvironments, depositional trends, and tectonic subsidence and uplift. MNF—Madonna della Neve Formation; ACF—Argille di Castelnuovo Formation; SNF—San Nicandro Formation; VOF—Valle Orsa Formation; CSU—coarsening and shallowing upward; ts—transgressive surface; mfs—maximum flooding surface.

limits that are based on the best fit to the power of the median-smoothed background spectrum.

Afterward, the detrended calcimetry series was analyzed on an evolutionary fast Fourier transform spectrogram to inspect how major frequencies evolve across stratigraphic intervals. Wavelet transform analysis was used to analyze localized variations of power within our time series. By decomposing the time series into time-frequency space, we were able to determine both the dominant modes of variability and how those modes vary in time (Torrence and Compo, 1998).

Finally, filtering allowed us to isolate specific frequency components, which have been used to build an age model, defining the orbital forcing we expect to be related to that specific frequency, and then, through the obtained age model, set the tuned data in the time domain.

4. RESULTS

4.1. Lithostratigraphy

The CN-1 borehole, located at the top of the Castelnuovo Hill (Fig. 3), reached a depth of 230 m below ground level. Pictures from the recovered CN-1 sediment core have been added in the Supplemental Material (Figs. S1–S10). In this section, we first describe the sediment core and then define the formations it cuts through.

The upper part of the well-log matches the outcropping succession of the Castelnuovo Hill (Figs. 4 and 5), where the boundary between the SNF and the VOF crops out (Nocentini et al., 2018; Fig. 3). CN-1 drilled 1 m of gravel/conglomerate of the VOF before penetrating the SNF (Spadi et al., 2016; Nocentini et al., 2018), which is defined by cyclic alternations of white calcareous silts and light-gray clayey-silts couplets, often separated by a thin oxidized silty-sandy layer.

Between −71.60 m and −118.80 m clayey levels start, becoming more abundant and thicker, while organic-rich clay levels appear (Fig. 5). From −118.80 m to −154.70 m, calcareous silty levels become occasional and thin, in favor of laminated, over-consolidated, organic-rich clays, which are predominant (Fig. 5). From −154.70 m to −194.80 m, the succession is formed by alternations of clayey-silts and laminated whitish calcareous silts, while down to −220.30 m, it is composed of alternations of clays, marls, and clayey-gravels, with coarser sediments becoming more and more frequent. Below −220.30 m down to the bottom (−230.00 m), fine-grained deposits almost disappear, passing to coarse polygenic gravels and calcareous breccias with rare clayey-silty layers (Fig. 5).

The CN-1 sediment core shows clear cyclicities in color changes, from white, light- and dark-gray, to black (Figs. S1 and S2). These changes occur with several periodicities, from millimeter-scale to multi-meter-scale. In some intervals of the sediment core, varved-like sediments occur (Figs. S1, S2, and S3), and single outsized (centimeter-scale) carbonate clasts ("lone-stones" of Frakes and Francis, 1988) have been found in the fine-grained deposits of both the SNF and Argille di Castelnuovo Formation (ACF; Figs. S4, S5, and S6). These clasts can be interpreted as "dropstones," as defined by Bennett et al. (1996), which may form either by deposition from a raft or as a projectile.

The stratigraphic succession drilled by the CN-1 borehole can be partly linked to the stratigraphic units known in outcrop in the PSC Sub-basin, such as the VOF conglomerates, intersected in the first meter of the borehole, the SNF, which was intersected from −1 m to −71.60 m (Fig. S7), and the MNF polygenic breccias, which crop out close to the Castelnuovo Hill, crossed from −220.30 m to the bottom of the borehole.

Between the SNF and the MNF, the borehole drilled, from top to bottom, gray clays with organic-rich clay levels, laminated over-consolidated organic rich clays, clayey silts and laminated whitish calcareous silts with thin sandy levels (Fig. S8), clays, marls, and clayey-gravels with coarser sediments becoming more frequent with depth (Figs. S9 and S10).

These predominantly clayey lithologies are not known in outcrop in all of the L'Aquila Basin, but have been encountered in a borehole to the SE of Castelnuovo Hill (CN2 in Spadi et al., 2022). From a lithostratigraphic point of view, the predominantly clayey lithologies encountered between −71.60 m and −220.30 m differ from both the overlying SNF, which is characterized by white calcareous silts, and the underlying polygenic breccias of the MNF (Fig. 5). For this reason, it is necessary to define a new formational unit, between the SNF and the MNF, which consists mainly of clay lithofacies, which we here refer to as the Argille di Castelnuovo Formation (ACF; Fig. 4). In the CN-1 borehole the ACF shows a thickness of ∼149 m.

4.2. Petrophysical Results

All magnetic susceptibility (MS), iron (Fe) and sulfur (S) contents were measured on a centimeter scale, to obtain high-resolution stratigraphic curves to better understand the variations of magnetic minerals along the cores (Fig. 6). The MS and Fe variation logs (Figs. 6A and 6B) show values from -15×10^{-5} SI to 162.7×10^{-5} SI (mean 1.7×10^{-5} SI) and from 0 ppm to 77,498 ppm (mean 2164 ppm), respectively. Both datasets are dominated by oscillating patterns around the mean values and show, together with the S log (from 0 ppm to 86,788 ppm, mean 869.5 ppm; Fig. 6C), clear peaks and rapid variations along the sediment core.

All three parameters, moving from the SNF down to the ACF, show drastic variations in intensity values at approximately −80 m. Thus, the parameter trends are described separately in the intervals from 0 m to −80.0 m and from −80.0 m to −218 m.

4.2.1. Interval from 0 m to −80 m

The MS values, excluding the maximum MS value of 162.7×10^{-5} SI corresponding to the tephra layer recognized at 29.38 m, range from -15×10^{-5} SI to 68.6×10^{-5} SI with an average value of -2.2×10^{-5} SI. The Fe curve varies from 0 ppm to 12,392 ppm (average 796 ppm). S is not present along the sediment core down to −50 m, while only a few peaks, the highest of which is of 8670 ppm at −51.24 m, appear in the remaining part of the core.

4.2.2. Interval from −80 m to −218 m

A general increase in the intensity values of all petrophysical logs is observed, in particular MS varies from -15.5×10^{-5} SI to -132.5×10^{-5} SI (mean 4.0×10^{-5} SI), Fe values range from 0 ppm to 77,498 ppm, with a mean of 3010 ppm, and S varies from 0 ppm to 86,788 ppm, with a mean of 1368 ppm. In this section of the sediment core, the highest values of Fe and S are found in two intervals, characterized by siliciclastic clay rich in organic matter, from −80 m to −90 m and from −190 m to −218 m. In the first interval, in particular, both Fe and S show average values, 9468 ppm and 14,442 ppm, well above the sediment core averages (3010 ppm and 1368 ppm), respectively. A different situation is observed in the interval from −118 m down to −150 m, where laminated, over-consolidated, dark, and organic-rich siliciclastic clays predominate. The facies of sediments in this case suggests probably anoxic depositional environments, as confirmed by the drastic decrease in carbonate input (from 10% to 3%) and by the increase in average Fe of ∼50% compared to the average of the section (4608 ppm and 3010 ppm, respectively).

4.3. Calcimetry ($CaCO_3$ Content)

Carbonate mostly occurs as lacustrine authigenic calcite, linked to the deposition of calcite through picoplankton activity, and as accumulation of autochthonous ostracod carbonate shells, in minor proportion. The $CaCO_3$ record displays marked and periodic oscillation, having different amplitude and average values along the core (Fig. 6D). From −2.04 m to ∼−50 m,

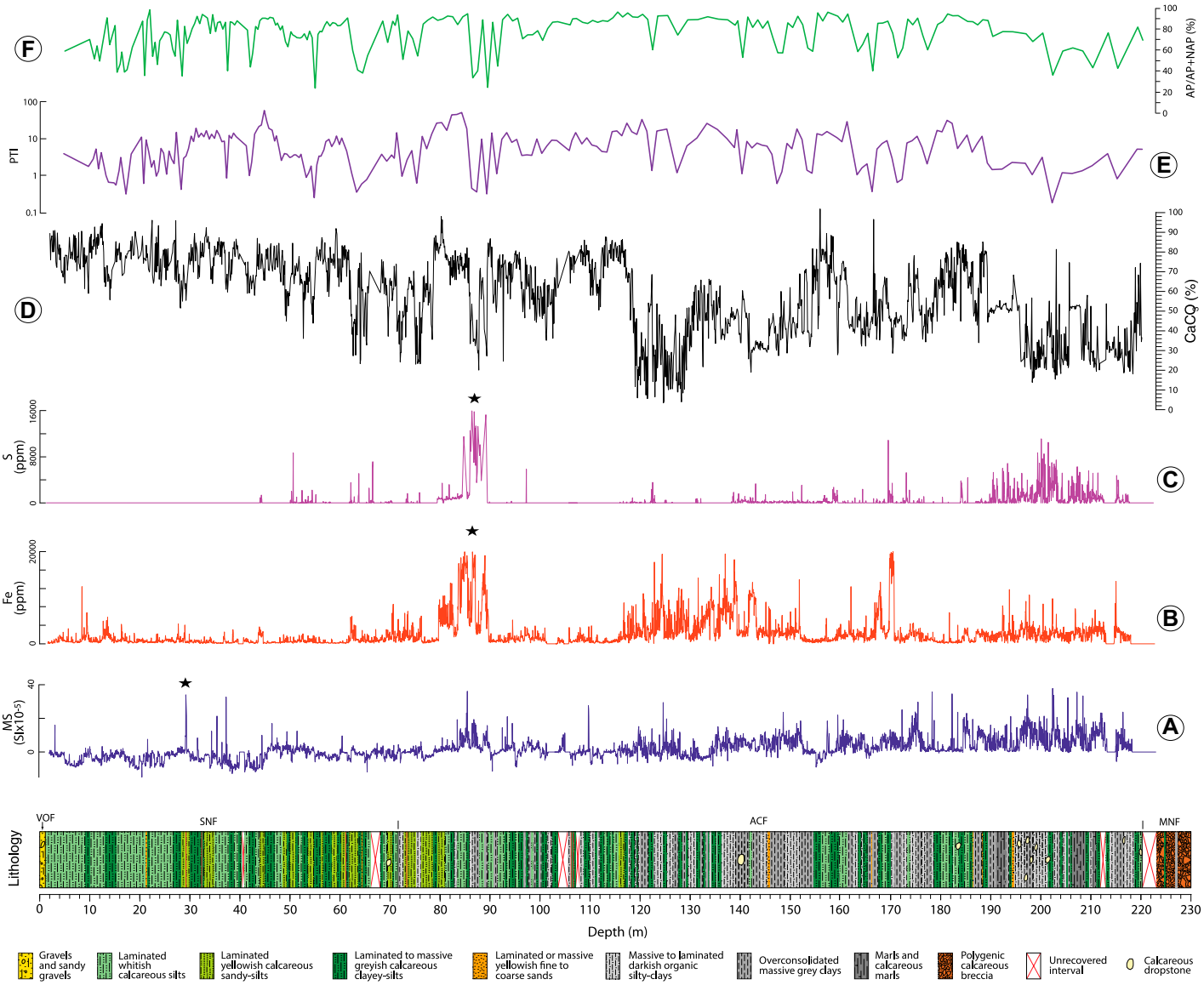

Figure 6. (A) Magnetic susceptibility (MS), (B) iron (Fe), and (C) sulfur (S) variation curves. Black stars indicate higher values in the three records: 162.7 SI × 10^{-5}, 86,788 ppm, and 77,498 ppm, respectively. (D) Raw calcimetry data measured from the CN-1 sediment core. (E, F) Fluctuations, along the CN-1 sediment core, in the records of mesothermic arboreal pollen taxa opposed to those of steppic and semi-desert taxa, expressed by both the pollen temperature index (PTI) ratio (E) and the AP/AP + NAP (arboreal plants, non-arboreal plants) percentages (F). MNF—Madonna della Neve Formation; SNF—San Nicandro Formation; VOF—Valle Orsa Formation.

the $CaCO_3$ content cyclically ranges between 95% and 45%, with an average value of ~75%. Between −50 m and −118 m, the $CaCO_3$ content displays more intense cyclic variations, ranging from almost 100% down to 20%, and slightly decreased average values (~65%). Between −118 m and −129 m, the $CaCO_3$ content reaches the lowest values, ranging between 10% and 3%. From −118 m to −220 m, the signal shows again a prominent cyclic pattern, with $CaCO_3$ content between 15% and almost 90% and an average value of ~50% that decreases to ~30% in the bottom section (~−198 m to −220 m). Overall, the $CaCO_3$ content shows a long-term decreasing trend moving downward in the CN-1 sediment core.

4.4. Ostracod Analyses

The ostracod analyses are still very preliminary, since only 82 samples out of the collected 426 were studied. In particular, only the topmost 30-m-thick calcareous silts (SNF) (from −2.19 m to −31.69 m, 60 samples in total) and the lowermost 11-m-thick silty-clays sediments of the core (ACF; from −209.59 m to −220.24 m, 22 samples in total) were analyzed. Unfortunately, in both intervals the ostracod valves were often fragmented, and only a few of them in each sample were identified at the species level. Thus, it was not possible to perform quantitative analyses.

In the upper portion of the core (SNF), the CNO 1 sample at −2.19 m was sterile and 31 scattered samples bore only fragmented valves, but in the remaining 29 samples, several adult and juvenile valves occurred. Six ostracod species were identified in the upper portion of the core: *Caspiocypris nicandroi* and *Caspiocypris*

vestinae, which were dominant, accompanied by subordinate *Caspiocypris amiterni* and *Caspiocypris bosii*, while *Cypria bikeratia* and *Ilyocypris ilae* were scarce, occurring in only one or two samples. Almost all the species were already known from the SNF cropping out in the surroundings, except for *Ilyocypris ilae*, which was reported only from the younger VOF (Spadi et al., 2016). It is worthwhile to note that *C. amiterni* was absent from −8.15 m to −10.64 m and −11.54 m to −15.19 m, whereas both *C. amiterni* and *C. bosii* were absent from −17.59 m to −25.34 m.

Samples from the lowermost portion of the core (ACF) bore very few ostracod valves, mainly broken and thus not recognizable taxonomically. Only in samples between −209.59 m and −211.69 m it was possible to observe a few adult and juvenile valves of *C. nicandroi* and a broken specimen of *C.* cf. *C. bikeratia*.

4.5. Pollen Analysis

The pollen flora consists of 110 taxa. Total pollen concentration ranges between 115 and 429,174 grains per gram of dry sediment. *Pinus* concentration ranges between 4 and nearly 91,265 grains per gram of dry sediment. Pollen assemblages mainly include taxa with a modern-day wide distribution in South Europe and North Africa. Taxa today with an extra-Mediterranean distribution such as *Taxodium-Glyptostrobus* type are present but in low abundance in the lowest portion, and they are discontinuous and scanty in the middle to uppermost portion.

Among the arboreal plants (AP), *Tsuga* and especially *Carya* are more abundant and continuous; other taxa today restricted in some geographical sectors of the Mediterranean area (such as *Liquidambar* and *Zelkova*), are subordinate. Deciduous oaks (*Quercus*) dominate the temperate broad-leaved forest assemblages whereas the Mediterranean sclerophyll group with scanty pollen grains of evergreen oaks and *Olea* are subordinate. Among the mid- to high-altitude coniferous forest taxa, *Cedrus* is especially abundant followed by *Abies* and *Picea*. Common non-arboreal plants (NAP) include Asteraceae (including *Artemisia*), Poaceae, Amaranthaceae and *Ephedra*, followed by *Plantago*.

Fluctuations in the records of mesothermic arboreal pollen taxa opposed to those of steppic and semi-desert taxa are expressed by both the pollen temperature index ratio (Fig. 6E) and the AP/AP + NAP percentages (Fig. 6F); this allows for the recognition of different climate conditions, according to glacial-interglacial cycles as well as stadials and interstadials (Figs. 6E and 6F).

4.6. Clumped Isotopes

Clumped isotope analyses were performed on authigenic carbonate mainly derived from picoplankton activity, to infer the lake-water temperature variations. Unfortunately, it has been not possible to analyze ostracod carbonate shells, as recently proposed by Marchegiano et al. (2024a, 2024b), due to the scarce number of ostracods recovered along the sediment core. We analyzed five carbonate samples collected from different depths along the sediment core: 14.04 m, 19.69 m, 28.14 m, 86.04 m, and 108.84 m.

The Δ_{47} values of the authigenic carbonate samples range from 0.6058 to 0.6374 with a standard error (1SE) from 0.0084‰ to 0.0101‰ (Table S3). The number of replicates per sample ensures the robustness of the results. The repeatability along the five sessions of the standards used to standardize the results and the carbonate samples is 23.6 ppm and 23.9 ppm, respectively. The ETH-4 standard, used to ensure and control the quality of the analyses, presents a Δ_{47} value of 0.4496 (in Bernasconi et al., 2021, ETH-4 value is 0.4505 ± 0.0018) and 0.0044 1SE for 94 replicates (Table S3). The lake-water clumped-isotope–derived temperatures (Δ_{47}-T) of the five analyzed authigenic carbonate samples are, from top to bottom, 11.5 ± 1.3 °C, 15.4 ± 1.6 °C, 11.3 ± 1.8 °C, 15.6 ± 1.7 °C, and 21 ± 1.7 °C (Table S3).

4.7. Magnetostratigraphy

The stratigraphic trends of selected paleomagnetic and rock magnetic parameters are shown in Figure 7. In particular, Figures 7A and 7B show the characteristic remanent magnetization (ChRM) inclination values for AF and thermal demagnetization, respectively. ΔGRM/ΔNRM values determined from AF demagnetization are shown in Figure 7C, whereas the maximum unblocking temperature (Tub) estimated from thermal demagnetization is shown in Figure 7D. The filtered ChRM inclination data for specimens with ΔGRM/ΔNRM values <0.1 and Tub ≥400 °C are shown in Figure 7E. Finally, Figure 7F shows the resulting magnetic zonation for the CN-1 sediment core.

4.7.1. Paleomagnetism

The demagnetization diagrams indicate stable palaeomagnetic behavior for most of the specimens throughout the CN-1 sediment core (Fig. S11). For all the measured specimens, a ChRM was determined by principal component analysis by fitting a linear component between 5–10 mT and 50–60 mT for the specimens demagnetized by AF and between 120–180 °C and 400–580 °C for the specimens thermally demagnetized.

Since the core was not azimuthally oriented, the magnetic polarity of the specimens was deduced by the paleomagnetic inclination. The analyzed specimens allow a clear recognition of both normal (Figs. S11b and S11e) and reverse (Figs. S11a and S11c) polarity throughout the core, as indicated by downward and upward ChRM inclination, respectively.

The demagnetization data indicate a variable magnetic mineralogy throughout the core. For specimens subjected to AF demagnetization, the acquisition of a GRM during AF demagnetization in AF peaks higher than 40–60 mT is virtually absent for all the specimens in the uppermost 85 m of the core, whereas it was significant for many specimens below −85 m (Fig. 7C). The ΔGRM/ΔNRM values are often higher than 1 for these specimens (e.g., Fig. S11f) and show a maximum peak of 30 measured at −203 m depth. One hundred specimens out of a total of 214 specimens subjected to AF demagnetization show ΔGRM/ΔNRM values <0.1. Fifty-six specimens out of a total of 180 specimens subjected to stepwise thermal demagnetization show a maximum unblocking temperature (Tub) lower than 400 °C (Fig. 7D).

4.7.2. Magnetic Zonation

For most of the specimens, the combination of median destructive field values in the range 20–30 mT, the absence of a significant GRM acquisition during AF demagnetization, and maximum unblocking temperature (Tub) between 400 °C and 580 °C during thermal demagnetization (Fig. 7B) indicate that magnetite is the main magnetic mineral. The combination of a Tub lower than 400 °C, a median destructive field higher than 40 mT, and a significant acquisition of a GRM at high AF demagnetization steps are typical proxies for the occurrence of greigite as a main remanence carrier (e.g., Sagnotti and Winkler, 1999).

The stratigraphic trends of selected rock magnetic parameters (Figs. 7C and 7D) indicate that magnetite and greigite occur in variable proportions throughout the sediment core. The stratigraphic trend of the inclination of the ChRM determined from AF and thermal demagnetization, as shown in Figures 7A and 7B, is generally consistent throughout the core, with some significant exceptions related to the presence of greigite as a main magnetic carrier, as discussed in the following paragraph.

The application of a filter that discards results from specimens characterized by a predominant occurrence of greigite, as indicated by a significant GRM acquisition during the AF treatment

(i.e., ΔGRM/ΔNRM values ≥ 0.1) and by a Tub lower than 400 °C during thermal demagnetization, improves the consistency of ChRM inclination data obtained with the two demagnetization methods (Fig. 7E). Greigite, in fact, is a diagenetic mineral, which can form either as a syn-sedimentary phase or during any later time because of fluid migration and non-steady-state diagenesis (i.e., Roberts and Weaver, 2005; Sagnotti, 2007), and its presence may hamper the reconstruction of a reliable magnetostratigraphy (e.g., Sagnotti et al., 2010).

The filtered ChRM inclination trend (Fig. 7E) allows the identification of six clear magnetozones, indicated as N1 to R3 in Figure 7F. Magnetozones are defined as intervals with adjacent specimens with consistent paleomagnetic inclination. Each magnetozone is defined by specimens with ChRM inclinations that are almost antipodal from the neighboring magnetozones and are of definite normal or reversed polarity.

Two stratigraphic intervals are left with undefined polarity (Fig. 7F): the upper one is between −7 m and −11 m depth, where specimens treated with AF and thermal demagnetization provide inconsistent results; the lower one is between −111.5 m and −150 m depth, where all the specimens are characterized by the predominance of greigite as main magnetic carrier. The uppermost reliable sample in the core is of reverse polarity, but it is a single sample, and it is not sufficient to define a robust magnetozone.

4.8. Tephra Major Element Composition and Core Outcrop Tephra Correlation

The tephra layer SNC-2, which we dated using ^{40}Ar-^{39}Ar geochronology (see section 4.9), occurs at an elevation and stratigraphic height consistent with that of the layer CN-29.38 found in the CN-1 sediment core at ~30 m (Figs. 4A and 5). The two layers share similar lithological and textural characteristics (Figs. 4D and 4E). They are both ~10 cm thick and blackish in color (Figs. 4B, 4C, 5, and S7). Both layers are made of brownish, poor vesicular, glass shards, dotted by abundant microliths, accompanied by scarce loose crystals of feldspar and clinopyroxene. Major element analyses of the glass shards of both layers reveal strong compositional similarities, with silica contents ranging from 56 wt% to 65 wt% and alkali sum from 5 wt% to 9 wt%, respectively (Table S4; Fig. 8). In the total alkali versus silica classification diagram (Le Bas et al., 1986), the composition of glass shards from both layers plots mainly in the field of latite, with some least and most evolved glass shards straddling, respectively, the fields of basaltic andesite and shoshonite and the field of trachyte (Fig. 8). Based on the very similar stratigraphic, lithological, and geochemical characteristics, SNC-2 and CN-1 can be thus reliably recognized as stratigraphic occurrences of the same tephra.

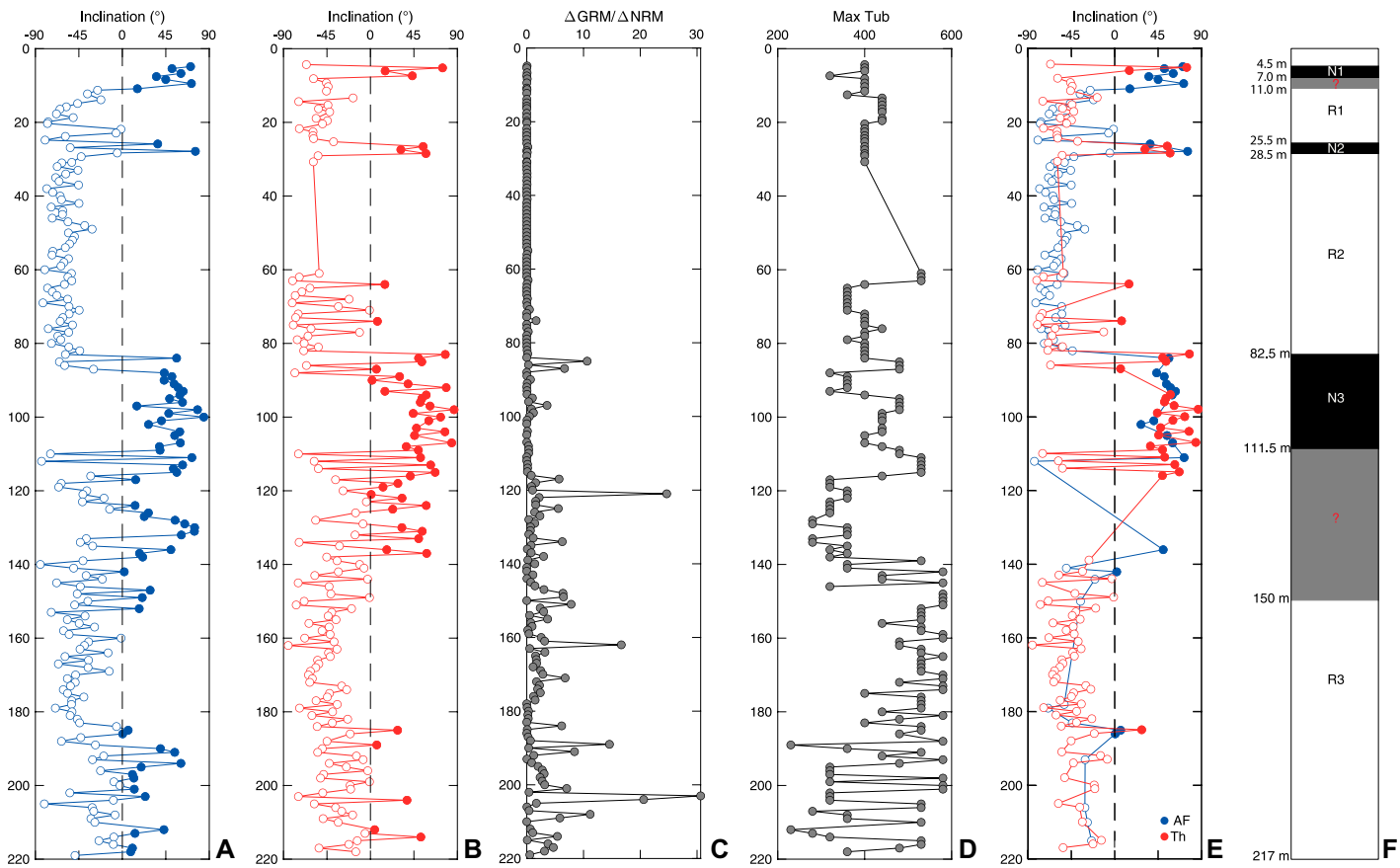

Figure 7. Stratigraphic trends of selected paleomagnetic and rock magnetic parameters: characteristic remanent magnetization (ChRM) inclination values determined for specimens subjected to alternating field (AF) demagnetization (A) and to thermal demagnetization (B); ΔGRM/ΔNRM values determined from AF demagnetization (C); maximum unblocking temperature (Tub) estimated from thermal demagnetization (D); filtered ChRM inclination data for specimens with ΔGRM/ΔNRM values <0.1 and Tub ≥400 °C (E). The resulting magnetic zonation is shown in (F). GRM—gyromagnetic remanent magnetization; NRM—natural remanent magnetization.

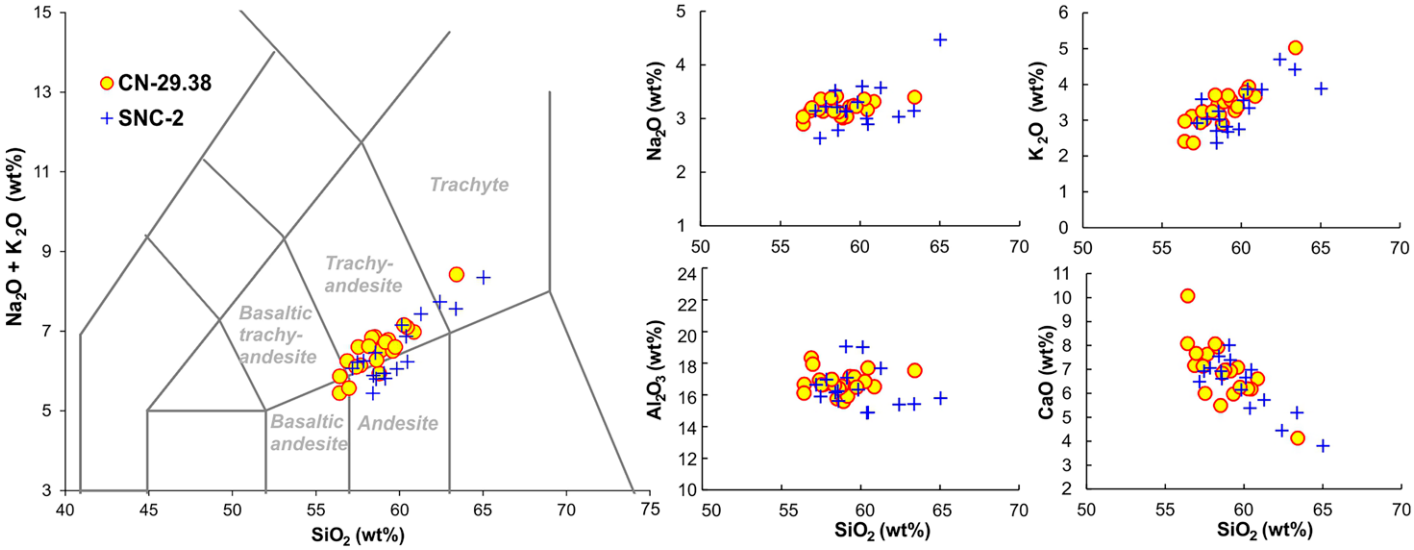

Figure 8. Total alkali vs. silica classification diagram (TAS) and representative bi-plots for the tephra SNC-2 and CN-29.38 showing a good compositional matching.

4.9. $^{40}Ar/^{39}Ar$ Geochronology of the Castelnuovo Tephra Layer (SNC-2)

The new $^{40}Ar/^{39}Ar$ ages reported herein were obtained via small-population multi-grain analyses of phenocrystic plagioclase from a fine-grained, vitric (almost aphyric) tephra layer (SNC-2), equivalent to the layer CN-29.38 in core CN-1. An age-probability density spectrum of the MCTF dating results is shown in Figure 9A. The age distribution is a quasi-symmetric, unimodal population with a weighted-mean age of 1.81 ± 0.13 Ma (1σ analytical error). As these analyses have a rather high and variable atmospheric argon component, it is instructive to analyze the argon isotopic distribution using an isotope correlation diagram ($^{36}Ar/^{40}Ar$ versus $^{39}Ar/^{40}Ar$ isochron; Fig. 9B). The age derived from the isochron analysis (1.54 ± 0.25 Ma) is about twice as imprecise as the weighted-mean age, but statistically indistinguishable from it at the 95% confidence level.

Incremental heating release spectra plots of the MCIH analyses are shown in Figure 10A. All aliquots yielded apparent-age plateaus encompassing all steps in each experiment. The "age plateau" identification algorithm used here delineates the set of contiguous steps encompassing the greatest percent of ^{39}Ar release that exhibit an acceptable MSWD (mean square of weighted deviates, with a threshold probability >95% that the observed scatter is due to analytical error alone and that geological scatter is not demonstrated). A plateau must comprise at least 50% of the total ^{39}Ar release and consist of at least three consecutive steps. The age and uncertainty assigned to the plateau are weighted means (weighted by the inverse variance of each step) and modified standard error (standard error expanded by root MSWD if MSWD is >1). The isotopic composition of each aliquot was then analyzed by the "inverse argon" isochron method to yield isochron ages (Fig. 10B), summarized in a probability density plot in Figure 10C. As before, the replicate experiments yielded a quasi-symmetrical unimodal population, with a weighted-mean age of 1.89 ± 0.18 Ma. The final age is taken as the weighted mean of the isochron ages for the MCTF and MCIH experiments, or 1.77 ± 0.15 Ma.

4.10. Cyclostratigraphy and Age Modeling

The multi-taper method spectral analysis of the whole calcimetry record shows the presence of a main spectral density peak corresponding to a frequency of a 0.034814 cycles/m (wavelength of 28.7240 m), with two secondary peaks centered at 0.021072 cycles/m (wavelength of 47.4608 m) and 0.043976 cycles/m (wavelength of 22.7396 m), respectively. Another important frequency value is related to the peak at 0.082455 cycles/m (wavelength of 12.1278 m), which is still above the 99.9% confidence limit related to the conventional AR(1) (autoregressive) modeling option we chose. The periodogram displays a series of spectral density peaks that falls below the 95% confidence limit (Fig. S12).

Multi-taper method spectral analysis provided main periodicities detected within the depth series, but it is still unclear where the dominant periodicity is mainly represented along the record. We therefore performed an evolutionary power spectral analysis, which enables an evaluation of the significance and dominance of the periodic components along the record. Defining the sliding window is a key parameter of the evolutionary power spectral analysis: too long, and higher frequencies will be over-smoothed, and possibly not detected; too short, and lower frequency can be lost (Kodama and Hinnov, 2015). Since the longest cycle of interest in the calcimetry series is ~47 m, a slightly longer window of 55 m has been adopted. The selected method to run the analysis was MATLAB's fast Fourier transform. The resulting graph reveals how the periodicity of ~12 m is dominant along the interval that spans from the top of the sediment core to almost −100 m depth, with the presence of secondary cyclicities within the first 20 m, while from −100 m depth down to the bottom the sediment core, a dominant periodicity slightly wobbles at ~28 m (Fig. 11).

Based on the results from the evolutionary spectral analysis, we split the calcimetry depth series into two different data series, the first from −2.04 m to −100 m, the second from −100 m to −220 m, with the purpose of testing if the periodicities we identified are actually the dominant ones in these two intervals. The power spectral analysis of these two data series shows, for the first interval, a main spectral density peak at a frequency value of 0.081633 cycles/m (wavelength of 12.2499 m), whereas, for the second interval, it shows a dominant frequency at 0.0399 cycles/m (wavelength of 25.0626 m; Fig. S13). It is worthwhile to note the acceptable match between values from the power spectral analysis of the whole calcimetry data series and

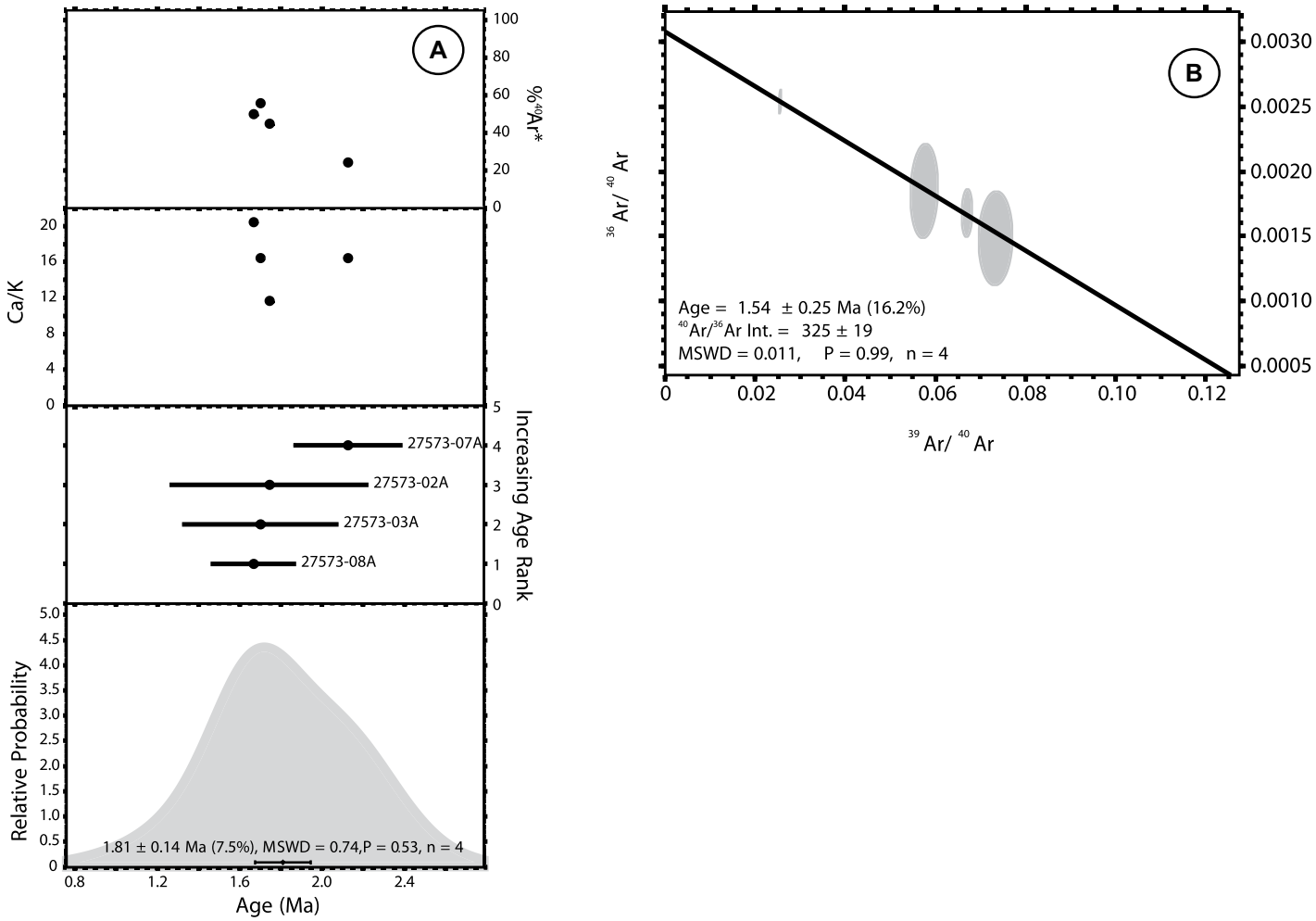

Figure 9. (A) Age-probability density spectra of multi-crystal total fusion (MCTF) analyses. The vertical scale is a relative probability measure that expresses the likelihood of a given age occurring in the sample. The weighted mean age of the analyses is shown via the 1σ error bar and the numerical annotation. (B) "Inverse" isochron plots ($^{36}Ar/^{40}Ar$ vs. $^{39}Ar/^{40}Ar$ isotope correlation diagrams) of the MCTF experiments. The age is derived from the *x*-axis intercept and is shown at 1σ. $^{40}Ar/^{39}Ar$ Int. refers to "trapped" non-radiogenic $^{40}Ar/^{36}Ar$ ratio derived from *y*-axis intercept of the isochron. MSWD—mean square of weighted deviates, a measure of the observed scatter about the fit line, compared to the expected scatter; P—probability that the observed scatter can be explained by analytical errors alone; n—number of analyses.

the ones from the power spectral analysis performed on the individual intervals.

To count the number of cycles related to each main frequency, two Gaussian band-pass filters were applied to filter the main frequency signal. Results of filtering are two filtered output series representing a real component of the calcimetry original signal related to the two specific frequency values. To merge the two filtered output series into a single filtered signal, we assumed that the main frequencies obtained in the first (−2.04 m to −100 m) and second interval (−100 m to −220 m) are attributable to the same orbital forcing (Fig. S14).

Assuming the same orbital forcing, a change in sedimentation rate could explain the wavelength increase of the dominant frequency filtered signal at ∼−100 m. As stated before, between −71.60 m and −118.80 m, clayey levels become more abundant and thicker, showing a transition from a lacustrine environment mainly dominated by carbonate authigenic silty deposits to a depositional context primarily characterized by siliciclastic clayey fine sediments, with a consequent increase in the sedimentation rate.

The merged filtered output series is composed of 13 cycles, which are characterized by different amplitudes (Fig. 12). To obtain an age model of the CN-1 sediment core, we can assign to each cycle a time interval corresponding to a particular orbital forcing. The orbital forcings we used for this step are obliquity (41 k.y.) and short eccentricity (100 k.y.). We do not consider precessional forcing as being responsible for the periodicity in the detrended calcimetry data series because the consequent sedimentation rate (0.6–1.3 mm/yr) is too high for a lacustrine environment in the intermontane basins of the central Apennines, which show typical sedimentation rates between 0.2 mm/yr and 0.7 mm/yr (e.g., Sulmona Basin; Regattieri et al., 2019). Our interpretations are illustrated in two graphs displaying the age model based on the selected orbital forcing and the change of the sedimentation rate along the series (Fig. 13).

Finally, tuning the 12–25 m cycles both to the 41 k.y. and 100 k.y. orbital cycles, two floating astronomical time scales were constructed, showing the calcimetry curve tuned to the obliquity (41 k.y.) and the eccentricity

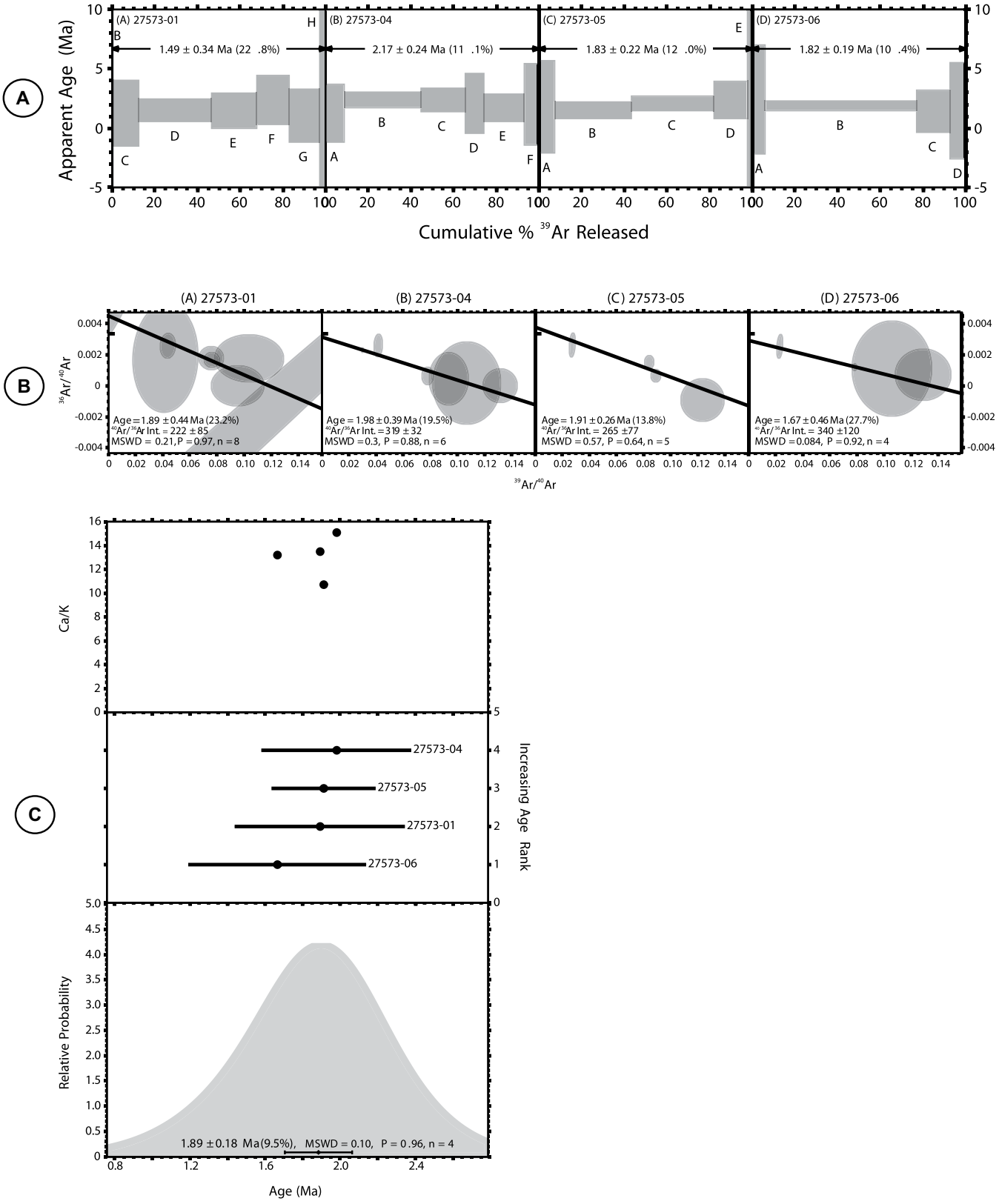

Figure 10. (A) Incremental heating release spectra of the multi-crystal incremental heating (MCIH) experiments. The weighted-mean plateau ages are shown above the release spectra. (B) Isochron plots of the individual MCIH experiments. (C) Age-probability density spectra of isochron results from the MCIH experiments. MSWD—mean square of weighted deviates; P—probability that the observed scatter can be explained by analytical errors alone; n—number of analyses.

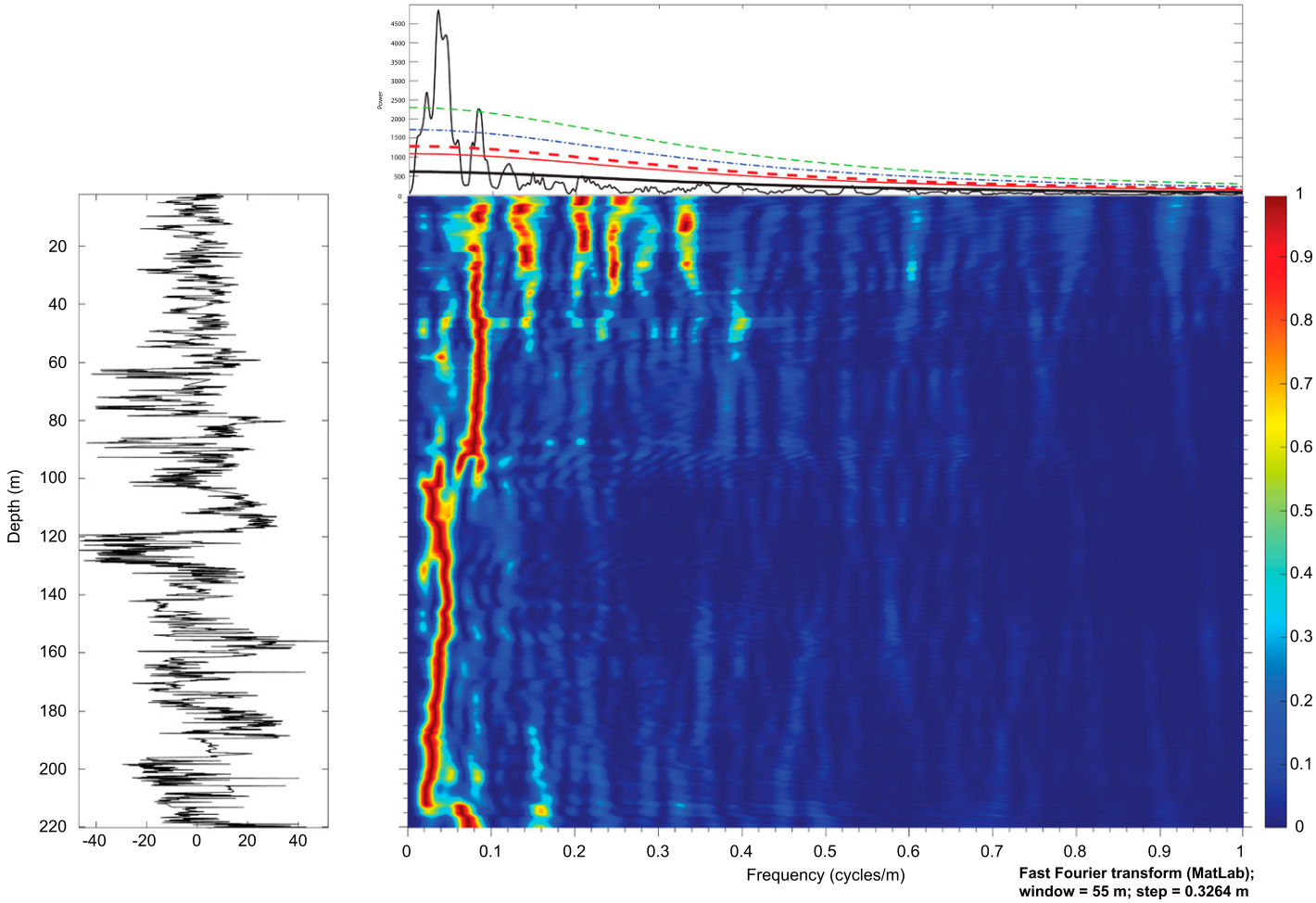

Figure 11. Evolutionary fast Fourier transform (FFT) spectrum of the calcimetry series of the Castelnuovo deep borehole after removing a LOWESS (locally weighted scatterplot smoothing) long-trend, because of evolutionary power spectral analysis. A 55-m-long running window has been used.

(100 k.y.). In the case of obliquity forcing, the CN-1 stratigraphic record represents 536.46 k.y., while in the case of eccentricity forcing, it represents 1308.43 k.y., with sedimentation rates of 0.3–0.6 mm/yr or 0.13–0.25 mm/yr, respectively (Fig. 14).

The presence, in the upper part of the CN-1 sediment core (~−30 m), of the 1.77 ± 0.15 Ma tephra layer represents a constraint for the tuning of the calcimetry curve (obliquity versus eccentricity). This point will be addressed in detail in the following section.

5. DISCUSSION

5.1. Age Model of the Castelnuovo 1 (CN-1) Deep Borehole

Combining the results from magnetostratigraphy, palynological analyses, and radiometric dating, it has been possible to achieve some constraints necessary to calibrate the spectral analysis carried out on the CN-1 sediment core and to correlate it to the geological time scale.

Palynological assemblages typical of the "warm" Piacenzian, typically dominated by *Taxodium-Glyptostrobus* in environments often characterized by extensive freshwater swamps, are present here but never exceed 9%. Steppe taxa, especially *Artemisia*, are well represented. Furthermore, the fluctuations described by the pollen curve reveal an opposition between the steppe elements and the warm/humid arboreals (Figs. 6E and 6F) reminiscent of the classical glacial/interglacial cycles that become most evident from 2.6 Ma onward.

The results from the pollen record and the $^{39}Ar/^{40}Ar$ radiometric dating of 1.77 ± 0.15 Ma obtained from the SNC-2 tephra, which corresponds to the tephra encountered at −29.38 m by the CN-1 borehole, point to an early Pleistocene age for the drilled sedimentary succession, leading us to refer the longest normal polarity interval (N3) to the Olduvai subchron. This correlation allows us to chronologically constrain the normal-reverse polarity transition at −82.50 m (top Olduvai) to 1770 ka (early Pleistocene; Channell et al., 2020).

Based on the late Piacenzian–Gelasian age of the San Nicandro Formation proposed by Spadi et al. (2016), the longest normal polarity interval (N3) detected in the CN-1 core from −82.50 m to −111.50 m could be considered as part of the Gauss Normal Chron. However, if the longest normal polarity interval (N3) were correlated with the Gauss Normal Chron (3.60–2.58 Ma), we would have expected to observe intervals dominated by *Taxodium*/*Glyptostrobus*, alongside other elements such as *Nyssa*, *Myrica*, *Engelhardia*, etc., extending from the base of the succession up to about −82 m. Moreover, we would have anticipated a more pronounced progressive reduction of these elements. Addi-

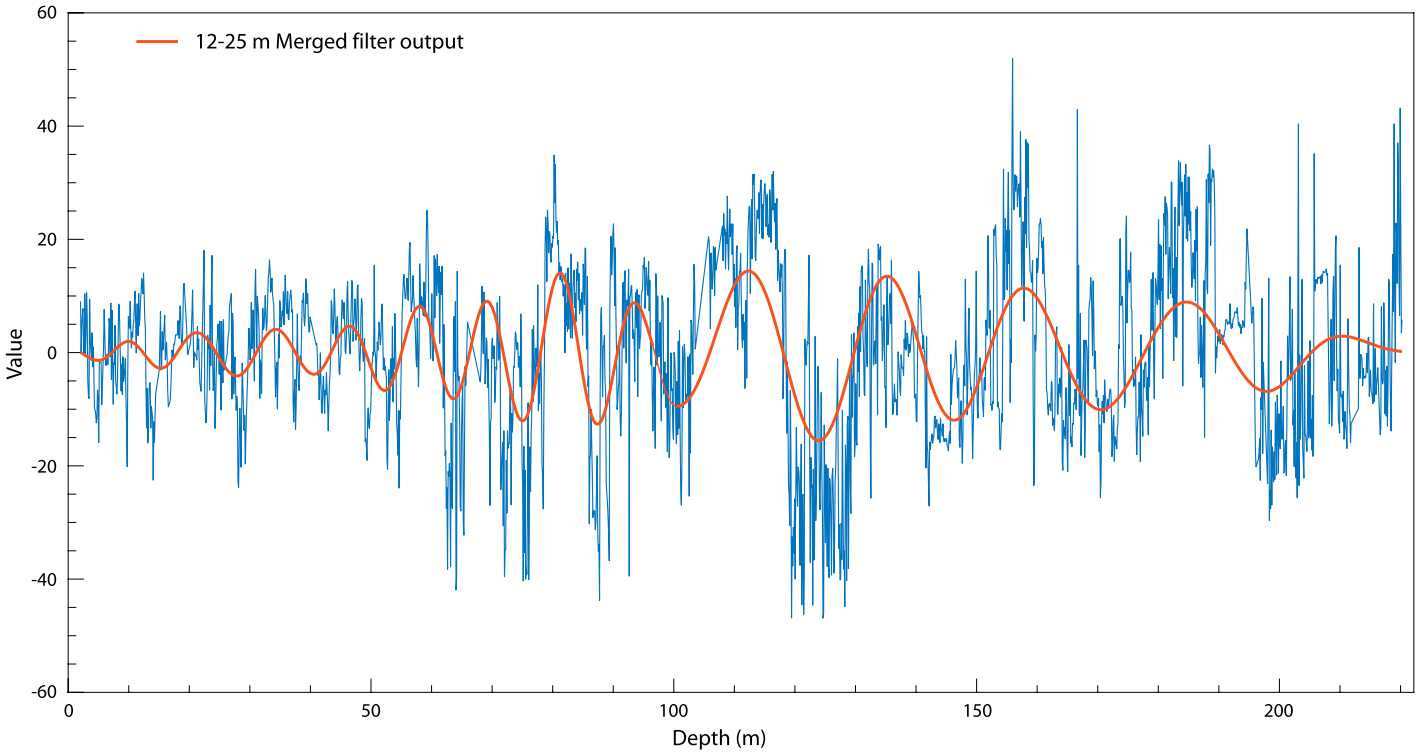

Figure 12. Detrended calcimetry data series with merged 12–25 m filter output superimposed (red line). The 13 cycles are clearly visible in both the output filter and calcimetry time series.

tionally, we should also have observed the onset of steppe phases around −80 m, which instead we observe occurring earlier, right from the base of the succession.

Given the early Pleistocene age for the CN-1 sediment core, we suggest that the 41 k.y. obliquity period is the main forcing process responsible for the cyclicity revealed by the spectral analysis of $CaCO_3$ content. According to Lisiecki and Raymo (2005), before 1.4 Ma, global climate, at least in terms of temperature and ice volume, was sensitive to obliquity modulation, and the 41-k.y. response is well recorded till 1.4 Ma. Only later, 100-k.y. orbital forcing related to short eccentricity became more dominantly influential. By assigning the obliquity periodicity to the output filtered signal of the calcimetry data series, the floating astronomical time scale provides a time span of 536.46 k.y. for the long-duration depositional processes that led to the sedimentation of the CN-1 sediment core (Fig. 15A).

Spectral analysis on the $CaCO_3$ content of the CN-1 sediment core shows the presence of 13 obliquity-modulated cycles, which display a constant wavelength from the top down to almost −90 m, while a longer wavelength has been detected for the remnant interval, down to the bottom (Fig. 15B). This change in wavelength can be explained by the variation in the depositional environment recorded by the CN-1 lithostratigraphy.

As described in section 4.1, at ~−90 m depth, the CN-1 sediment core shows a change from laminated carbonate silts (SNF), related to a distal lacustrine environment, to dark grayish siliciclastic clays (ACF) bearing centimeter carbonate clasts (dropstone), related to a lacustrine environment gradually becoming more proximal going toward the bottom of CN-1, where carbonate coarse-grained clasts point to a steep slope lacustrine margin (MNF; Fig. 16). This environmental change implies an increase in the sedimentation rate of the CN-1 sediment core starting from −90 m depth (Fig. 15B).

In terms of sequence stratigraphy, the transition between ACF/SNF encountered in the CN-1 sediment core is part of a transgressive surface (ts, in Figs. 5 and 16) responsible for the superposition of more distal and deeper lacustrine deposits (SNF) above more marginal lacustrine facies (ACF). In contrast, the abrupt SNF/VOF transition encountered at the top of the CN-1 sediment core corresponds to the maximum flooding surface (mfs, in Figs. 5 and 16), with the transition from deeper lacustrine silty deposits (SNF) to sands and conglomerates of lacustrine delta environment (VOF). This abrupt change in depositional environments was possibly due to a forced regression induced by a regional tectonic uplift that affected the L'Aquila Basin at ca. 1.5 Ma.

By comparing the petrophysical logs with the variation curves of pollen and $CaCO_3$ in the interval from 0 m to −80 m depth (Fig. 6), it is evident that the MS and Fe curves show a cyclic trend comparable to that observed for the authigenic silty carbonate deposits and that the Fe content is generally lower than the rest of the core, consistent with deposition in a deep environment with little supply of terrestrial minerals and magnetite as the main magnetic carrier of the paleomagnetic data (74 AF demagnetized paleomagnetic samples out of 100 are concentrated in this interval). Furthermore, the appearance of S peaks (~−51 m and −64–67 m) seems to occur in a longer cold climate period as revealed by the pollen curves, while the relative increase in Fe between −60 m and −80 m corresponds to a decrease in $CaCO_3$ content (Fig. 6).

In the interval from −80 m to −218 m depth, a general increase in the intensity values of MS, Fe, and S is observed. These values are consistent with an increase in the contribution of terrestrial input due to the transition from a deep lake to a marginal lacustrine depositional environment. Furthermore, the intervals between −80 m to −90 m and −190 m to −218 m are characterized by cold climate periods of longer duration, as indicated by the pollen analysis and by

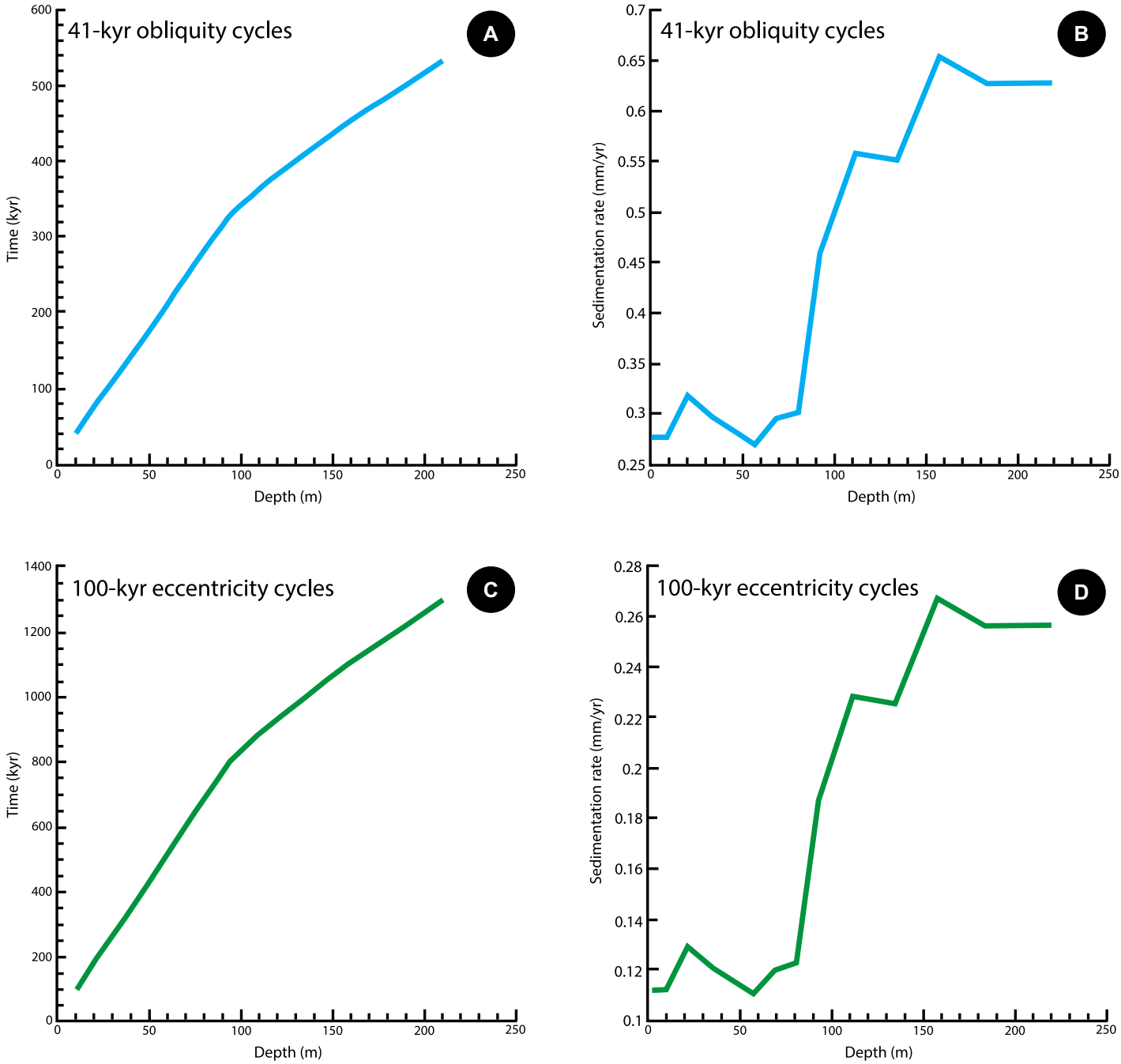

Figure 13. Age model (A) and sedimentation rate (B) obtained applying a 41 k.y. obliquity lasting for each of the 13 cycles retrieved from the filtering process. Age model (C) and sedimentation rate (D) obtained applying a 100 k.y. eccentricity lasting for each of the 13 cycles.

a lower $CaCO_3$ content. The trends in Fe and S (Figs. 6B and 6C) are probably due to an increase in terrestrial detrital input as a consequence of the decrease in plant cover for the cold climate period. In contrast, the sediments between −118 m and −150 m were deposited in warmer climate periods that persisted longer than cold ones, as demonstrated by pollen analysis, and they were characterized by a relative abundance of iron versus organic matter, which probably produced strong sulfur-reducing microbacterial activity (Kao et al., 2004; Sagnotti, 2007; Picard et al., 2018). This hypothesis is supported by the absence of valuable S content and the formation of the mineral greigite, as described in the magnetostratigraphic results.

In this regard, the general decreasing trend in $CaCO_3$ content toward the bottom of the CN-1 sediment core could be linked to the presence, and subsequent increase, of organic matter starting at a depth of −72 m (see stratigraphic log in Fig. 6). Indeed, organic carbon and $CaCO_3$ content in lake sediments are often inversely related (Dean, 1999), since large amount of organic carbon in the sediments results in pH lowering and consequent increase of $CaCO_3$ dissolution.

Starting from the magnetostratigraphic constraint described earlier, in which we use pollen data and $^{39}Ar/^{40}Ar$ dating of the SNC-2 tephra to relate the N3 normal magnetic polar-

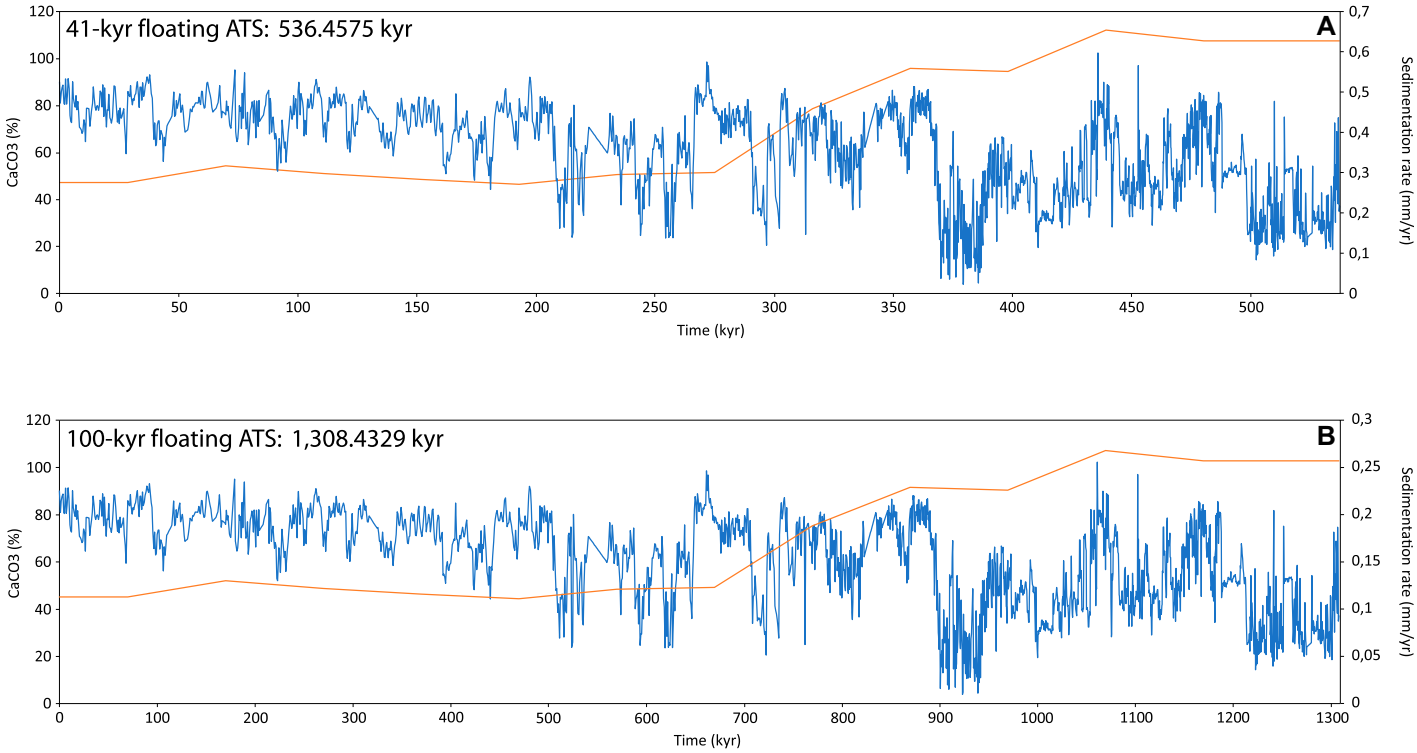

Figure 14. Floating astronomical time scale (ATS) applying a 41 k.y. obliquity orbital forcing to construct the age model (A). Floating ATS applying a 100 k.y. eccentricity orbital forcing for deriving the age model (B).

ity recovered in the CN-1 borehole (from −82.50 m to −111.50 m) to the Olduvai subchron (age of the top 1770 ka; e.g., Shackleton et al., 1990; Horng et al., 2002, 2003; Channell et al., 2002, 2016, 2020), we can correlate the 13 obliquity-modulated cycles of the CN-1 sediment core, encompassing a temporal interval of 536.46 k.y., with the La2010d astronomical solution for the obliquity (Laskar et al., 2011) and the Pliocene–Pleistocene benthic stack LR04 (Lisiecki and Raymo, 2005; Fig. 17). Following this correlation, the top Olduvai falls within MIS 63, as in other Italian land sections (Hilgen, 1991) and in several deep-sea sediment cores (Horng et al., 2002, 2003; Channell et al., 2002, 2016).

This astrochronological model results in an age of 1490.38 ka for the top of the CN-1 sediment core and an age of 2026.83 ka for its base (Fig. 17), encompassing the marine isotopic stages MIS 50 through MIS 75. Clumped-isotope–derived lake-water temperatures are used to confirm the reconstructed cyclostratigraphy and to better constrain the age model. A general trend of decreasing Δ_{47}-temperature is recorded from the lower (Δ_{47}-T of 21 ± 1.7 °C, 1SE) to the upper part of the sediment core (Δ_{47}-T of 11.5 ± 1.3 °C, 1SE), in accordance with the average trend of the Plio-Pleistocene $\delta^{18}O$ stack (Lisiecki and Raymo, 2005). Lower temperatures correspond to lower $CaCO_3$ content and to the colder MIS 64 (15.6 ± 1.7 °C), MIS 54 (11.3 ± 1.8 °C), and MIS 52 (11.5 ± 1.3 °C), while higher temperatures correspond to higher $CaCO_3$ content and to the warmer MIS 67 (21 ± 1.7 °C) and MIS 53 (15.4 ± 1.6 °C). Similar behavior was reported from Lake Trasimeno (Umbria, central Italy) during MIS 3 and 2 and the Holocene, where higher temperatures correspond to higher total inorganic carbon values and vice versa (Francke et al., 2022; Marchegiano et al., 2020, 2024a). These results could support a prevalence of carbonate precipitation during warmer periods in lacustrine systems in central Italy.

Applying this astrochronological model, the two normal magnetic polarity intervals occurring near the top of the CN-1 sediment core, from −28.5 m to −25.5 m (N2) and from −7.00 m (or −11.00 m) to −4.50 m (N1), could be ascribed, respectively, to the Gilsa excursion (1584 ka; Channell et al., 2008, 2016) and to the Gardar excursion (ca. 1460 ka; Channell et al., 2020; Fig. 18).

The N2 magnetic polarity interval (Gilsa excursion) has its top at ca. 1572 ka, while the bottom has an age of ca. 1581 ka, within the MIS 54, almost in agreement with literature data (1575–1567 ka, Channell et al., 2002; 1584 ka, Channell et al., 2016). The N1 magnetic polarity interval (Gardar excursion) has its top at ca. 1499 ka, while the bottom, due to noisy magnetic signal, could be set either at ca. 1508 ka or at ca. 1523 ka, with ages in contrast with literature data (1480–1472 ka, Channell et al., 2002; 1463 ka, Xuan et al., 2016).

The discrepancy with the presumed age of the Gardar excursion base from the literature suggests that high-resolution dating (i.e., on a millennial scale) for short-duration geomagnetic events ca. 1.5 Ma may still be subject to revision and slight adjustments.

A greater contrast between the magnetostratigraphy of CN-1 and the proposed astrochronological model is with the Olduvai base. In the literature, the onset of the Olduvai subchron has been correlated with MIS 71/72 (Horng et al., 2002, 2003), MIS 72/73 (Raymo et al., 1989), MIS 71 (Channell et al., 2003), and MIS 73 (Channell et al., 2016).

As shown in section 4.7.2 and in Figure 7, the Olduvai base (N3) is not well defined in the proposed magnetostratigraphic model because of the presence of greigite, which makes the paleomagnetic signature highly disturbed. However, below the undetermined polarity interval between −111.5 m to −150 m, a clear reverse magnetozone (R3) was detected from −150 m to −217 m (base sampling for magnetostratigraphy). It means that the Olduvai base should

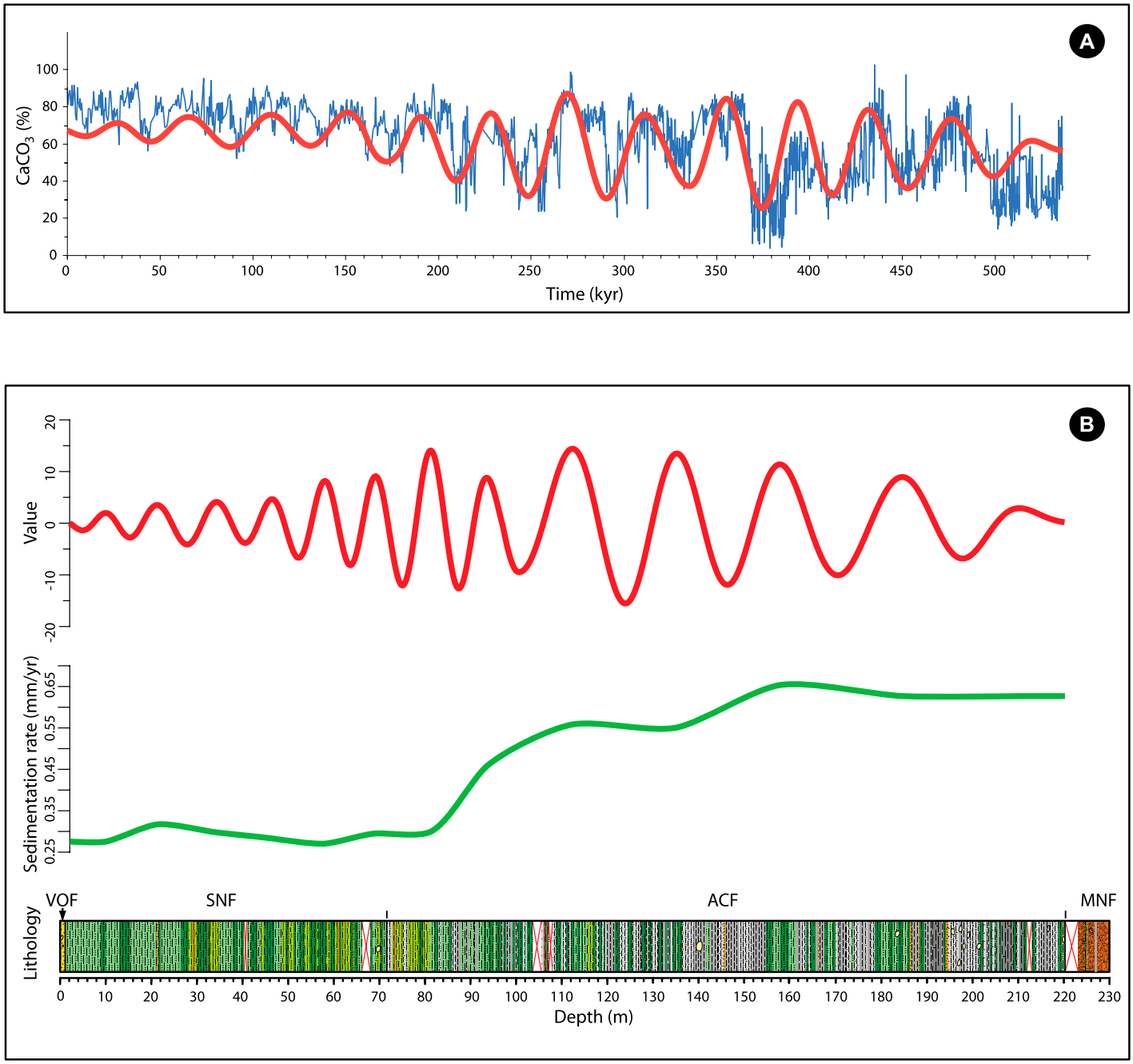

Figure 15. (A) Floating astronomical time scale (ATS) for the Castelnuovo sediment core, providing a 536.4575 k.y. duration for the sedimentary succession to take place. (B) Increasing of the sedimentation rate at ~90 m depth, where the lithology of the core gradually passes from being made up of carbonate whitish silts and sandy silts to grayish and darkish clays with sandy intercalations. The correlation between the increasing of wavelength in the filter output and the sedimentation rate is very noticeable. ACF—Argille di Castelnuovo Formation; MNF—Madonna della Neve Formation; SNF—San Nicandro Formation; VOF—Valle Orsa Formation.

be placed between −111.5 m and −150.0 m. Unfortunately, applying the astrochronological age model to these two depths, we obtain ages of ca. 1.835 Ma (MIS 67) and ca. 1.915 Ma (MIS 70), respectively, much younger than the age of the Olduvai base (1.925 Ma, MIS 71), which, in the CN-1 sediment core, corresponds to the depth of −160 m, well within the reverse magnetozone R3.

The disparity noted in positioning the base of the Olduvai subchron through cyclostratigraphy versus magnetostratigraphic zonation likely stems from the complex magnetic mineral assemblage within the core, notably in the interval below −85 m depth. In this interval, magnetite and greigite coexist as predominant magnetic carriers, in variable proportions, introducing uncertainties regarding the timing of magnetic remanence acquisition. Consequently, this complicates the interpretation of magnetostratigraphic data.

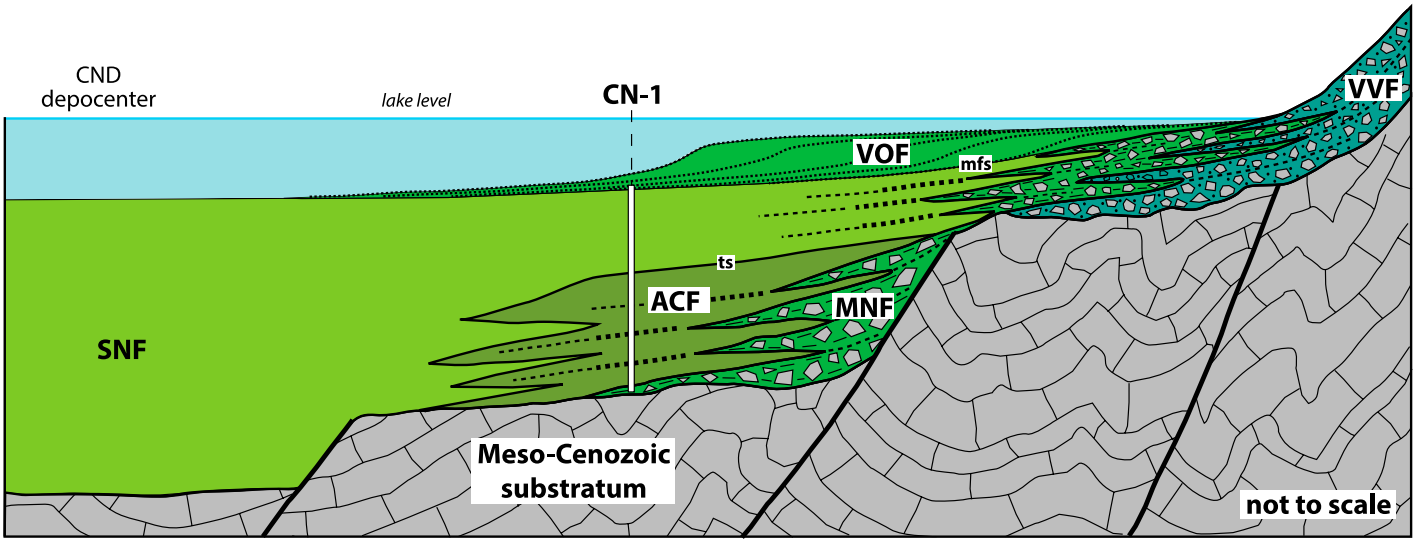

Figure 16. Facies tracts of the Plio-Pleistocene deposits of the Paganica–San Demetrio–Castelnuovo Sub-basin. ACF—laminated and overconsolidated organic-rich clays (Argille di Castelnuovo Formation); CND—Castelnuovo depocenter; CN-1—Castelnuovo 1 borehole; MNF—calcareous breccia with lacustrine whitish calcareous silty matrix (Madonna della Neve Formation); SNF—deep lacustrine whitish calcareous silty deposits (San Nicandro Formation); VVF—alluvial fan and slope deposits (Valle Valiano Formation); VOF—deltaic lacustrine conglomerates and carbonate sandstones (Valle Orsa Formation); mfs—maximum flooding surface; ts—transgressive surface. Modified from Cosentino et al. (2019).

The proposed astrochronological model points to an age of ca. 1.59 Ma for the CN-29.38 tephra layer in core CN-1, which is slightly younger than the youngest age derived from the weighted mean of the isochron ages for the MCTF and MCIH $^{40}Ar/^{39}Ar$ experiments (1.62 Ma) performed on the corresponding SNC-2 tephra. However, it is notable that the astrochronological calibration for the CN-29.38 tephra (1.59 Ma) is in agreement with the age derived from the isochron analysis of the MCTF dating results (1.54 ± 0.25 Ma; Fig. 9B).

5.2. Refining the Age for the Onset of Continental Sedimentation in the L'Aquila Intermontane Basin

Due to the lack of subsurface data for almost all the sub-basins of the L'Aquila Basin, the uncertainty on the age of the basal infill and thus for the onset of continental sedimentation in the L'Aquila intermontane basin is high. For this reason, the inferred age of Pucci et al. (2019) for the basal part of the continental deposition in the L'Aquila Basin is shown with a large error (ca. 2.3 ± 0.5 Ma), suggesting that a possible age for the creation of the L'Aquila intermontane basin could be between 2.8 Ma and 1.8 Ma.

A lack of subsurface data when attempting to reconstruct the stratigraphic architecture and thickness of the sedimentary infill of these intermontane basins is a major hindrance, resulting in reconstructions that are commonly inconsistent with newly acquired borehole data. This is the case for the reconstruction of the stratigraphic relationships within the L'Aquila area and the Paganica–San Demetrio and Barisciano-Castelnuovo sub-basins reported in recent literature (e.g., Pucci et al., 2019).

In the subsurface of the L'Aquila area, Pucci et al. (2019) reported only an 80-m-thick post-orogenic sedimentary cover. In contrast, the deepest borehole in L'Aquila downtown (S10, in Tallini et al., 2019) drilled ~400 m of fine-grained siliciclastic deposits, which are referable to alluvial plain environments with marshes and swamps (lignite levels). These characteristics enabled Tallini et al. (2019) to refer them to the Madonna della Strada Formation (lower Pleistocene pro parte).

By comparing the thickness of Madonna della Strada Formation in the subsurface of L'Aquila downtown (ca. 400 m) with that in the surrounding areas of the ASB (ca. 200 m; Tallini et al., 2012; Cosentino et al., 2017; Nocentini et al., 2017), Tallini et al. (2019) depicted an early Pleistocene depocenter in the subsurface of L'Aquila downtown. Thus, a complex buried structure, characterized by topographic highs and lows (i.e., highs and depocenters), typifies the early Pleistocene ASB.

A similar tectono-stratigraphic setting has been recognized by Civico et al. (2017) in the Middle Aterno Valley. According to these authors, the Middle Aterno Valley is characterized by three main depocenters, where the basin infill thickness varies from 200 m (Bagno depocenter) to more than 450 m (San Demetrio depocenter).

Discrepancies between subsurface schematic reconstructions and deep borehole stratigraphy can be also found for the PSC Sub-basin. In the area of Barisciano and Castelnuovo, Pucci et al. (2019) show a thickness of ca. 100 m for the early Pleistocene continental deposits resting unconformably on the Mesozoic–Cenozoic substratum.

More recently, by using the CN-1 stratigraphy, Spadi et al. (2022) showed that the observed horizontal-to-vertical spectral ratio frequency peaks are associated with an impedance contrast at −210 m depth, corresponding to the lithologic boundary between clayey silts (Argille di Castelnuovo Formation) and carbonate breccias (Madonna della Neve Formation).

By using the reconstructed complex subsurface architecture of the Middle Aterno Valley (Civico et al., 2017), the residual gravimetric anomaly map by Cesi et al. (2010), and the CN-1 stratigraphy (this work), we attempted to reconstruct the subsurface architecture of the San Demetrio–Barisciano–Castelnuovo area (Fig. 19). In addition to the San Demetrio depocenter, already described by Civico et al. (2017), our reconstruction shows a depocenter between San Nicandro and Castelnuovo (Castelnuovo depocenter; CND in Fig. 19), as revealed also by Florio et al. (2021).

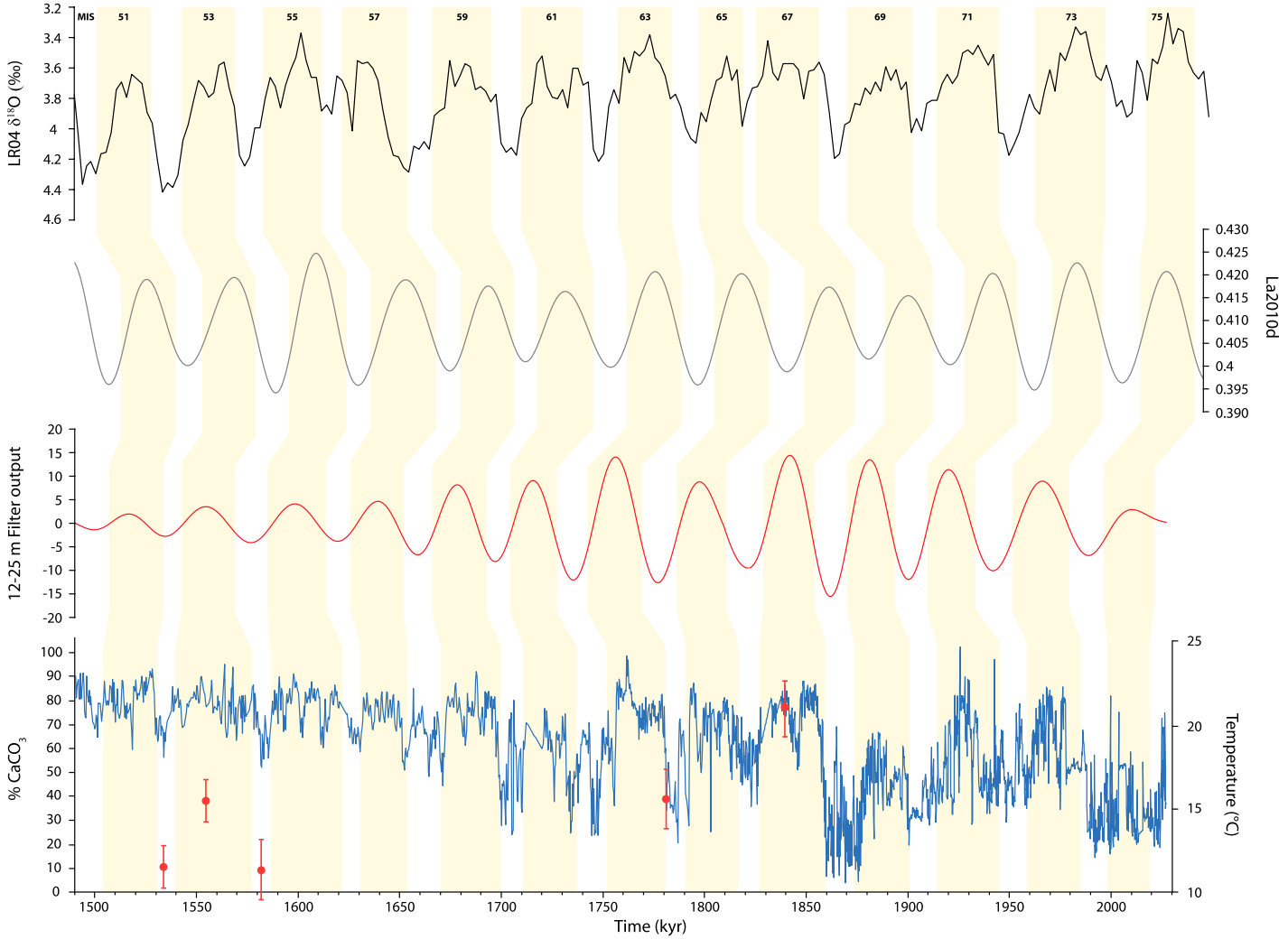

Figure 17. Diagram showing the good correlation degree among different proxies: benthic stack LR04, La2010d obliquity astronomical solution, 12–25 m merged filter output, the calcimetry signal, and the temperature derived from the clumped isotope analysis (red dots). The astrochronology of the Castelnuovo calcimetry dataset suggests a 1490.3761 ka age for the top and a 2026.8336 ka age for the bottom of the sediment core, spanning from the upper Gelasian to the lower Calabrian (lower Pleistocene).

In the San Demetrio–Castelnuovo area, Florio et al. (2021), by processing the gravity data from the Bouguer Gravity Anomaly Map of Italy (Carrozzo et al., 1986) identified two depocenters: the San Demetrio and Castelnuovo depocenters, with thicknesses of the Quaternary infill as great as 550 m and greater than 700 m, respectively.

Applying the equation $y = -14x^2 + 34x - 410$ proposed by Florio et al. (2021) for the relationship between substratum depth (y) and the gravity datum (x) at the same point, the value of −3.6 mGal performed by Cesi et al. (2010) for the Castelnuovo site would correspond to a depth of 350 m. On the contrary, considering a local thickness of 30 m for the Madonna della Neve formation, the stratigraphy of CN-1 borehole allows estimating a substratum depth at −250 m from ground level.

As a first approximation, by applying the law of direct proportionality between gravity anomaly and substratum depth, at the CN-1 borehole these two quantities lead to the definition of the formula $y = 69.4 \times x$, to define the relationship between substratum depth (y) and gravity anomaly (x) for the depocenter of which the Castelnuovo site is a part. The maximum gravity anomaly observed by Cesi et al. (2010) in this depocenter area (−8 mGal) would lead to the definition of a maximum substratum depth of ~550 m, lower than that estimated by Florio et al. (2021) for the Castelnuovo depocenter (700 m).

For this depocenter (CND in Fig. 19) we can infer <300 masl for the elevation of the Mesozoic–Cenozoic bedrock. In addition to the trend of the bedrock, the outcrop elevations of the VOF/SNF boundary, its bedding attitude, and the horizontal lines on the dipping surface of this boundary are shown in Figure 19.

Combining the minimum elevation of the Castelnuovo depocenter (<300 masl) with the elevation of the horizontal line on the dipping surface of the VOF/SNF boundary in the depocentral area (H810; Fig. 19), we can infer more than 510 m of thickness for the SNF, which represents the first depositional unit resting above the Meso-Cenozoic bedrock in the depocentral areas of the PSC Sub-basin (Cosentino et al., 2019; Fig. 16). A similar thickness (450 m) for the SNF can be suggested for the San Demetrio depocenter, which shows the Mesozoic–Cenozoic bedrock at ca. 150 masl and the elevation of the horizontal line on the dipping surface of

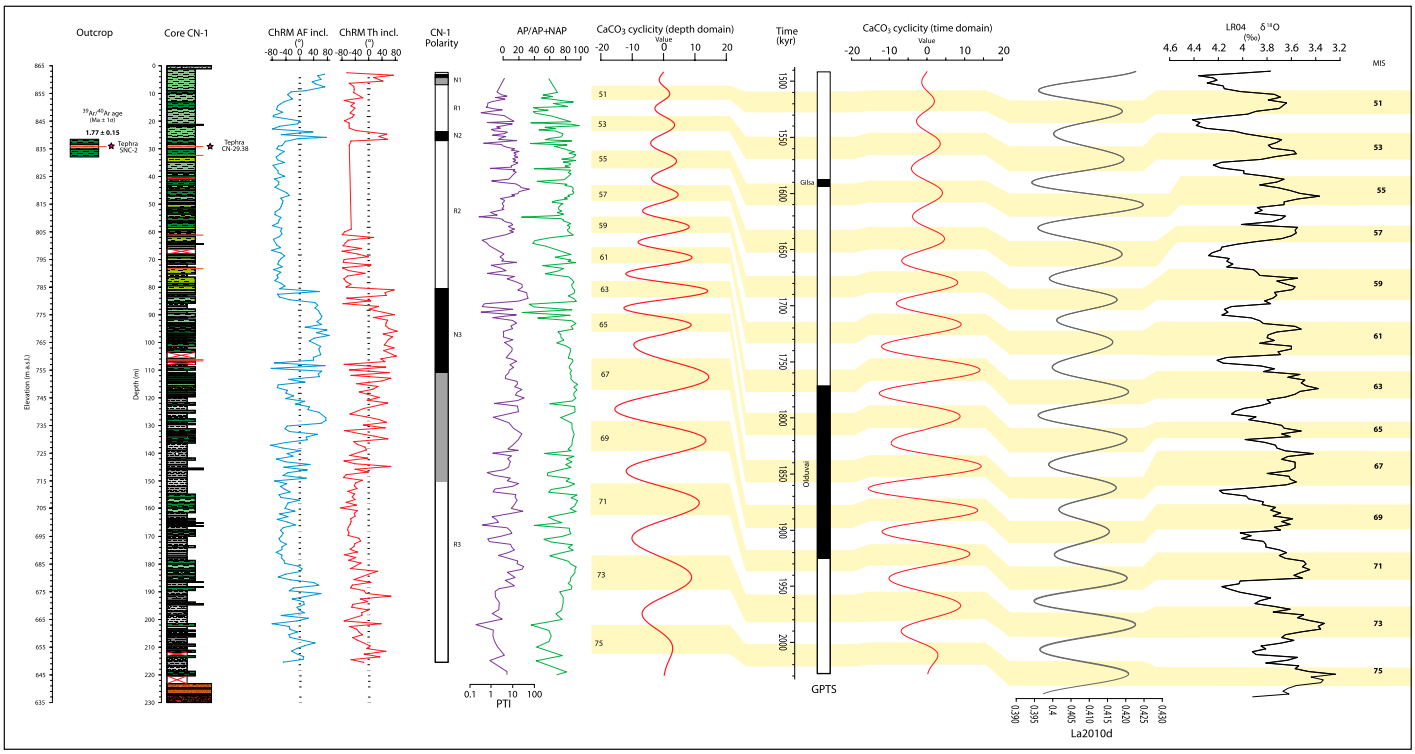

Figure 18. Correlation panel of the main proxies used to define the age model of the CN-1 sediment core. ChRM—characteristic remanent magnetization; AF—alternating field demagnetization; Th—thermal demagnetization; AP—arboreal plants; NAP—non-arboreal plants; PTI—pollen temperature index; GPTS—geomagnetic polarity time scale; La2010d—astronomical solution for the obliquity (Laskar et al., 2011); LR04—Pliocene–Pleistocene benthic stack (Lisieck and Raymo, 2005); MIS—marine isotopic stage.

the VOF/SNF boundary at 600 masl (H600; Fig. 19).

For the deep lacustrine whitish calcareous silty deposits of the SNF drilled by the CN-1 borehole down to a depth of −80 m, the proposed age model suggests a sedimentation rate of 0.3 mm/yr. Higher sedimentation rates (0.5–0.6 mm/yr) characterize the lacustrine marginal facies drilled from −120 m to −230 m (mainly ACF; Fig. 15B).

Considering that the more silty-sandy facies of ACF and the more marginal lacustrine facies (Madonna della Neve Formation) strictly characterize the marginal areas of the ancient lacustrine basin (e.g., Nocentini et al., 2018; Cosentino et al., 2019), the areas far from its margins, and even more the depocentral areas, hosted the sedimentation of fine-grained deep lacustrine deposits (white calcareous silts, SNF; Fig. 16). Therefore, we can attribute sedimentation rates of 0.3 mm/yr to the depocentral areas of the ancient lacustrine basin. Assuming a constant sedimentation rate through time, the 450 m of deep lacustrine sediment (SNF) of the San Demetrio depocenter would have been deposited in 1.5 m.y. and, considering the age of ca. 1.5 Ma for the VOF/SNF boundary from the age model of the CN-1 stratigraphy, the onset of the lacustrine sedimentation in the PSC Sub-basin would have started at ca. 3 Ma. Slightly older would be the age of onset of lacustrine sedimentation in the PSC Sub-basin if we consider the greater depth of the Castelnuovo depocenter, with a thickness of 510 m of lacustrine deposit (ca. 3.2 Ma).

These ages for the formation of the tectonically controlled L'Aquila intermontane basin are in agreement with the low-temperature exhumation ages of the carbonate bedrocks recently obtained for the Monte Marine fault zone, in the L'Aquila Basin, by dolomite luminescence thermochronometry (Zhang et al., 2025), as well as with the Pliocene–Pleistocene kinematic evolution of the central Apennines (e.g., Cosentino et al., 2010, 2017).

In this tectonic framework, the L'Aquila intermontane basin developed in a post-orogenic setting, within the late Pliocene–earliest Pleistocene syn-rift area of the central-northern Apennines, which includes all the Plio-Quaternary intermontane basins from the Tiberino Basin to the Sulmona Basin (Cosentino et al., 2017).

6. CONCLUSIONS

We applied an integrated multiple-dating approach, including $^{40}Ar/^{39}Ar$ dating, magnetostratigraphy, multiproxy paleoclimatic data, and astrocyclostratigraphy, to a long sediment core (Castelnuovo 1 borehole; CN-1) recovered from the L'Aquila Basin lacustrine succession to reduce the existing uncertainties about the age of the basin and the onset of the current extensional tectonic and seismic regime that is affecting the central Apennines.

Combining the results from magnetostratigraphy, palynological analyses, and radiometric dating, it has been possible to obtain constraints necessary to correlate the CN-1 borehole with the geological time scale. Results from the pollen record and $^{40}Ar/^{39}Ar$ radiometric dating obtained from the SNC-2 tephra (1.77 ± 0.15 Ma) indicate that the longest polarity interval of the CN-1 sediment core (N3) can be referred to the Olduvai subchron. In addition, spectral analysis on the calcimetry data series of the CN-1 sediment core shows the presence of 13 obliquity-modulated cycles, which correspond to a time span of ~536 k.y.

The well-defined top of the Olduvai subchron allow us to correlate the 13 obliquity-modulated cycles with the La2010d astronomical solution for the obliquity (Laskar et al., 2011) and the Pliocene–Pleistocene benthic stack LR04 (Lisiecki and Raymo, 2005), resulting in an

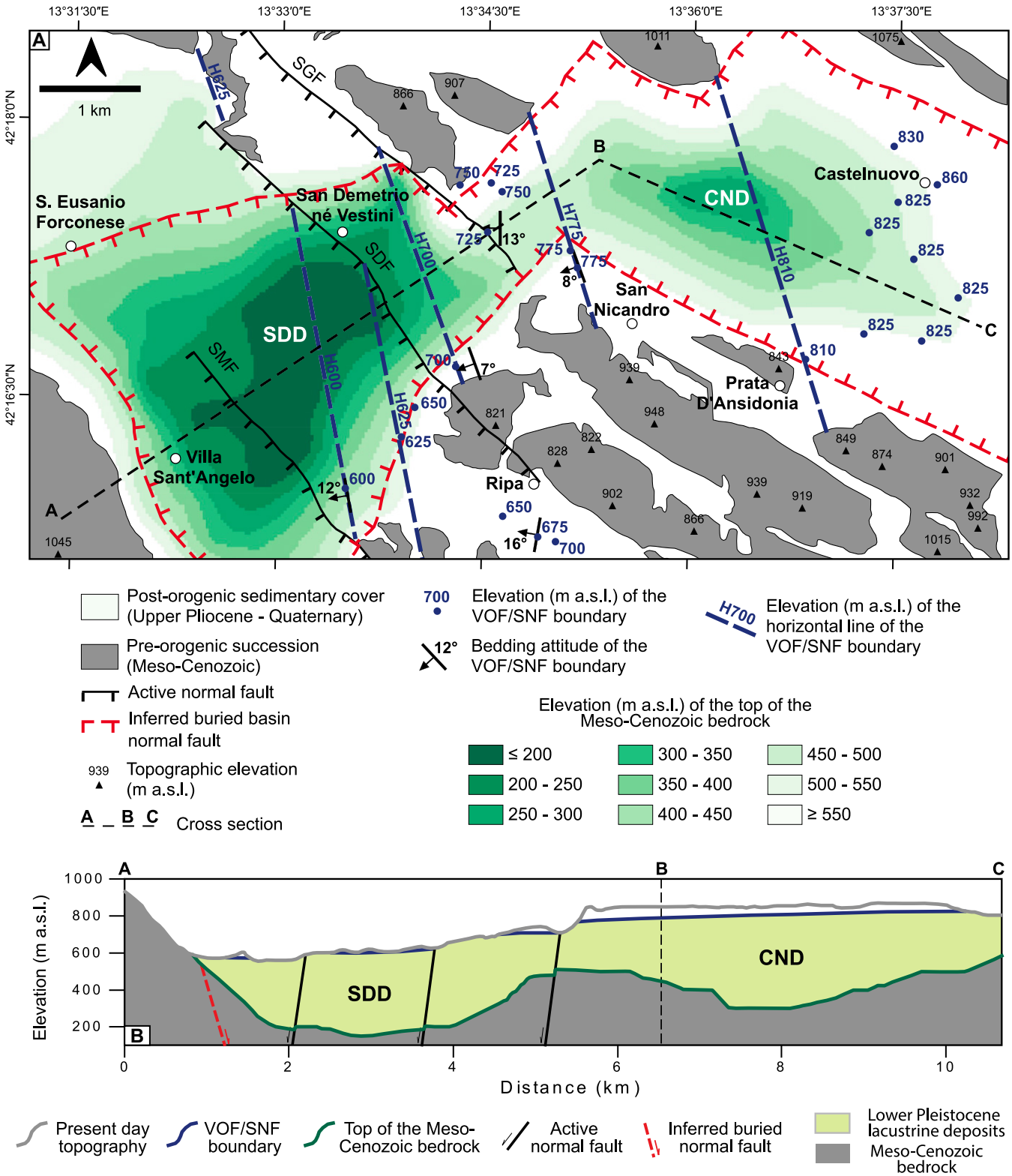

Figure 19. (A) Reconstruction of the complex subsurface geology of a part of the Paganica–San Demetrio–Castelnuovo (PSC) Subbasin, between S. Eusanio Forconese, to the west, and Castelnuovo, to the east. Data from Civico et al. (2017), Cesi et al. (2010), and the CN-1 stratigraphy (this work). CND—Castelnuovo depocenter; SDD—San Demetrio depocenter; SDF—San Demetrio fault; SGF—San Giovanni fault; SMF—San Mauro fault. (B) Cross section showing the subsurface geological model for the PSC Subbasin. The thickness of the lacustrine deposits of the different depocenters can be calculated by subtracting the elevation of the Mesozoic–Cenozoic bedrock from the elevation of the Valle Orsa Formation/San Nicandro Formation (VOF/SNF) boundary.

age of ca. 1490 ka for the top of the CN-1 sediment core and an age of ca. 2027 ka for its base. Consequently, the sediment core encompasses the marine isotopic stages between MIS 50 and MIS 75.

Ostracod analyses show the occurrence of *Caspiocypris nicandroi* and *Cypria* cf. *C. bikeratia* already from the lowermost portion of the core (−211 m depth), pointing to the presence of a well-developed lacustrine environment in the PSC Sub-basin at 2 Ma.

This lacustrine environment recorded warm-to-cold climate changes evidenced by variations in both the pollen temperature index and in clumped isotopes measurements. In particular, the lacustrine environment recorded warm-to-cold temperatures of 15.4 ± 1.6 °C (MIS 53) and 11.5 ± 1.3 °C (MIS 52), lower than the temperatures from the lower part of the sediment core, which show warm-to-cold temperatures of 21 ± 1.7 °C (MIS 67) and 15.6 ± 1.7 °C (MIS 64).

As in other parts of the L'Aquila intermontane basin, the PSC Sub-basin shows a complex subsurface architecture with highs and depocenters. In both the main depocenters of the PSC Sub-basin (San Nicandro and Castelnuovo depocenters), we can infer from 450 m up to 510 m of thickness for the deep lacustrine deposits of the SNF, which represents the first continental unit deposited above the marine Mesozoic–Cenozoic bedrock in the depocentral area of the PSC Sub-basin.

The age model performed in this work for the CN-1 sediment core suggests a sedimentation rate of 0.3 mm/yr for the fine-grained deep lacustrine deposits of the SNF, which we extrapolate to estimate the onset of the continental sedimentation in the PSC Sub-basin and thus, by extension, of the onset of the current extensional tectonic and seismic regime at ca. 3.2–3.0 Ma.

This conclusion supports the idea that L'Aquila intermontane basin developed in a post-orogenic setting, within the late Pliocene–Pleistocene extensional area of the central-northern Apennines of Italy (Cosentino et al., 2017), which includes the intermontane basins from the Tiberino Basin (to the NW) to the Sulmona Basin (to the SE). This post-orogenic extensional domain, which is still active, represents an archive of ∼3 m.y. of continued crustal extension and one of the most seismically active sectors of the central Mediterranean region.

ACKNOWLEDGMENTS

The deep borehole CN-1 was funded by the following institutions, which are warmly thanked for their support: Dipartimento di Ingegneria, Edile-Architettura e Ambientale, Università dell'Aquila (Italy); Dipartimento di Scienze, Università di Roma Tre (Italy); Istituto di Geologia Ambientale e Geoingegneria, CNR (Italy); Ufficio Speciale per la Ricostruzione dei Comuni Cratere (USRC), Fossa (L'Aquila, Italy). Giorgio Pipponzi and USRC are thanked for the local logistical assistance. The grant to the Department of Sciences of Roma Tre University (MIUR—Italy Department of Excellence, article 1, paragraph 314–337, law 232/2016) is gratefully acknowledged. P. Claeys thanks the Research Foundation Flanders (FWO) for instrument funding and the VUB Strategic Research program. The authors especially thank Taylor Schildgen, Alex Whittaker, and two anonymous reviewers whose insightful comments have greatly improved our manuscript. This work is dedicated to our dear friend and colleague Giorgio Pipponzi, who left us too soon.

REFERENCES CITED

Abbazzi, L., Albianelli, A., Ambrosetti, P., Argenti, P., Basilici, G., Bertini, A., Gentili, S., Masini, F., Napoleone, G., and Pontini, M.R., 1997, Paleontological and sedimentological record in Pliocene distal alluvial fan deposits at Cava Toppetti (Todi, central Italy): Bollettino della Società Paleontologica Italiana, v. 36, p. 5–22.

Affek, H.P., Bar-Matthews, M., Ayalon, A., Matthews, A., and Eiler, J.M., 2008, Glacial/interglacial temperature variations in Soreq cave speleothems as recorded by 'clumped isotope' thermometry: Geochimica et Cosmochimica Acta, v. 72, p. 5351–5360, https://doi.org/10.1016/j.gca.2008.06.031.

Agostini, S., Palombo, M.R., Rossi, M.A., Di Canzio, E., and Tallini, M., 2012, *Mammuthus meridionalis* (Nesti, 1825) from Campo di Pile (L'Aquila, Abruzzo, central Italy): Quaternary International, v. 276–277, p. 42–52, https://doi.org/10.1016/j.quaint.2012.05.013.

Agterhuis, T., Ziegler, M., de Winter, N.J., and Lourens, L.J., 2022, Warm deep-sea temperatures across Eocene Thermal Maximum 2 from clumped isotope thermometry: Communications Earth & Environment, v. 3, 39, https://doi.org/10.1038/s43247-022-00350-8.

Amato, A., Chiarabba, C., and Selvaggi, G., 1997, Crustal and deep seismicity in Italy (30 years after): Annali di Geofisica, v. 40, p. 981–993, https://doi.org/10.4401/ag-3839.

Arriga, G., Marchegiano, M., Peral, M., Hu, H.-M., Cosentino, D., Shen, C.-C., Dalton, H., Brilli, M., Aldega, L., Claeys, P., and Rossetti, F., 2024, Long-term tectonostratigraphic evolution of a propagating rift system, L'Aquila Intermontane Basin (central Apennines): Tectonics, v. 43, https://doi.org/10.1029/2024TC008548.

Bagh, S., Chiaraluce, L., De Gori, P., Moretti, M., Govoni, A., Chiarabba, C., Di Bartolomeo, P., and Romanelli, M., 2007, Background seismicity in the Central Apennines of Italy: The Abruzzo region case study: Tectonophysics, v. 444, p. 80–92, https://doi.org/10.1016/j.tecto.2007.08.009.

Barchi, M., Brozzetti, E., and Lavecchia, G., 1991, Analisi strutturale e geometrica dei bacini della media Valle del Tevere e della Valle Umbra: Bollettino della Società Geologica Italiana, v. 110, p. 65–76.

Basilici, G., 1997, Sedimentary facies in an extensional and deep-lacustrine depositional system: The Pliocene Tiberino Basin, central Italy: Sedimentary Geology, v. 109, p. 73–94, https://doi.org/10.1016/S0037-0738(96)00056-5.

Bennett, M.R., Doyle, P., and Mather, A.E., 1996, Dropstones: Their origin and significance: Palaeogeography, Palaeoclimatology, Palaeoecology, v. 121, p. 331–339, https://doi.org/10.1016/0031-0182(95)00071-2.

Bernasconi, S.M., et al., 2018, Reducing uncertainties in carbonate clumped isotope analysis through consistent carbonate-based standardization: Geochemistry, Geophysics, Geosystems, v. 19, p. 2895–2914, https://doi.org/10.1029/2017GC007385.

Bernasconi, S.M., et al., 2021, InterCarb: A community effort to improve interlaboratory standardization of the carbonate clumped isotope thermometer using carbonate standards: Geochemistry, Geophysics, Geosystems, v. 22, https://doi.org/10.1029/2020GC009588.

Bertini, A., 2010, Pliocene to Pleistocene palynoflora and vegetation in Italy: State of the art: Quaternary International, v. 225, p. 5–24, https://doi.org/10.1016/j.quaint.2010.04.025.

Bertini, A., 2013, Climate and vegetation in the Upper Valdarno Basin (central Italy) as a response to Northern Hemisphere insolation forcing and regional tectonics in the late Pliocene-early Pleistocene: Italian Journal of Geosciences, v. 132, p. 137–148, https://doi.org/10.3301/IJG.2012.18.

Bertini, A., and Combourieu-Nebout, N., 2023, Piacenzian to late Pleistocene flora and vegetation in Italy: A moving sketch: Piacenzian to Pleistocene flora and vegetation in Italy: Alpine and Mediterranean Quaternary, v. 36, p. 91–119, https://doi.org/10.26382/AMQ.2023.05.

Bertini, A., Toti, F., Marino, M., and Ciaranfi, N., 2015, Vegetation and climate across the Early-Middle Pleistocene transition at Montalbano Jonico, southern Italy: Quaternary International, v. 383, p. 74–88, https://doi.org/10.1016/j.quaint.2015.01.003.

Bertini, T., and Bosi, C., 1993, La tettonica quaternaria della conca di Fossa (L'Aquila): Il Quaternario, v. 6, p. 293–314.

Blumetti, A.M., Guerrieri, L., and Vittori, E., 2013, The primary role of the Paganica-San Demetrio fault system in the seismic landscape of the Middle Aterno Valley basin (Central Apennines): Quaternary International, v. 288, p. 183–194, https://doi.org/10.1016/j.quaint.2012.04.040.

Bosi, C., 1989, Tentativo di correlazione fra le successioni Plio-Pleistoceniche, *in* Elementi di Tettonica Plio-cenico-Quaternaria ed Indizi di Sismicità Olocenica nell'Appennino Laziale-Abruzzese: Rome, Italy, Società Geologica Italiana, p. 97–104.

Bosi, C., and Bertini, T., 1970, Geologia della media valle dell'Aterno: Memorie della Societa Geologica Italiana, v. 9, p. 719–777.

Bosi, C., Galadini, F., Giaccio, B., Messina, P., and Sposato, A., 2003, Plio-Quaternary continental deposits in the Latium- Abruzzi Apennines: The correlation of geological events across different intermontane basins: Il Quaternario, v. 16, p. 55–76.

Brand, W.A., Assonov, S.S., and Coplen, T.B., 2010, Correction for the ^{17}O interference in $\delta(^{13}C)$ measurements when analyzing CO_2 with stable isotope mass spectrometry (IUPAC Technical Report): Pure and Applied Chemistry, v. 82, p. 1719–1733, https://doi.org/10.1351/PAC-REP-09-01-05.

Brozzetti, F., et al., 2019, High-resolution field mapping and analysis of the August–October 2016 coseismic surface faulting (central Italy earthquakes): Slip distribution, parameterization, and comparison with global earthquakes: Tectonics, v. 38, p. 417–439, https://doi.org/10.1029/2018TC005305.

Bruno, P.P.G., Villani, F., and Improta, L., 2022, High-resolution seismic imaging of fault-controlled basins: A case study from the 2009 Mw 6.1 central Italy earthquake: Tectonics, v. 41, https://doi.org/10.1029/2022TC007207.

Carminati, E., and Doglioni, C., 2012, Alps vs. Apennines: The paradigm of a tectonically asymmetric Earth: Earth-Science Reviews, v. 112, p. 67–96, https://doi.org/10.1016/j.earscirev.2012.02.004.

Carrozzo, M.T., Luzio, D., Margiotta, C., and Quarta, T., 1986, Gravity anomaly map of Italy: Consiglio Nazionale delle Ricerche (CNR), Progetto Finalizzato Geodinamica (Geodynamics, Final Project), sub-project Modello Strutturale–Tridimensionale (Three-Dimensional Structural Model) [in Italian].

Cavinato, G.P., and DeCelles, P.G., 1999, Extensional basins in the tectonically bimodal Central Apennines fold-thrust belt, Italy: Response to corner flow above a subducting slab in retrograde motion: Geology, v. 27, p. 955–958, https://doi.org/10.1130/0091-7613(1999)027<0955:EBITTB>2.3.CO;2.

Centamore, E., and Dramis, F., 2010, Note Illustrative della Carta Geologica d'Italia alla scala 1:50,000, Foglio 358—Pescorocchiano: Istituto Superiore per la Protezione e la Ricerca Ambientale (ISPRA)–Servizio Geologico d'Italia, Ente Realizzatore Regione Lazio, Rome, Italy, 147 p., http://www.isprambiente.gov.it/Media/carg/note_illustrative/358_Pescorocchiano.pdf.

Centamore, E., Crescenti, U., and Dramis, F., 2006, Note illustrative della Carta Geologica d'Italia alla scala

1:50.000, Foglio 359—L'Aquila: APAT—Dipartimento Difesa del Suolo-Servizio Geologico d'Italia, Ente realizzatore Regione Abruzzo, 128 p., http://www.isprambiente.gov.it/Media/carg/note_illustrative/359_LAquila.pdf.

Cesi, C., Di Filippo, M., Di Nezza, M., and Ferri, M., 2010, Caratteri gravimetrici della media Valle del Fiume Aterno, *in* Microzonazione sismica per la ricostruzione dell'area Aquilana, vol. 3: Gruppo di Lavoro MS–AQ Ed., Regione Abruzzo–Dipartimento della Protezione Civile, L'Aquila.

Channell, J.E.T., Mazaud, A., Sullivan, P., Turner, S., and Raymo, M.E., 2002, Geomagnetic excursions and paleointensities in the 0.9–2.15 Ma interval of the Matuyama chron at ODP Sites 983 and 984 (Iceland Basin): Journal of Geophysical Research: Solid Earth, v. 107, v. B6, https://doi.org/10.1029/2001JB000491.

Channell, J.E.T., Labs, J., and Raymo, M.E., 2003, The Reunion subchronozone at ODP site 981 (Feni drift, North Atlantic): Earth and Planetary Science Letters, v. 215, p. 1–12, https://doi.org/10.1016/S0012-821X(03)00435-7.

Channell, J.E.T., Hodell, D.A., Xuan, C., Mazaud, A., and Stoner, J.S., 2008, Age calibrated relative paleointensity for the last 1.5 Myr at IODP Site U1308 (North Atlantic): Earth and Planetary Science Letters, v. 274, p. 59–71, https://doi.org/10.1016/j.epsl.2008.07.005.

Channell, J.E.T., Hodell, D.A., and Curtis, J.H., 2016, Relative paleointensity (RPI) and oxygen isotope stratigraphy at IODP site U1308: North Atlantic RPI stack for 1.2–2.2 Ma (NARPI-2200) and age of the Olduvai subchron: Quaternary Science Reviews, v. 131, p. 1–19, https://doi.org/10.1016/j.quascirev.2015.10.011.

Channell, J.E.T., Singer, B.S., and Jicha, B.R., 2020, Timing of Quaternary geomagnetic reversals and excursions in volcanic and sedimentary archives: Quaternary Science Reviews, v. 228, https://doi.org/10.1016/j.quascirev.2019.106114.

Cinti, F.R., et al., 2019, 22-kyr-long record of surface faulting along the source of the 30 October 2016 earthquake (Central Apennines, Italy), from integrated paleoseismic data sets: Journal of Geophysical Research: Solid Earth, v. 124, p. 9021–9048, https://doi.org/10.1029/2019JB017757.

Cipollari, P., Cosentino, D., and Gliozzi, E., 1999, Extension- and compression-related basins in central Italy during the Messinian Lago-Mare event: Tectonophysics, v. 315, p. 163–185, https://doi.org/10.1016/S0040-1951(99)00287-5.

Civico, R., Sapia, V., Di Giulio, G., Villani, F., Pucci, S., Baccheschi, P., Amoroso, S., Cantore, L., Di Naccio, D., Hailemikael, S., Smedile, A., Vassallo, M., Marchetti, M., and Pantosti, D., 2017, Geometry and evolution of a fault-controlled Quaternary basin by means of TDEM and single-station ambient vibration surveys: The example of the 2009 L'Aquila earthquake area, central Italy: Journal of Geophysical Research: Solid Earth, v. 122, https://doi.org/10.1002/2016JB013451.

Cosentino, D., Cipollari, P., Marsili, P., and Scrocca, D., 2010, Geology of the central Apennines: A regional review, *in* Beltrando, M., Peccerillo, A., Mattei, M., Conticelli, S., and Doglioni, C., eds., The Geology of Italy: Journal of the Virtual Explorer, v. 36, https://doi.org/10.3809/jvirtex.2010.00223.

Cosentino, D., Asti, R., Nocentini, M., Gliozzi, E., Kotsakis, T., Mattei, M., Esu, D., Spadi, M., Tallini, M., Cifelli, F., Pennacchioni, M., Cavuoto, G., and Di Fiore, V., 2017, New insights into the onset and evolution of the central Apennine extensional intermontane basins based on the tectonically active L'Aquila Basin (central Italy): Geological Society of America Bulletin, v. 129, p. 1314–1336, https://doi.org/10.1130/B31679.1.

Cosentino, D., Giaccio, B., Gliozzi, E., Nocentini, M., Pipponzi, G., Spadi, M., and Tallini, M., 2019, Lacustrine deposits of the late Piacenzian-Gelasian L'Aquila intermontane basin (central Italy), *in* Vigliotti, M., Tropeano, M., Pascucci, V., Ruberti, D., and Sabato, L., eds., Field Trips Guide Book: International Association of Sedimentologists 34th IAS Meeting of Sedimentology, Rome, Italy, 10–13 September 2019, Field Trip A5, p. 93–111.

Daëron, M., 2021, Full propagation of analytical uncertainties in Δ_{47} measurements: Geochemistry, Geophysics, Geosystems, v. 22, https://doi.org/10.1029/2020GC009592.

Daëron, M., Blamart, D., Peral, M., and Affek, H.P., 2016, Absolute isotopic abundance ratios and the accuracy of Δ_{47} measurements: Chemical Geology, v. 442, p. 83–96, https://doi.org/10.1016/j.chemgeo.2016.08.014.

Dean, W.E., 1999, The carbon cycle and biogeochemical dynamics in lake sediments: Journal of Paleolimnology, v. 21, p. 375–393, https://doi.org/10.1023/A:1008066118210.

De Vleeschouwer, D., Peral, M., Marchegiano, M., Füllberg, A., Meinicke, N., Pälike, H., Auer, G., Petrick, B., Snoeck, C., Goderis, S., and Claeys, P., 2022, Plio-Pleistocene Perth Basin water temperatures and Leeuwin Current dynamics (Indian Ocean) derived from oxygen and clumped isotope paleothermometry: Climate of the Past Discussions, v. 18, p. 1–40, https://doi.org/10.5194/cp-2021-151.

Dewey, J.F., 1988, Extensional collapse of orogens: Tectonics, v. 7, p. 1123–1139, https://doi.org/10.1029/TC007i006p01123.

Dubois, M.K., Goldstein, R.H., and Hasiotis, S.T., 2012, Climate-controlled aggradation and cyclicity of continental loessic siliciclastic sediments is Asselian-Sakmarian cyclothems, Permian, Hugoton embayment, USA: Sedimentology, v. 59, p. 1782–1816, https://doi.org/10.1111/j.1365-3091.2012.01326.x.

Eiler, J.M., 2007, "Clumped-isotope" geochemistry—The study of naturally-occurring, multiply-substituted isotopologues: Earth and Planetary Science Letters, v. 262, p. 309–327, https://doi.org/10.1016/j.epsl.2007.08.020.

EMERGEO Working Group, 2010, Evidence for surface rupture associated with the Mw 6.3 L'Aquila earthquake sequence of April 2009 (central Italy): Terra Nova, v. 22, p. 43–51, https://doi.org/10.1111/j.1365-3121.2009.00915.x.

Faccenna, C., Davy, P., Brun, J.-P., Funiciello, R., Giardini, D., Mattei, M., and Nalpas, T., 1996, The dynamics of back-arc extension: An experimental approach to the opening of the Tyrrhenian Sea: Geophysical Journal International, v. 126, p. 781–795, https://doi.org/10.1111/j.1365-246X.1996.tb04702.x.

Faccenna, C., Becker, T.W., Lucente, F.P., Jolivet, L., and Rossetti, F., 2001, History of subduction and backarc extension in the central Mediterranean: Geophysical Journal International, v. 145, p. 809–820, https://doi.org/10.1046/j.0956-540x.2001.01435.x.

Falcucci, E., Gori, S., Peronace, E., Fubelli, G., Moro, M., Saroli, M., Giaccio, B., Messina, P., Naso, G., Scardia, G., Sposato, A., Voltaggio, M., Galli, P., and Galadini, F., 2009, The Paganica fault and surface coseismic ruptures caused by the 6 April 2009 earthquake (L'Aquila, central Italy): Seismological Research Letters, v. 80, p. 940–950, https://doi.org/10.1785/gssrl.80.6.940.

Falcucci, E., Gori, S., Moro, M., Pisani, A.R., Melini, D., Galadini, F., and Fredi, P., 2011, The 2009 L'Aquila earthquake (Italy): What's next in the region?: Hints from stress diffusion analysis and normal fault activity: Earth and Planetary Science Letters, v. 305, p. 350–358, https://doi.org/10.1016/j.epsl.2011.03.016.

Falcucci, E., Gori, S., Moro, M., Fubelli, G., Saroli, M., Chiarabba, C., and Galadini, F., 2015, Deep reaching versus vertically restricted Quaternary normal faults: Implications on seismic potential assessment in tectonically active regions: Lessons from the Middle Aterno Valley fault system, central Italy: Tectonophysics, v. 651–652, p. 186–198, https://doi.org/10.1016/j.tecto.2015.03.021.

Falcucci, E., Gori, S., Galadini, F., Fubelli, G., Moro, M., and Saroli, M., 2016, Active faults in the epicentral and mesoseismal Ml 6.0 24, 2016 Amatrice earthquake region, central Italy: Methodological and seismotectonic issues: Annals of Geophysics, v. 59, https://doi.org/10.4401/ag-7266.

Fellin, M.G., San Jose, M., Faccenna, C., Willett, S.D., Cosentino, D., Lanari, R., Gourbet, L., and Maden, C., 2022, Transition from slab roll-back to slab break-off in the central Apennines, Italy: Constraints from the stratigraphic and thermochronologic record: Geological Society of America Bulletin, v. 134, p. 1916–1930, https://doi.org/10.1130/B36123.1.

Fischer, A.G., 1986, Climatic rhythms recorded in strata: Annual Review of Earth and Planetary Sciences, v. 14, p. 351–376, https://doi.org/10.1146/annurev.ea.14.050186.002031.

Florio, G., Milano, M., and Cella, F., 2021, Gravity mapping of basement depth in seismogenic, fault-controlled basins: The case of Middle Aterno Valley (Central Italy): Tectonophysics, v. 817, https://doi.org/10.1016/j.tecto.2021.229044.

Frakes, L.A., and Francis, J.E., 1988, A guide to Phanerozoic cold polar climates from high-latitude ice rafting in the Cretaceous: Nature, v. 333, p. 547–549, https://doi.org/10.1038/333547a0.

Francke, A., Lacey, J.H., Marchegiano, M., Wagner, B., Ariztegui, D., Zanchetta, G., Kusch, S., Ufer, K., Baneschi, I., and Knödgen, K., 2022, Coeval Mediterranean rainfall and global marine circulation patterns during the Last Glacial: Boreas, v. 51, p. 219–237, https://doi.org/10.1111/bor.12552.

Fu, Y., von Dobeneck, T., Franke, C., Heslop, D., and Kasten, S., 2008, Rock magnetic identification and geochemical process models of greigite formation in Quaternary marine sediments from the Gulf of Mexico (IODP Hole U1319A): Earth and Planetary Science Letters, v. 275, p. 233–245, https://doi.org/10.1016/j.epsl.2008.07.034.

Funiciello, F., Faccenna, C., and Giardini, D., 1999, Laboratory experiments of subduction: Geophysical Research Abstracts, v. 1, p. 62.

Galli, P., Giaccio, B., and Messina, P., 2010, The 2009 central Italy earthquake seen through 0.5 Myr-long tectonic history of the L'Aquila faults system: Quaternary Science Reviews, v. 29, p. 3768–3789, https://doi.org/10.1016/j.quascirev.2010.08.018.

Galli, P., Giaccio, B., Messina, P., Peronace, E., and Zuppi, G.M., 2011, Palaeoseismology of the L'Aquila faults (central Italy, 2009, M_w 6.3 earthquake): Implications for active fault linkage: Geophysical Journal International, v. 187, p. 1119–1134, https://doi.org/10.1111/j.1365-246X.2011.05233.x.

Galli, P., Galderisi, A., Peronace, E., Giaccio, B., Hajdas, I., Messina, P., Pileggi, D., and Polpetta, F., 2019, The awakening of the dormant Mount Vettore fault (2016 central Italy earthquake, M_w 6.6): Paleoseismic clues on its millennial silences: Tectonics, v. 38, p. 687–705, https://doi.org/10.1029/2018TC005326.

Geurts, A.H., Whittaker, A.C., Gawthorpe, R.L., and Cowie, P.A., 2020, Transient landscape and stratigraphic responses to drainage integration in the actively extending central Italian Apennines: Geomorphology, v. 353, https://doi.org/10.1016/j.geomorph.2019.107013.

Giaccio, B., Galli, P., Messina, P., Peronace, E., Scardia, G., Sottili, G., and Silvestri, S., 2012, Fault and basin depocentre migration over the last 2 Ma in the L'Aquila 2009 earthquake region, central Italian Apennines: Quaternary Science Reviews, v. 56, p. 69–88, https://doi.org/10.1016/j.quascirev.2012.08.016.

Gibbard, P.L., and Head, M.J., 2009, IUGS ratification of the Quaternary System/Period and the Pleistocene Series/Epoch with a base at 2.58 Ma: Quaternaire, v. 20, p. 411–412, https://doi.org/10.4000/quaternaire.5289.

Grauel, A.-L., Hodell, D.A., and Bernasconi, S.M., 2016, Quantitative estimates of tropical temperature change in lowland Central America during the last 42 ka: Earth and Planetary Science Letters, v. 438, p. 37–46, https://doi.org/10.1016/j.epsl.2016.01.001.

Hilgen, F.J., 1987, Sedimentary cycles and high-resolution chronostratigraphic correlations in the mediterranean Pliocene: Stratigraphic Newsletter, v. 17, p. 109–127, https://doi.org/10.1127/nos/17/1987/109.

Hilgen, F.J., 1991, Astronomical calibration of Gauss to Matuyama sapropels in the Mediterranean and implication for the Geomagnetic Polarity Time Scale: Earth and Planetary Science Letters, v. 104, p. 226–244, https://doi.org/10.1016/0012-821X(91)90206-W.

Horng, C.S., Lee, M.Y., Pälike, H., Wei, K.-Y., Liang, W.T., Iizuka, Y., and Torii, M., 2002, Astronomically calibrated ages for geomagnetic reversals within the Matuyama Chron: Earth, Planets, and Space, v. 54, p. 679–690, https://doi.org/10.1186/BF03351719.

Horng, C.S., Roberts, A.P., and Liang, W.T., 2003, Astronomically tuned record of relative geomagnetic pa-

leointensity from the western Philippine Sea: Journal of Geophysical Research: Solid Earth, v. 108, v. B1, https://doi.org/10.1029/2001JB001698.

Hudson, A.M., et al., 2017, Stable C, O and clumped isotope systematics and ^{14}C geochronology of carbonates from the Quaternary Chewaucan closed-basin lake system, Great Basin, USA: Implications for paleoenvironmental reconstructions using carbonates: Geochimica et Cosmochimica Acta, v. 212, p. 274–302, https://doi.org/10.1016/j.gca.2017.06.024.

Huntington, K.W., Wernicke, B.P., and Eiler, J.M., 2010, Influence of climate change and uplift on Colorado plateau paleotemperatures from carbonate clumped isotope thermometry: Tectonics, v. 29, https://doi.org/10.1029/2009TC002449.

Iezzi, F., Francescone, M., Pizzi, A., Blumetti, A., Boncio, P., Di Manna, P., Pace, B., Piacentini, T., Papasodaro, F., Morelli, F., Caciagli, M., Chiappini, M., D'Ajello Caracciolo, F., Materni, V., Nicolosi, I., Sapia, V., and Urbini, S., 2023, Slip localization on multiple fault splays accommodating distributed deformation across normal fault complexities: Tectonophysics, v. 868, https://doi.org/10.1016/j.tecto.2023.230075.

Improta, L., et al., 2019, Multi-segment rupture of the 2016 Amatrice-Visso-Norcia seismic sequence (central Italy) constrained by the first high-quality catalog of early aftershocks: Scientific Reports, v. 9, 6921, https://doi.org/10.1038/s41598-019-43393-2.

John, C.M., and Bowen, D., 2016, Community software for challenging isotope analysis: First applications of "Easotope" to clumped isotope: Rapid Communications in Mass Spectrometry, v. 30, p. 2285–2300, https://doi.org/10.1002/rcm.7720.

Kao, S.-J., Horng, C.-S., Roberts, A.P., and Liu, K.-K., 2004, Carbon-sulfur-iron relationships in sedimentary rocks from southwestern Taiwan: Influence of geochemical environment on greigite and pyrrhotite formation: Chemical Geology, v. 203, p. 153–168, https://doi.org/10.1016/j.chemgeo.2003.09.007.

Kocken, I.J., Müller, I.A., and Ziegler, M., 2019, Optimizing the use of carbonate standards to minimize uncertainties in clumped isotope data: Geochemistry, Geophysics, Geosystems, v. 20, p. 5565–5577, https://doi.org/10.1029/2019GC008545.

Kodama, K.P., and Hinnov, L., 2015, Rock Magnetic Cyclostratigraphy: Wiley-Blackwell, 176 p, https://doi.org/10.1002/9781118561294.

Laskar, J., Fienga, A., Gastineau, M., and Manche, H., 2011, La2010: A new orbital solution for the long-term motion of the Earth: Astronomy & Astrophysics, v. 532, https://doi.org/10.1051/0004-6361/201116836.

Lavecchia, G., et al., 2016, Ground deformation and source geometry of the 24 August 2016 Amatrice earthquake (Central Italy) investigated through analytical and numerical modeling of DInSAR measurements and structural-geological data: Geophysical Research Letters, v. 43, p. 12,389–12,398, https://doi.org/10.1002/2016GL071723.

Le Bas, M.J., Le Maitre, R.W., Streckeisen, A., and Zanettin, B., 1986, A chemical classification of volcanic rocks based on the total alkali-silica diagram: Journal of Petrology, v. 27, p. 745–750, https://doi.org/10.1093/petrology/27.3.745.

Lee, J.-Y., Marti, K., Severinghaus, J.P., Kawamura, K., Yoo, H.-S., Lee, J.B., and Kim, J.S., 2006, A redetermination of the isotopic abundances of atmospheric Ar: Geochimica et Cosmochimica Acta, v. 70, p. 4507–4512, https://doi.org/10.1016/j.gca.2006.06.1563.

Li, M., Hinnov, L.A., and Kump, L.R., 2019, Acycle: Time-series analysis software for paleoclimate projects and education: Computers & Geosciences, v. 127, p. 12–22, https://doi.org/10.1016/j.cageo.2019.02.011.

Lisiecki, L.E., and Raymo, M.E., 2005, A Pliocene-Pleistocene stack of 57 globally distributed benthic δ^{18}O records: Paleoceanography, v. 20, https://doi.org/10.1029/2004PA001071.

Liu, M., and Stein, S., 2016, Mid-continental earthquakes: Spatiotemporal occurrences, causes, and hazards: Earth-Science Reviews, v. 162, p. 364–386, https://doi.org/10.1016/j.earscirev.2016.09.016.

Macrì, P., et al., 2016, Analysis of a 150 m sediment core from the coseismic subsidence depocenter of the 2009 Mw = 6.1 L'Aquila earthquake (Italy): Implications for Holocene-Pleistocene tectonic subsidence rates and for the age of the seismogenic Paganica fault system: Tectonophysics, v. 687, p. 180–194, https://doi.org/10.1016/j.tecto.2016.09.004.

Magri, D., di Rita, F., and Palombo, M.R., 2010, An Early Pleistocene interglacial record from an intermontane basin of central Italy (Scoppito, L'Aquila): Quaternary International, v. 225, p. 106–113, https://doi.org/10.1016/j.quaint.2009.04.005.

Magri, D., di Rita, F., Aranbarri, J., Fletcher, W., and González-Sampériz, P., 2017, Quaternary disappearance of tree taxa from Southern Europe: Timing and trends: Quaternary Science Reviews, v. 163, p. 23–55, https://doi.org/10.1016/j.quascirev.2017.02.014.

Mancini, M., Cavuoto, G., Pandolfi, L., Petronio, C., Salari, L., and Sardella, R., 2012, Coupling basin infill history and mammal biochronology in a Pleistocene intramontane basin: The case of western L'Aquila Basin (Central Apennines, Italy): Quaternary International, v. 267, p. 62–77, https://doi.org/10.1016/j.quaint.2011.03.020.

Manighetti, I., Mercier, A., and De Barros, L., 2021, Fault trace corrugation and segmentation as a measure of fault structural maturity: Geophysical Research Letters, v. 48, https://doi.org/10.1029/2021GL095372.

Maraio, S., Villani, F., Bruno, P.P.G., Sapia, V., and Improta, L., 2023, Active fault detection and characterization by ultrashallow seismic imaging: A case study from the 2016 Mw 6.5 central Italy earthquake: Tectonophysics, v. 850, https://doi.org/10.1016/j.tecto.2023.229733.

Marchegiano, M., and John, C.M., 2022, Disentangling the impact of global and regional climate changes during the middle Eocene in the Hampshire Basin: New insights from carbonate clumped isotopes and ostracod assemblages: Paleoceanography and Paleoclimatology, v. 37, https://doi.org/10.1029/2021PA004299.

Marchegiano, M., Horne, D.J., Gliozzi, E., Francke, A., Wagner, B., and Ariztegui, D., 2020, Rapid Late Pleistocene climate change reconstructed from a lacustrine ostracod record in central Italy (Lake Trasimeno, Umbria): Boreas, v. 49, p. 685–920, https://doi.org/10.1111/bor.12450.

Marchegiano, M., Peral, M., Doyle, R., García-Alix, A., Francke, A., Snoeck, C., Goderis, S., and Claeys, P., 2024a, Temperature and hydrological variations during the Late-Glacial in the central Mediterranean: Application of the novel ostracod-clumped isotope thermometer: Earth and Planetary Science Letters, v. 625, https://doi.org/10.1016/j.epsl.2023.118470.

Marchegiano, M., Peral, M., Venderickx, J., Martens, K., García-Alix, A., Snoeck, C., Goderis, S., and Claeys, P., 2024b, The ostracod clumped-isotope thermometer: A novel tool to accurately quantify continental climate changes: Geophysical Research Letters, v. 51, https://doi.org/10.1029/2023GL107426.

Martinetto, E., Bertini, A., Basilici, G., Baldanza, A., Bizzarri, R., Cherin, M., Gentili, S., and Pontini, M.R., 2014, The plant record of the Dunarobba and Pietrafitta sites in the Plio-Pleistocene palaeoenvironmental context of central Italy: Alpine and Mediterranean Quaternary, v. 27, no. 1, p. 29–72, https://amq.aiqua.it/index.php/amq/article/view/70.

Meckler, A.N., Ziegler, M., Millán, M.I., Breitenbach, S.F.M., and Bernasconi, S.M., 2014, Long-term performance of the Kiel carbonate device with a new correction scheme for clumped isotope measurements: Rapid Communications in Mass Spectrometry, v. 28, p. 1705–1715, https://doi.org/10.1002/rcm.6949.

Meckler, A.N., et al., 2022, Cenozoic evolution of deep ocean temperature from clumped isotope thermometry: Science, v. 377, p. 86–90, https://doi.org/10.1126/science.abk0604.

Min, K.W., Mundil, R., Renne, P.R., and Ludwig, K.R., 2000, A test for systematic errors in ^{40}Ar/^{39}Ar geochronology through comparison with U/Pb analysis of a 1.1-Ga rhyolite: Geochimica et Cosmochimica Acta, v. 64, p. 73–98, https://doi.org/10.1016/S0016-7037(99)00204-5.

Nehme, C., Todisco, D., Breitenbach, S.F.M., Couchoud, I., Marchegiano, M., Peral, M., Vonhof, H., Hellstrom, J., Tjallingii, R., and Claeys, P., 2023, Holocene hydroclimate variability along the Southern Patagonian margin (Chile) reconstructed from Cueva Chica speleothems: Global and Planetary Change, v. 222, https://doi.org/10.1016/j.gloplacha.2023.104050.

Nicol, A., Walsh, J., Berryman, K., and Nodder, S., 2005, Growth of a normal fault by the accumulation of slip over millions of years: Journal of Structural Geology, v. 27, p. 327–342, https://doi.org/10.1016/j.jsg.2004.09.002.

Niespolo, E.M., Rutte, D., Deino, A.L., and Renne, P.R., 2017, Intercalibration and age of the Alder Creek sanidine ^{40}Ar/^{39}Ar standard: Quaternary Geochronology, v. 39, p. 205–213, https://doi.org/10.1016/j.quageo.2016.09.004.

Nocentini, M., Asti, R., Cosentino, D., Durante, F., Gliozzi, E., Macerola, L., and Tallini, M., 2017, Plio-Quaternary geology of L'Aquila-Scoppito Basin (central Italy): Journal of Maps, v. 13, p. 563–574, https://doi.org/10.1080/17445647.2017.1340910.

Nocentini, M., Cosentino, D., Spadi, M., and Tallini, M., 2018, Plio-Quaternary geology of the Paganica-San Demetrio-Castelnuovo Basin (Central Italy): Journal of Maps, v. 14, p. 411–420, https://doi.org/10.1080/17445647.2018.1481774.

Palombo, M.R., Mussi, M., Agostini, S., Barbieri, M., di Canzio, E., di Rita, F., Fiore, I., Iacumin, P., Magri, D., Speranza, F., and Tagliacozzo, A., 2010, Human peopling of Italian intramontane basins: The early Middle Pleistocene site of Pagliare di Sassa (L'Aquila, central Italy): Quaternary International, v. 223–224, p. 170–178, https://doi.org/10.1016/j.quaint.2009.10.038.

Peral, M., et al., 2020, Changes in temperature and oxygen isotopic composition of Mediterranean water during the Mid-Pleistocene transition in the Montalbano Jonico section (southern Italy) using the clumped-isotope thermometer: Palaeogeography, Palaeoclimatology, Palaeoecology, v. 544, https://doi.org/10.1016/j.palaeo.2020.109603.

Peral, M., Marchegiano, M., Verheyden, S., Goderis, S., Van Helden, T., Vanhaecke, F., Van Acker, T., Dehais, T., Xue, J., Cheng, H., Snoeck, C., and Claeys, P., 2024, A climatic degradation coeval with Neanderthal last occupations in Europe over the MIS3: Quaternary Science Reviews, v. 329, https://doi.org/10.1016/j.quascirev.2024.108564.

Petersen, S.V., et al., 2019, Effects of improved ^{17}O correction on interlaboratory agreement in clumped isotope calibrations, estimates of mineral-specific offsets, and temperature dependence of acid digestion fractionation: Geochemistry, Geophysics, Geosystems, v. 20, p. 3495–3519, https://doi.org/10.1029/2018GC008127.

Picard, A., Gartman, A., Clarke, D.R., and Girguis, P.R., 2018, Sulfate-reducing bacteria influence the nucleation and growth of mackinawite and greigite: Geochimica et Cosmochimica Acta, v. 220, p. 367–384, https://doi.org/10.1016/j.gca.2017.10.006.

Pontini, M., Albianelli, A., Basilici, G., Bertini, A., and Napoleone, G., 2002, Pollen record and magnetostratigraphy of the Middle-Late Pliocene lacustrine sequence in the Tiberino basin, (central Italy): Bollettino della Società Geologica Italiana, volume speciale no. 1, p. 467–472.

Pucci, S., Villani, F., Civico, R., Pantosti, D., Del Carlo, P., Smedile, A., and Gueli, A., 2015, Quaternary geology of the Middle Aterno Valley, 2009 L'Aquila earthquake area (Abruzzi Apennines, Italy): Journal of Maps, v. 11, p. 689–697, https://doi.org/10.1080/17445647.2014.927128.

Pucci, S., Villani, F., Civico, R., Di Naccio, D., Porreca, M., Benedetti, L., Gueli, A., Stella, G., Baccheschi, P., and Pantosti, D., 2019, Complexity of the 2009 L'Aquila earthquake causative fault system (Abruzzi Apennines, Italy) and effects on the Middle Aterno Quaternary basin arrangement: Quaternary Science Reviews, v. 213, p. 30–66, https://doi.org/10.1016/j.quascirev.2019.04.014.

Puliti, I., Pizzi, A., Benedetti, L., Di Domenica, A., and Fleury, J., 2020, Comparing slip distribution of an active fault system at various timescales: Insights for the evolution of the Mt. Vettore-Mt. Bove fault system in Central Apennines: Tectonics, v. 39, https://doi.org/10.1029/2020TC006200.

Racano, S., van der Beek, P.A., Schildgen, T.F., Faccenna, C., Buleo Tebar, V., and Cosentino, D., 2024, Slab driven Quaternary rock-uplift and topographic evolution in the

northern-central Apennines from linear inversion of the drainage system: Geochemistry, Geophysics, Geosystems, v. 25, https://doi.org/10.1029/2024GC011592.

Raymo, M.E., Ruddiman, W.F., Backman, J., Clement, B.M., and Martinson, D.G., 1989, Late Pliocene variation in Northern Hemisphere ice sheets and North Atlantic deep water circulation: Paleoceanography, v. 4, p. 413–446, https://doi.org/10.1029/PA004i004p00413.

Regattieri, E., Giaccio, B., Mannella, G., Zanchetta, G., Nomade, S., Tognarelli, A., Perchiazzi, N., Vogel, H., Boschi, C., Drysdale, R.N., Wagner, B., Gemelli, M., and Tzedakis, P., 2019, Frequency and dynamics of millennial-scale variability during Marine Isotope Stage 19: Insights from the Sulmona Basin (central Italy): Quaternary Science Reviews, v. 214, p. 28–43, https://doi.org/10.1016/j.quascirev.2019.04.024.

Roberts, A.P., and Weaver, R., 2005, Multiple mechanisms of remagnetization involving sedimentary greigite (Fe_3S_4): Earth and Planetary Science Letters, v. 231, p. 263–277, https://doi.org/10.1016/j.epsl.2004.11.024.

Sadori, L., Giardini, M., Chiarini, E., Mattei, M., Papasodaro, F., and Porreca, M., 2010, Pollen and macrofossil analyses of Pliocene lacustrine sediments (Salto river valley, Central Italy): Quaternary International, v. 225, p. 44–57, https://doi.org/10.1016/j.quaint.2009.05.008.

Sagnotti, L., 2007, Iron sulfides, *in* Gubbins, D., and Herrero-Bervera, E., eds., Encyclopaedia of Geomagnetism and Paleomagnetism: Dordrecht, Springer, p. 454–459, https://doi.org/10.1007/978-1-4020-4423-6_160.

Sagnotti, L., 2013, Demagnetization Analysis in Excel (DAIE)—An open source workbook in Excel for viewing and analyzing demagnetization data from paleomagnetic discrete samples and u-channels: Annals of Geophysics, v. 56, https://doi.org/10.4401/ag-6282.

Sagnotti, L., and Winkler, A., 1999, Rock magnetism and palaeomagnetism of greigite-bearing mudstones in the Italian peninsula: Earth and Planetary Science Letters, v. 165, p. 67–80, https://doi.org/10.1016/S0012-821X(98)00248-9.

Sagnotti, L., Cascella, A., Ciaranfi, N., Macrì, P., Maiorano, P., Marino, M., and Taddeucci, J., 2010, Rock magnetism and paleomagnetism of the Montalbano Jonico section (Italy): Evidence for late diagenetic growth of greigite and implications for magnetostratigraphy: Geophysical Journal International, v. 180, p. 1049–1066, https://doi.org/10.1111/j.1365-246X.2009.04480.x.

Santo, A., Ascione, A., Di Crescenzo, G., Miccadei, E., Piacentini, T., and Valente, E., 2014, Tectonic-geomorphological map of the middle Aterno River valley (Abruzzo, central Italy): Journal of Maps, v. 10, p. 365–378, https://doi.org/10.1080/17445647.2013.867545.

Schwarzacher, W., 2000, Repetitions and cycles in stratigraphy: Earth-Science Reviews, v. 50, p. 51–75, https://doi.org/10.1016/S0012-8252(99)00070-7.

Scognamiglio, L., Tinti, E., Michelini, A., Dreger, D.S., Cirella, A., Cocco, M., Mazza, S., and Piatanesi, A., 2010, Fast determination of moment tensors and rupture history: What has been learned from the 6 April 2009 L'Aquila earthquake sequence: Seismological Research Letters, v. 81, p. 892–906, https://doi.org/10.1785/gssrl.81.6.892.

Scognamiglio, L., Tinti, E., Casarotti, E., Pucci, S., Villani, F., Cocco, M., Magnoni, F., Michelini, A., and Dreger, D., 2018, Complex fault geometry and rupture dynamics of the M_W 6.5, 30 October 2016, Central Italy earthquake: Journal of Geophysical Research: Solid Earth, v. 123, p. 2943–2964, https://doi.org/10.1002/2018JB015603.

Shackleton, N.J., Berger, A., and Peltier, W.R., 1990, An alternative astronomical calibration of the lower Pleistocene timescale based on ODP Site 677: Transactions of the Royal Society of Edinburgh: Earth Sciences, v. 81, p. 251–261, https://doi.org/10.1017/S0263593300020782.

Soria, A.R., Muñoz, A., Liesa, C.L., Luzón, A., Meléndez, A., and Nieves Meléndez, M., 2012, Climate-driven cyclicity in an Early Cretaceous synrift lacustrine series (Aguilón sub-basin, NE Spain): Terra Nova, v. 24, p. 407–416, https://doi.org/10.1111/j.1365-3121.2012.01080.x.

Spadi, M., Gliozzi, E., Cosentino, D., and Nocentini, M., 2016, Late Piacenzian-Gelasian freshwater ostracods (Crustacea) from L'Aquila Basin (central Apennines, Italy): Journal of Systematic Palaeontology, v. 14, p. 617–642, https://doi.org/10.1080/14772019.2015.1079561.

Spadi, M., Gliozzi, E., and Medici, M.C., 2018, A Plio–Pleistocene *Caspiocypris* species flock (Candoninae, Ostracoda) from the Palaeolake Tiberino (Umbria, central Italy): Journal of Systematic Palaeontology, v. 16, p. 417–434, https://doi.org/10.1080/14772019.2017.1310143.

Spadi, M., Gliozzi, E., and Medici, M.C., 2019, Piacenzian-Gelasian non-marine ostracods from the Dunarobba Fossil Forest (Tiberino Basin, Umbria, central Italy): Papers in Palaeontology, v. 5, p. 391–413, https://doi.org/10.1002/spp2.1240.

Spadi, M., Tallini, M., Albano, M., Cosentino, D., Nocentini, M., and Saroli, M., 2022, New insights on bedrock morphology and local seismic amplification of the Castelnuovo village (L'Aquila Basin, Central Italy): Engineering Geology, v. 297, https://doi.org/10.1016/j.enggeo.2021.106506.

Storti, F., Aldega, L., Balsamo, F., Corrado, S., Del Monaco, F., Di Paolo, L., Mastalertz, M., Monaco, P., and Tallini, M., 2013, Evidence for strong middle Pleistocene earthquakes in the epicentral area of the 6 April 2009 L'Aquila seismic event from sediment paleofluidization and overconsolidation: Journal of Geophysical Research: Solid Earth, v. 118, p. 3767–3784, https://doi.org/10.1002/jgrb.50254.

Suc, J.P., and Popescu, S.M., 2005, Pollen records and climatic cycles in the North Mediterranean region since 2.7 Ma, *in* Head, M.J., and Gibbard, P.L., eds., Early-Middle Pleistocene Transitions: The Land-Ocean Evidence: Geological Society, London, Special Publication 247, p. 147–158, https://doi.org/10.1144/gsl.sp.2005.247.01.08.

Suc, J.P., Combourieu-Nebout, N., Seret, G., Popescu, S.M., Klotz, S., Gautier, F., Clauzon, G., Westgate, J., Insinga, D., and Sandhu, A.S., 2010, The Crotone series: A synthesis and new data: Quaternary International, v. 219, p. 121–133, https://doi.org/10.1016/j.quaint.2010.01.008.

Tallini, M., Cavuoto, G., Del Monaco, F., Di Fiore, V., Mancini, M., Caielli, G., Cavinato, G.P., De Franco, R., Pelosi, N., and Rapolla, A., 2012, Seismic surveys integrated with geological data for in-depth investigation of Mt. Pettino active fault area (western L'Aquila Basin): Italian Journal of Geosciences, v. 131, p. 389–402, https://doi.org/10.3301/IJG.2012.10.

Tallini, M., Spadi, M., Cosentino, D., Nocentini, M., Cavuoto, G., and Di Fiore, V., 2019, High resolution seismic reflection exploration for evaluating the seismic hazard in a Plio-Quaternary intermontane basin (L'Aquila downtown, Central Italy): Quaternary International, v. 532, p. 34–47, https://doi.org/10.1016/j.quaint.2019.09.016.

Thomson, D.J., 1982, Spectrum estimation and harmonic analysis: Proceedings of the IEEE, v. 70, p. 1055–1096, https://doi.org/10.1109/PROC.1982.12433.

Torrence, C., and Compo, G.P., 1998, A practical guide to wavelet analysis: Bulletin of the American Meteorological Society, v. 79, p. 61–78, https://doi.org/10.1175/1520-0477(1998)079<0061:APGTWA>2.0.CO;2.

Vannoli, P., Burrato, P., Fracassi, U., and Valensise, G., 2012, A fresh look at the seismotectonics of the Abruzzi (central Apennines) following the 6 April 2009 L'Aquila earthquake (Mw 6.3): Italian Journal of Geosciences, v. 131, p. 309–329, https://doi.org/10.3301/IJG.2012.03.

Vezzani, L., Ghisetti, F., and Festa, A., 2009, Caratterizzazione strutturale dei principali sistemi di faglie dell'Abruzzo Aquilano: Geoitalia, v. 28, p. 4–12.

Weedon, G.P., 2003, Time Series Analysis and Cyclostratigraphy: Examining Stratigraphic Records of Environmental Cycles: Cambridge, UK, Cambridge University Press, 259 p., https://doi.org/10.1017/CBO9780511535482.

Xuan, C., Channell, J.E.T., and Hodell, D.A., 2016, Quaternary paleomagnetic and oxygen isotope records from diatom-rich sediments of the southern Gardar Drift (IODP Site U1304, North Atlantic): Quaternary Science Reviews, v. 142, p. 74–89, https://doi.org/10.1016/j.quascirev.2016.04.010.

Yue, J., Xiao, J., Wang, X., Meckler, A.N., Modestou, S.E., and Fan, J., 2022, "Cold and wet" and "warm and dry" climate transitions at the East Asian summer monsoon boundary during the last deglaciation: Quaternary Science Reviews, v. 295, https://doi.org/10.1016/j.quascirev.2022.107767.

Zhang, J., Arriga, G., Rossetti, F., Argante, V., Krämer, D., Sontag-González, M., Cosentino, D., Cipollari, P., and Tsukamoto, S., 2025, Dolomite luminescence thermochronometry reconstructs the low-temperature exhumation history of carbonate rocks in the central Apennines, Italy: Communications Earth & Environment, v. 6, 252, https://doi.org/10.1038/s43247-025-02216-1.

Zhou, X., Yang, J., Xiao, G., Wang, J., Hu, Y., Zheng, Y., Liu, J., and Li, X., 2023, Megacycles of climate and vegetation in East Asia since 3 Ma: Catena, v. 229, https://doi.org/10.1016/j.catena.2023.107195.

Science Editor: Wenjiao Xiao
Associate Editor: Stefano Mazzoli

Manuscript Received 5 May 2024
Revised Manuscript Received 10 July 2025
Manuscript Accepted 14 August 2025